Human microglia clear intraneuronal α-synuclein aggregates by GPNMB-mediated trogocytosis

Hung-Ju Chueh[1,2], Antigoni Katsikoudi[1,2], Ana Aragón-González[1,2], Chor Lai Lam[1,2], Liezel Tamon[3], Ashwin Jainarayanan[4,6], Devika Agarwal[3], Sally A. Cowley[5], David Sims[3], George K Tofaris[1,2,*]

1. Nuffield Department of Clinical Neurosciences, University of Oxford, Oxford, UK
2. Kavli Institute for Nanoscience Discovery, University of Oxford, Oxford, UK
3. MRC Weatherall Institute of Molecular Medicine, University of Oxford, Oxford, UK
4. Kennedy Institute of Rheumatology, University of Oxford, Oxford, UK
5. James and Lillian Martin Centre for Stem Cell Research, Sir William Dunn School of Pathology, University of Oxford, Oxford, UK
6. Current affiliation: Department of Neurology and Neurological Sciences, Stanford Medicine, Stanford University, Palo Alto, California

*Corresponding author
Email: george.tofaris@ndcn.ox.ac.uk

OVERLINE: Neurodegeneration

One-sentence Summary: Microglia clear intraneuronal α-synuclein aggregates

ABSTRACT

Microglia are the primary immune cells of the brain, but their role in Parkinson's disease is not fully understood. Chronic microglial activation is toxic to neurons, but in the early stages of pathology they also exert beneficial functions. We used induced pluripotent stem cell (iPSC)–derived co-culture models to investigate how human microglia respond to α-synuclein aggregates that form de novo inside human dopaminergic neurons with α-synuclein gene triplication or are triggered by fibrils. We found that microglia cleared Ser129-phosphorylated α-synuclein aggregates through a contact-dependent mechanism. This process was fine-tuned by sensing (P2RY12) and inhibitory (CD22) signals and involved selective phagocytosis of neuronal sub-compartments (trogocytosis), independently of TREM2 or phosphatidylserine. In the presence of intraneuronal α-synuclein aggregates, microglia exhibited morphological and transcriptional changes indicative of activation. Using single cell sequencing, we identified a cluster of disease-associated microglia (DAM) responsible for this beneficial phenotype and the Parkinson's disease GWAS candidate Glycoprotein non-metastatic melanoma protein B (GPNMB*)* as a key effector of aggregate clearance by microglial lysosomes. GPNMB interacted with Ser129-phosphorylated α-synuclein in iPSC-derived microglia exposed to aggregate-laden dopaminergic neurons and was upregulated in substantia nigra microglia of individuals with incidental Lewy bodies or Parkinson's disease. Microglia-specific GPNMB knockdown using CRISPRi reduced intraneuronal aggregate clearance. GPNMB-mediated trogocytosis was negatively regulated by an autocrine IL-10 signalling loop, whereas IL-10 receptor blockade enhanced the phagocytic response. Together, our study identifies a subtype of human microglia capable of removing intraneuronal aggregates and potential therapeutic targets.

INTRODUCTION

Parkinson's disease (PD) is a neurodegenerative disorder currently without a cure, affecting more than 1% of the global population over the age of 60. Pathologically, it is characterised by the degeneration of primarily dopaminergic but also other types of neurons and formation of intraneuronal filamentous inclusions composed of α-synuclein. The identification of families with α-synuclein gene (*SNCA*) multiplications indicates that an increase in wild-type α-synuclein levels through a gene dosage effect is sufficient to cause PD, suggesting a causal relationship between α-synuclein accumulation, aggregation and proteotoxicity (*1*). Therefore, understanding the mechanisms that regulate the clearance of α-synuclein aggregates is key to the development of therapies that prevent the spread of pathology and progression of the clinical symptoms. So far, most studies have focused on intracellular clearance pathways (*2*), which are already compromised by protein aggregates (*3*), whereas the contribution of non-cell-autonomous mechanisms is not fully understood or largely ascribed to the clearance of aggregates after their release from neurons (*4, 5*).

Microglia are the specialised brain resident scavenging cells that survey its microenvironment, provide neurotrophic support, prune synapses, and remove cellular debris and pathogenic entities. Although activated microglia bind to and internalise pathogenic proteins such as α-synuclein via pattern recognition receptors facilitating their clearance (*6, 7*), persistent activation by these stimuli exacerbates neuroinflammation and neurodegeneration *(8, 9)*. Age-dependent changes in microglia also influence their phagocytic efficiency such as the up-regulation of the sialic acid–binding receptor CD22, which when blocked restores microglial homeostasis and improves cognitive function in aged mice (*10*). Such studies underscore the therapeutic potential of targeting selective microglial receptors. Transcriptomic profiling of microglia has identified a subpopulation

known as disease-associated microglia (DAM), that are characterised by the upregulation of genes implicated in lysosomal, phagocytic, and lipid metabolism pathways *(11, 12).* Depending on the stimulus, microglia transition into diverse DAM states with sub-specialised functions *(13, 14)* some of which are beneficial, at least in the early phase of the neurodegenerative process (*15*). Deciphering these activation states is confounded by the realisation that microglial responses in humans differ from rodents (*16*) and exhibit a greater transcriptomic heterogeneity (*17*).

This complexity of microglia states calls for models that involve human cells in an environment that resembles the relevant disease pathology. Here, we have modelled the interaction of microglia with dopaminergic neurons using human induced pluripotent stem cell (iPSC)-derived co-cultures under pathological conditions of intraneuronal α-synuclein aggregation to determine whether microglia can clear aggregates and to identify the cellular and molecular pathways that govern this response.

RESULTS

Human iPSC-based modelling of long-term interactions between microglia and dopaminergic neurons reveals a protective response.

Most studies to date have focused on short-term interactions between microglia and neurons, typically over 48-72 hrs often with LPS-primed microglia (*18*), or on the acute microglial response to fibrils (*19*). To investigate the effects of healthy human microglia in a chronic model of intraneuronal α-synuclein pathology, we initially co-cultured iPSC-derived microglia (MG) from two control lines with dopaminergic neurons (DANs) from a patient with *SNCA* triplication ($SNCA^{TRIP}$, DAN^{TRIP}; **table S1**). DAN^{TRIP} were differentiated as we described previously (*20*) and their identity was confirmed by immunostaining (83% $TUJ1^+$ $MAP2^+$, 72% TH^+) as shown in **fig. S1A**. MG were generated by a MYB-independent

iPSC differentiation protocol (*21*). Immunofluorescence showed that 94% of cells express IBA1 and 97% express TMEM119 (**fig. S1B**).

Harvested microglia precursors (MGpre) were added to DANs at 1:1 ratio and co-cultured for two weeks from D59 until D73, a period during which further maturation of both cell types was achieved (**Fig. 1A** and **fig. S1C**). Quantification by immunofluorescence confocal microscopy at D73 revealed that the co-culture consisted of 11.7% $IBA1^+$ MG and 78.8% of $MAP2^+$ neurons, of which 71.1% were TH^+ (**Fig. 1B**). The composition of the co-culture was further assessed transcriptomically using multiple cell markers (**Fig. 1C**). This was achieved by cell type deconvolution analysis of bulk RNASeq with a reference multi-subject human single cell atlas (*22*) using the MuSiC method (*23*), which estimated the cell type composition of the bulk RNASeq samples across multiple bootstraps identifying ~80% as DANs and ~15% MG. Expression levels of relevant genes (*MERTK*, *GPR34*, *PROS1*, *C1QA*, *GAS6, TMEM119*, *TREM2*, and *P2RY12*), which were previously reported in MG (*21, 24*), were confirmed by qPCR in the microglial monocultures and MG^{HC}-DAN^{TRIP} co-cultures, and were not detectable in DAN monocultures (**fig. S1D**). *P2RY12* was significantly up regulated further in MG^{HC}-DAN^{TRIP} compared to MG alone ($P = 0.0108$) (**fig. S1D**). Thus, allogenic MG can be co-cultured with human DANs derived from patients with PD at a ratio that is roughly proportional to their brain composition (*25*) and could be used to study the MG response to PD pathology. We then analysed transcriptomic markers of metabolic, oxidative, and mitochondrial stress in co-cultures versus monocultures. We found that MG^{HC}-DAN^{TRIP} co-cultures exhibited lower expression of stress-related genes compared to DAN^{TRIP} monocultures, suggesting that addition of MG is beneficial (**Fig. 1D, fig. S2A, table S2**). Quantification of fragmented nuclei in $MAP2^+$ cells showed that neuronal death was not significantly increased in the presence of MG (**Fig. 1E**).

We therefore asked whether this improvement could be due to removal of aggregates from neurons. To this end, we used instant structured illumination microscopy (iSIM), which offers higher resolution for smaller aggregates in co-cultures of MG with either DAN^{TRIP} or their isogenic control DANs (DAN^{ISO}). We identified puncta of serine 129 phosphorylated α-synuclein (pSyn), a widely used marker of endogenous α-synuclein aggregation (*20, 26*), in MG^{HC} only when co-cultured with DAN^{TRIP}, not DAN^{ISO} ($P < 0.0001$) (**Fig. 1F**). This observation was associated with restoration of total intracellular α-synuclein levels in the MG-DAN^{TRIP} co-culture to isogenic control levels, as assessed by ELISA (**Fig. 1G**). Neurofilament light chain (NfL) levels in these cell lysates, measured by MSD electrochemiluminescence, were significantly increased when either DAN^{TRIP} or DAN^{ISO} were co-cultured with MG, with highest NfL levels detected in MG-DAN^{ISO} ($P = 0.0004$) followed by MG-$SNCA^{TRIP}$ ($P = 0.0146$) co-cultures (**Fig. 1H**). $Synapsin^+$ pre-synaptic terminals were significantly reduced in DAN^{TRIP} ($P = 0.0307$) but not DAN^{ISO} when co-cultured with MG (**Fig. 1I** and **fig. S2B)**, accompanied by the detection of $synapsin^+$ and $MAP2^+$ puncta inside $IBA1^+$ cells using 3D reconstruction (**Fig 1J**). Thus, MG sense and remove small aggregates that develop de novo inside neurons both at the axonal terminal ($synapsin^+$) and somatodendritic ($MAP2^+$) compartments, without causing neuronal injury.

Microglia promote the clearance of large intraneuronal α-synuclein aggregates

We then assessed whether human MG clear larger, established intraneuronal aggregates. To this end, we co-cultured MG derived from two unrelated healthy iPSC lines with DAN^{TRIP} seeded with fibrils (**Fig. 2A**). Fibrils generated from recombinant α-synuclein (**fig. S3A to S3E**) were first added at D45, a timepoint at which we previously found iPSC-derived DANs to be electrophysiologically active (*27*). Two weeks after fibril addition (D59), intraneuronal α-synuclein aggregation was confirmed by immunostaining (**fig. S3F**) and time-resolved FRET (**fig. S3G**) for total pSyn in cell lysates. MG were then added to

158 the neurons with established α-synuclein aggregates at D59 and co-cultured for two further weeks up to D73 (**Fig. 2A**).

160 Using immunofluorescence confocal microscopy, we found a significant reduction in intraneuronal $pSyn^+$ aggregates in the presence of MG (**Fig. 2B**), as quantified by 3 162 different parameters: percentage area containing aggregates per $MAP2^+$ neuron (**Fig. 2C**), number of aggregates per $MAP2^+$ neuron (**fig. S4A**), and average aggregate size **(fig. S4B)** 164 ($P < 0.0001$). This finding in seeded DAN^{TRIP} was further corroborated by time-resolved FRET for pSyn ($P = 0.0002$) (**Fig. 2D**) and immunoblotting of RIPA-insoluble pSyn in cell 166 lysates ($P < 0.0001$) (**Fig. 2E**). Neuronal clearance of seeded aggregates was accompanied by a more prominent increase in $pSyn^+$ puncta within MG as visualised by 3D rendering 168 (**Fig. 2F** and **2G**) and confirmed by quantification of the area of aggregates within MG ($P = 0.0019$) (**Fig. 2H**) or the number of MG containing aggregates ($P = 0.0024$) (**fig. S4C**). 170 Additionally, the presence of $MAP2^+$ puncta within MG was confirmed by quantifying the $MAP2^+$ area per microglial cell ($P = 0.0175$) (**Fig. 2I**) and the number of $MAP2^+$ puncta per 172 microglial cell ($P = 0.0005$) (**fig. S4D**). We confirmed that MG in monocultures internalise aggregates when treated with fibrils (1μM) for 24h and this process was blocked by pre-174 treatment with a non-toxic concentration (10 μM) of cytochalasin D, an inhibitor of actin polymerisation used to block phagocytosis ($P = 0.0015$) (**fig. S4E-G**). Moreover, continuous 176 treatment of the fibril-seeded co-cultures with a low (non-toxic) dose of the lysosomotropic agent chloroquine (10 μM), blocked aggregate clearance ($P = 0.0005$) (**Fig. 2J**). 178 Collectively, these data indicate that healthy human MG clear fibril-induced intraneuronal α-synuclein aggregates, by a lysosomal/phagocytic mechanism. We also assessed in our co-180 culture model of seeded aggregation, iPSC-derived MG with the PD-associated $SNCA^{TRIP}$, $LRRK2^{G2019S}$ gene mutation (*28*) or the PD risk allele GBA^{N409S} (aka GBA^{N370S}) that is 182 implicated in lysosomal function (*29*). Under our experimental conditions, these mutations

did not influence MG clearance of aggregates when compared to healthy controls as quantified by time-resolved FRET for pSyn levels (**fig. S4H**). In *SNCA*^{TRIP} MG monocultures we assessed lysosomal function relative to isogenic control MG at baseline and after addition of fibrils using Magic Red, which measures cathepsin B activity. These experiments did not reveal a lysosomal defect in *SNCA*^{TRIP} MG (**fig. S4I**). In control experiments, we tested and confirmed that endotoxin levels at the time of MG addition were low (<0.5 EU/ml) and comparable between the seeded and non-seeded conditions (**fig. S4J**). Therefore, endotoxin contamination is unlikely to be a confounding factor in our experiments**.**

We further verified that aggregate clearance is not due to MG-induced neuronal death. We found that under seeded conditions, the % neurons with healthy, non-fragmented nuclei were significantly higher in MG^{HC}-DAN^{TRIP} co-culture compared to DAN^{TRIP} monoculture (P = 0.0048) (**Fig. 2K**) and NfL levels in cell lysates were similar in fibril seeded DAN^{TRIP} monocultures and MG^{HC}-DAN^{TRIP} co-cultures (**Fig. 2L**). In contrast, MG treated with lipopolysaccharide (LPS, 100 ng/ml), a potent pro-inflammatory agent, also significantly reduced intraneuronal pSyn (P = 0.0006) (**Fig. 2M**). This was accompanied by neuronal damage, evidenced by significantly reduced NfL levels in cell lysates (P < 0.0176; **Fig. 2N**), increased neuronal death, indicated by a higher number of fragmented nuclei in MAP2^{+} cells (P = 0.0129) (**Fig. 2O**) and secretion of the cytotoxic cytokine TNFα (P < 0.0001) (*30*), which was minimally detectable at baseline (**Fig. 2P, fig. S4K**), even in MG^{TRIP} - DAN^{TRIP} co-cultures (**fig. S4L**). Thus, iPSC-based MG^{HC}-DAN^{TRIP} co-cultures model both beneficial and harmful responses depending on the extent of MG activation but at basal conditions, the clearance of pSyn is not due to the death of aggregate-laden neurons.

Microglial activation in response to intraneuronal α-synuclein aggregation is TREM2-independent and involves contact partly mediated by CD22 and P2RY12.

We assessed the extent of MG activation in response to increasing burden of neuronal α-synuclein pathology by quantifying the morphology of $IBA1^+$ microglia in co-culture with either DAN^{TRIP} or fibril-seeded DAN^{TRIP}. In the fibril-treated conditions, microglia displayed significantly higher circularity ($P < 0.0001$), lower aspect ratio ($P = 0.0065$) and elevated roundness ($P = 0.0002$), indicating a transition to a more rounded, less ramified morphology, characteristic of reactive activation with diminished process arborisation (**Fig 3A, B**). Accordingly, immunoblotting of cell lysates showed that the microglial marker IBA1 was significantly upregulated in the fibril-seeded condition ($P = 0.0230$) whilst PU.1, a transcription factor involved in microglial development remained unchanged (**Fig. 3C**). Furthermore, qPCR analysis revealed increased expression of disease associated microglial (DAM) genes that were previously reported in Alzheimer's disease (AD) and other neurodegenerative conditions (*11*). Specifically, we found that genes related to phagocytosis, lysosome function and lipid metabolism (e.g. *APOE, TLR4, LPL, CD68*) were upregulated in MG co-cultured with fibril-seeded DANs ($P < 0.05$) (**fig. S5A).**

To decipher how the two cell-types interact under pathological conditions, we first asked whether contact between MG and DANs changes in response to increased aggregation induced by fibrils. We quantified the spatial overlap between IBA1-positive microglia and $MAP2^+$ neurons by performing 3D volumetric analysis and calculated the proportion of $IBA1^+$ volume overlapping $MAP2^+$ volume. We found that microglial contact with neurons was enhanced when intraneuronal aggregate burden was significantly increased with seeding ($P = 0.0240$) (**Fig. 3D**). Using a transwell co-culture system we confirmed that eliminating the contact between MG and DANs prevented the clearance of $pSyn^+$ aggregates as quantified by immunofluorescence (**Fig. 3E** and **fig. S5B**).

Contact was accompanied by significantly increased expression of the DAM-related innate immune receptors TREM2 ($P = 0.043$), CD22 ($P = 0.0297$), as well as the homeostatic receptor P2RY12 ($P = 0.0471$) but not CX3CR1 or TMEM119 (**Fig. 3F, fig. S5A**), suggesting that microglia engage a hybrid activation state tailored to intraneuronal α-synuclein aggregates. To investigate how microglia recognise aggregate-laden neurons, we first tested TREM2 because it is required for the transition of MG to a DAM phenotype (*6*) in neurodegenerative disease models and it is a reported receptor for phosphatidylserine which is exposed on damaged neurons (*31*). qPCR revealed significant up-regulation of *TYROBP* ($P = 0.0177$) which interacts with TREM2, as well as *AKT* ($P = 0.0373$) and *PI3K* ($P = 0.0386$), which are downstream mediators in the TREM2 signalling pathway (**fig. S5C**). Whether TREM2 is a genetic modifier in PD is controversial (*32, 33*) and, its function in human models of α-synuclein pathology is unclear. To address this issue, we used iPSC-derived MG with CRISPR/Cas9 mediated knockout of TREM2 and their isogenic wildtype control (**fig. S5D**). Firstly, we added fibrils to either $TREM2^{KO}$ or isogenic wildtype MG monocultures and measured α-synuclein degradation 24 h later at baseline or in the presence of chloroquine (50 μM). We found that fibrils were degraded to a similar extent by $TREM2^{KO}$ or wildtype MG, as assessed by immunoblotting for total α-synuclein, and degradation was blocked by chloroquine (**Fig. 3G**). $TREM2^{KO}$ or wildtype MG were also co-cultured with fibril-seeded DAN^{TRIP} as described earlier and pSyn was measured by time-resolved FRET. These experiments did not reveal any difference in the clearance of pSyn aggregates between $TREM2^{KO}$ versus wildtype isogenic control MG (**Fig. 3H**). To ensure these results were not due to compensation from chronic lack of TREM2 in this model, we also assessed the effect of acute TREM2 inhibition using specific TREM2-blocking antibodies (kindly provided by Eli Lilly). We found that TREM2 blocking antibodies at 10 μg/ml did not modify the clearance of pSyn aggregates when compared to non-targeted

control IgG (**Fig. 3I**). Furthermore, recombinant Annexin V (0.2 μg/ml, added 24 h before and during the two weeks of co-culture), which binds to and blocks phosphatidylserine signalling, had no effect (**Fig. 3J**). In control experiments, we stained non-permeabilised neurons with anti-Annexin V antibody (**fig. S5E**). Quantification of % of Annexin V^+ area ($P = 0.0133$) (**fig. S5F**) or fluorescence intensity ($P = 0.0119$) (**fig. S5G**) confirmed Annexin V binding, which was increased in fibril-seeded neurons treated with Annexin V. Thus, phosphatidylserine which is exposed on the surface of neurons with aggregates, and TREM2 on MG are dispensable for microglial aggregate clearance in this human model.

We then asked whether contact may involve both homeostatic and DAM receptors acting in concert. We assessed CD22, an α2,6-linked sialic acid receptor previously shown to prevent aggregate clearance (*10*) and P2RY12, a G-protein-coupled receptor activated by neuronal damage *(34, 35)* that were up-regulated with increased aggregation. We found that continuous treatment during the 2-week co-culture period with blocking antibodies against CD22 (5 μg/ml) significantly enhanced aggregate clearance ($P = 0.0002$) (**Fig. 3K**), whereas treatment with the P2RY12 inhibitor PSB-0739 (4 μM) significantly increased residual aggregate load by 2-fold ($P = 0.0226$) (**Fig. 3L**), as assessed by time-resolved FRET for pSyn. To further investigate candidate effectors that are not readily targetable with antibodies, we integrated a doxycycline-inducible CRISPR-dCas9 interference cassette into one of the healthy control iPSC lines (**fig. S6A** to **S6G**). We knocked down *P2RY12* expression specifically in MG by lentiviral transduction at the iPSC stage with pooled gRNAs targeting the promoter region of *P2RY12* (**fig. S6H**), followed by differentiation into MG and subsequent addition to DANs. A 65% reduction in *P2RY12* mRNA as assessed using qPCR in the co-culture at D73 ($P = 0.0004$) (**fig. S6I**) significantly increased the residual neuronal $pSyn^+$ aggregates by 1.8-fold as measured by time-resolved FRET ($P = 0.0337$) (**Fig. 3M**). Collectively, these data suggest that neuron-microglial contact is

required for the removal of intraneuronal aggregates, and this process is fine-tuned by multiple signals such as P2RY12, which senses neuronal damage and CD22, which limits phagocytic activity.

Finally, we performed single-cell RNA sequencing (scRNA-seq) on DAN^{TRIP} seeded with fibrils alone and compared them to seeded DAN^{TRIP} co-cultured with MG. Unbiased clustering across the combined conditions revealed eight distinct clusters (**fig. S7A**). Clusters 0, 6, and 7 were identified as neurons in monocultures, based on their expression of dopaminergic markers (**fig. S7B**, **S7C**) and additional neuronal markers (**fig. S7D**) (n=22,045), whereas clusters 1 and 2 from MG^{HC}-DAN^{TRIP} co-cultures were identified as neurons (n=6,984). Cluster 3 was classified as a microglial population, as evident by the relevant marker expression profile (**fig. S7E**) (n=2,676). We found that neurons cocultured with microglia exhibited a distinct transcriptional response compared to DAN^{TRIP} monoculture, principally in genes implicated in extracellular matrix (ECM) remodelling (**Fig. 3N, table S3**). Gene ontology analysis revealed enrichment in pathways such as syndecan interactions, collagen organisation, and MET signalling, non-integrin-membrane ECM interactions, suggesting that neurons actively modify their ECM microenvironment when in contact with MG (**Fig. 3O**). These findings suggest that active organisation of the neuronal ECM may further refine interactions with MG. Finally, we analysed transcriptomic markers related to metabolic activity, hypoxia, and mitochondrial stress in co-cultures versus neuronal monocultures. These results corroborated our earlier bulk RNA-seq findings, i.e. that stress markers are reduced in neurons co-cultured with MG when compared to neuronal monocultures, with the most pronounced effect observed under fibril seeded conditions (**fig. S7F**).

Single-cell RNA sequencing identifies clusters of α-synuclein-related DAM.

To fully define the molecular phenotype of human MG in our model and assess its relevance to human pathology, we performed scRNA-seq on MG isolated from co-cultures with DAN^{TRIP}, with or without fibrils. In total, we profiled 5,640 MG transcriptomes across all conditions (**Fig. 4A**). Cells from all three replicates exhibited enrichment in microglial identity and maturation markers (**fig. S8A**), consistent with our bulk RNA-seq data and confirming successful differentiation.

Unbiased clustering across combined conditions revealed five distinct clusters, consistently detected across replicates. Clusters 3 and 4 were more abundant in the fibril-seeded condition (**Fig. 4B**, **fig. S8B**). Cluster 5 exhibited a proliferative state characterized by high expression of cell cycle-associated genes. Among the non-proliferative microglial clusters, clusters 3 and 4 displayed the strongest DAM signatures, whereas cluster 2 displayed the weakest (**Fig. 4C**). Comparison of these microglial clusters to previous analyses (*13*) further corroborated that clusters 3 and 4 most closely resemble neurodegeneration-associated DAM states, whereas cluster 2 aligns closer to a homeostatic phenotype and cluster 5 to a proliferative state (**fig. S8C**).

Pseudotime analysis indicated a trajectory from cluster 2, representing the homeostatic state, toward either cluster 3 and cluster 4, or cluster 1, reflecting dynamic transitions in microglial states in response to α-synuclein pathology (**Fig. 4A**). Differential gene expression analysis showed that cluster 3, which exhibited the strongest DAM signature, was enriched for canonical DAM genes including *TYROBP*, *APOE*, and the PD GWAS candidate *GPNMB* as well as antigen-presenting genes such as *B2M* and the PD GWAS-linked genes *HLA-DRB1* and *HLA-DQ* (**Fig. 4D**, **fig. S8D; table S4**). Cluster 4 was enriched for *TLR4* and complement components *C1QB* (**Fig. 4D**, **fig. S8D; table S4**).

To uncover molecular pathways underlying the divergent pseudotime trajectories, we performed GO cellular component analysis on branch-specific differentially expressed genes (**Fig. 4E; table S5**). The trajectory toward cluster 3 and 4 was enriched in ferritin complexes, autolysosomal and endolysosomal membranes, MHC complexes, and mitochondrial subunits. In contrast, the trajectory toward cluster 1 showed enrichment for complement components (especially C1), ribosomal and rough ER subunits, cytosolic small ribonucleoprotein particles, and secretory granules, suggesting a microglial state characterised by enhanced protein synthesis and secretion, particularly of complement proteins such as *C1Q*. We validated the up-regulation of DAM-associated genes *CHIT1 (P* = 0.0145)*, LGALS3 (P* = 0.0407)*, GPNMB (P* = 0.0171) by qPCR in n=3 additional differentiations per iPSC-MG line (**Fig. 4F**). Increased *GPNMB* expression was further confirmed when MG were co-cultured with DAN^{TRIP} relative to isogenic control neurons (*P* = 0.0247) (**fig. S8E**)

The PD GWAS candidate gene *GPNMB* was highly expressed in DAM microglial clusters 3 and 4, and its expression increased along this pseudotime trajectory (black line in **Fig. 4G** and **4A**). We confirmed using ELISA (**Fig. 4H**) and immunoblotting (**fig. S8F**) that GPNMB protein is up-regulated in MG^{HC}-DAN^{TRIP} co-culture lysates with minimal detection in DAN^{TRIP} monocultures in n=3 further independent differentiations per iPSC-MG line ($P < 0.0001$). In further control experiments, we tested and confirmed that *GPNMB* mRNA levels were minimally detected in DAN monocultures but were increased in co-cultures ($P < 0.0001$) (**fig. S8G**). We then investigated whether GPNMB is secreted, by measuring with ELISA GPNMB protein levels in conditioned media from DAN monocultures and MG-DAN co-cultures. These experiments showed that GPNMB was similarly secreted in MG-DAN co-cultures irrespective of the extent of neuronal aggregation

but was barely detectable in DAN conditioned media at baseline or after seeding with fibrils **(Fig. 4I).**

GPNMB interacts with α-synuclein in MG, promotes aggregate clearance and is up-regulated in post-mortem substantia nigra tissue from patients with PD

We next assessed whether GPNMB is involved in aggregate clearance. Using a proximity ligation assay, we found that GPNMB interacted with $pSyn^{+}$ aggregates in MG rather than DANs under both non-seeded ($P = 0.0003$) and seeded ($P = 0.0006$) conditions (**Fig. 5A, 5B**). To investigate the function of GPNMB in microglial-mediated clearance of $pSyn^{+}$aggregates, we used our doxycycline-inducible CRISPRi system to selectively knock down *GPNMB* expression in healthy control MG. Knockdown was achieved via lentiviral transduction of iPSCs with a pool of three gRNAs targeting distinct regions of the *GPNMB* promoter (**fig. S9A-C**), followed by differentiation into MG and subsequent co-culture with DAN^{TRIP}. Continuous doxycycline treatment from Day 1 of differentiation resulted in a 66% reduction in GPNMB protein levels in the co-culture system upon gRNA expression (±gRNA) as measured by ELISA ($P < 0.0001$) (**Fig. 5C**). This degree of *GPNMB* knockdown in MG was sufficient to block the clearance of neuronal $pSyn^{+}$ aggregates as measured by time-resolved FRET (**Fig. 5D and fig. S9D**). *GPNMB* knockdown, did not affect MG morphology or MG interactions with neurons in the co-cultures (**fig. S9E-F**). Collectively, these data suggest that GPNMB is a critical effector of α-synuclein aggregate clearance by MG.

Finally, we confirmed that GPNMB is predominantly expressed in IBA1-positive microglia in the substantia nigra of healthy control (81%), incidental Lewy body (iLB; 92%), and PD (87%) brains based on the % $GPNMB^{+}$ voxels overlapping $IBA1^{+}$ voxels (**Fig. 5E**, **5F**, **table S6**). Furthermore, we found that within the IBA^{+} microglia, GPNMB levels were

significantly increased in a graded manner with lowest voxels detected in HC, intermediate in iLB ($P = 0.0253$) and highest in PD ($P < 0.0001$) (**Fig. 5G**).

Autocrine regulation of microglia by IL-10 limits α-synuclein aggregate clearance.

To identify potential secreted regulators of the microglial phenotype, we used a membrane-based proteome array of 105 cytokines and chemokines and analysed their relative detected intensity (AU) in pooled co-culture conditioned media from three independent differentiations at D73. This analysis identified 48 differentially secreted cytokines in the conditioned media of fibril-seeded co-cultures compared to non-seeded co-cultures (**Fig. 6A**). We observed high levels of IL-10 under conditions of seeded aggregation relative to non-seeded baseline (**Fig. 6B**). Tumour Necrosis Factor-α (TNFα), a key cytokine of microglial-mediated cytotoxicity, that is down-regulated by IL-10 signalling (*36*), was not detectable under these conditions, in contrast to what was seen earlier in LPS-treated co-cultures (**Fig. 2P**).

We confirmed by ELISA that addition of fibrillar but not monomeric α-synuclein significantly increased IL-10 secretion in iPSC-derived MG monocultures ($P < 0.0001$) (**Fig. 6C**). Blocking the action of IL-10 in MG monocultures with anti-IL10 receptor alpha (anti-IL-10Rα) antibodies (1 μg/ml) significantly increased the degradation of α-synuclein fibrils when compared to non-targeting control (NTC) IgG ($P = 0.0183$) (**Fig. 6D**). Thus, IL-10 may act as an autocrine negative regulator of microglial degradation of α-synuclein fibrils. In the MG^{HC}-DAN^{TRIP} model, we first showed that IL-10 was detectable only in the conditioned media from co-cultures, not DAN^{TRIP} monocultures, and significantly increased further when MG were co-cultured with fibril-seeded DAN^{TRIP} that exhibit more extensive α-synuclein aggregation ($P = 0.0016$) (**Fig. 6E**). We then assessed the effect of anti-IL-10Rα blocking antibodies (1 μg/ml) for the 2-week duration of the co-culture of MG with DAN^{TRIP}

406 that were previously seeded with fibrils. This analysis revealed a dose-dependent reduction in pSyn levels, indicating that blocking IL-10 signalling enhances microglial-induced
408 clearance of $pSyn^+$ aggregates when compared to NTC IgG ($P = 0.0038$) (**Fig. 6F**). In control experiments, we tested and confirmed that IL-10Rα blockade did not have a direct effect on
410 $pSyn^+$ aggregates in neuronal monocultures (**Fig. 6G**). We also assessed factors that were strongly released across co-culture conditions such as MCP-1 (using inhibitor RS504393, 2
412 μM), SPP1 (using anti-SPP1 antibody, 5 μg/ml), and MMP9 (using inhibitor MMP9i 444278, 5 μM). These treatments did not modify microglial clearance of neuronal pSyn
414 aggregates (**fig. S10A** and **S10B**).

To assess whether IL-10 signalling influences microglial activation, we performed -
416 qPCR in co-cultures treated with either anti-IL10Rα or NTC IgG antibodies under fibril-induced aggregation conditions. This analysis showed that blocking IL-10Rα significantly
418 increased the expression of target genes identified in scRNAseq including *GPNMB* ($P = 0.0035$) as well as *CD22* ($P = 0.0034$) and *P2RY12* ($P = 0.0013$) (**Fig. 6H** and **fig. S10C**).
420 It is noteworthy, that LPS treatment, which is associated with a cytotoxic state, does not up-regulate *GPNMB* expression in either microglial monoculture (**fig. S10D**) or in fibril-treated
422 co-cultures (**fig. S10E**). The IL-10 induced upregulation of GPNMB was further confirmed by ELISA ($P = 0.0027$) (**Fig. 6I**). To functionally delineate this signalling cascade, we added
424 anti-IL10Rα antibodies to co-cultures where *GPNMB* was specifically knocked down in MG using CRISPRi. We found that knockdown of GPNMB muted the effect of IL-10 blockade
426 on aggregate clearance (**Fig. 6J, fig. S10F**). These findings suggest that IL-10 acts as an autocrine negative regulator of GPNMB-mediated microglial clearance of neuronal α-
428 synuclein aggregates.

430

DISCUSSION

Most research on microglia in PD has involved the study of animal models or short-term rodent co-culture systems, whereas the chronic response of human microglia to aggregate-laden human DANs is unknown. We developed iPSC-derived microglia and DAN co-cultures to determine microglial mechanisms of aggregate clearance in the human condition. Our findings identify distinct microglial states that exert beneficial effects, challenging the dominant view from animal studies, that in PD microglial activation is principally detrimental (*9, 37*).

A key finding of our study is that microglia trogocytose α-synuclein aggregates from the neuronal sub-compartment where they reside, based on the detection of $pSyn^{+}$, $synapsin^{+}$ (pre-synaptic) and $MAP2^{+}$ (somatodendritic) puncta within microglia and the requirement for direct contact between the two cell types. Initial α-synuclein aggregates in animal models (*38*) and human PD brain (*39*) localise predominantly in presynaptic terminals, raising the possibility that these are the earliest sites of microglial trogocytosis. Presynaptic microglial trogocytosis was previously shown to remodel synapses (*40*). Our study uncovers some of the underpinning signals and suggests that MG trogocytose intraneuronal aggregates throughout the neuronal compartments. This allows microglia to preserve neuronal integrity while simultaneously clearing toxic species. Our data suggest that this action is mediated by lysosomal degradation but is not detectably compromised by PD-associated $LRRK2^{G2019S}$ or GBA^{N370S} mutations in MG. Similarly, $SNCA^{TRIP}$ in MG did not affect pSyn clearance, cathepsin B activity or TNFα secretion under the conditions tested. However, further studies across additional iPSC clones and lines will be important to fully exclude a potential modifier effect. LPS activated MG secreted TNFα and triggered neuronal death, demonstrating that prolonged or over-activation is detrimental in this model, as previously suggested in other model systems (*30, 41*).

Multiple mechanisms of α-synuclein uptake by microglia have been described, primarily in rodent models such as endocytosis of secreted α-synuclein (*5, 42*) or tunnelling nanotube–mediated transfer (*43*). It is possible that such mechanisms also contribute in our human model, especially in the early stages as direct contact between microglia and neurons was required for the removal of intraneuronal aggregates. However, the mechanism we identified also differs substantially in that it is unaffected by TREM2 knockout or the LRRK2^{G2019S} mutation, two genes that regulate tunnelling nanotube mediated transfer from neurons to MG (*18*). Additionally, blockade of neuronal phosphatidylserine, a well-established generic "eat-me" signal via microglial TREM2 (*31*), had no impact on aggregate removal in agreement with the dispensability of TREM2 in our system. Whether these differences are due to species- or context-specific mechanisms of microglial function remains to be seen. Phosphatidylserine blockage prevented microglial phagocytosis of GABA neurons but not DANs, suggesting that microglia utilise different receptor repertoire for interactions with different types of neurons (*44*).

Instead, we found that trogocytosis is more nuanced and mediated by multiple effectors acting in concert, including sensing signals via P2RY12 and negative regulation via the sialic-acid–binding immunoglobulin-like lectin CD22 and the anti-inflammatory cytokine IL-10. *P2RY12* gene variants have been implicated in PD pathogenesis (*45*) and CD22 was previously identified in animal models as an age-related negative regulator of microglial phagocytosis including removal of α-synuclein aggregates (*12*). IL-10 levels are increased in the blood of patients with PD (*46*) and IL-10 over-expression in animal models increased α-synuclein aggregate burden and reduced survival (*47*). It is likely that additional mechanisms contribute such as remodelling of the ECM by neurons and signals from neighbouring glia, including microglia subtypes with secretory function as suggested by our transcriptomic profiling. This withstanding, our study demonstrates that signals such as

CD22 and IL-10 may act as brakes on microglial surveillance or activation to ensure it remains proportionate to the extent of neuronal pathology. Therefore, their graded inhibition could restore or amplify degradative capacity, especially in the presence of proteopathic stress. Defining this regulatory "sweet spot" of microglial activation is critical for designing therapeutics to enhance aggregate clearance while minimising inflammatory damage.

We found that aggregate clearance coincided with a shift in microglial morphology and gene expression profile. The microglial morphological transformation to a less ramified, more amoeboid state is consistent with the long held observation in post-mortem PD brains (*48*) . This was accompanied in our model by up-regulation of DAM markers, including lysosomal and phagocytic genes and innate immune receptors, which have been implicated in neurodegeneration (*49*). Although DAM signalling may be broadly conserved across neurodegenerative diseases, our results suggest that the DAM response is also adapted to α-synuclein pathology. For example, unlike its critical microglial function in AD (*11, 50*), TREM2 was not required for α-synuclein aggregate clearance in our model and it is not an established risk gene in PD (*32, 33*). Microglia in our model retained clearance competence without inducing neuronal death, despite up-regulation of DAM-associated genes, as evident by the up-regulation and retained function of the homeostatic gene *P2RY12* and the lack of TNFα secretion. We identified two transcriptionally distinct trajectories that diverge along separate paths in pseudotime analysis. The first trajectory was marked by upregulation of *C1Q*, a key initiator of the classical complement cascade traditionally involved in developmental synaptic pruning (*51*) and genes implicated in endosomal sorting, protein synthesis and secretion. The second trajectory, encompassing clusters 3 and 4, was expanded under conditions of increased aggregate abundance and displayed the DAM-like profile. This includes upregulation of *APOE*, *APOC1*, *LGALS3*, *CHIT1*, *FTH1*, and *FTL*, genes linked to lipid metabolism, phago-lysosomal degradation, and iron sequestration,

506 which are dysregulated in PD and other neurodegenerative conditions. The enrichment of *HLA-DRB1*, a well-established GWAS locus for PD risk (*52*), alongside other MHC class II
508 genes in cluster 3, which exhibits the strongest DAM signature, suggest a role for MHC-II–mediated microglial immunosurveillance in response to α-synuclein pathology. *HLA-DR* is
510 highly expressed in reactive microglia in the substantia nigra of post-mortem PD brains (*53*). Therefore, subtypes of microglia in our model may secret regulatory signals or actively
512 process and present antigenic material, potentially α-synuclein peptides (*54*), suggesting that the response we detected in culture could be further modified in vivo by signals from
514 adaptive immunity or systemic inflammation (*55*).

An important finding is the identification of GPNMB as a key effector of microglial
516 aggregate clearance. *GPNMB* is a PD GWAS candidate gene (*56, 57*) and one of the most strongly up-regulated genes in our microglial cluster 3 and 4. In postmortem brain, GPNMB
518 immunoreactivity was increased specifically in microglia in the substantia nigra with α-synuclein pathology, in agreement with findings in animal models (*58, 59*). *GPNMB* gene
520 knockout studies in animal models of α-synuclein pathology did not reveal a modifier action (*60*), whereas studies in iPSC-derived neurons suggested that loss of *GPNMB* prevents the
522 uptake of α-synuclein fibrils and α-synuclein pathology (*57*). Our data show that GPNMB is highly expressed in microglia both in culture and in post-mortem brains, with minimal
524 detection in neurons and it is required for efficient clearance of aggregates. Furthermore, *GPNMB* expression was regulated by an autocrine feedback loop involving IL-10 (**fig.**
526 **S10G**). Thus, in agreement with our findings in post-mortem brains, our mechanistic investigations suggest a microglia-centric role for GPNMB in PD. Specifically, we found
528 that GPNMB protein is minimally detected in DANs, and it is not up-regulated in neurons upon fibril exposure. Instead, GPNMB is upregulated in microglia when co-cultured with
530 neurons previously seeded with fibrils. GPNMB was shown in other cell types to interact

with extracellular matrix components such as syndecans (*61*) that were up-regulated in our model in neurons contacting MG. Although GPNMB is secreted under baseline conditions, potentially to modulate immune responses (*62*), we did not detect increased secretion when MG were co-cultured with fibril-seeded neurons. Using proximity ligation assay, we identified an interaction between GPNMB and pSyn within microglia. Thus, GPNMB is retained intracellularly upon binding to $pSyn^{+}$ aggregates, facilitating lysosomal degradation, as previously shown in other contexts (*63, 64*), rather than contributing to aggregate spread (*57*). This underscores the importance of cell-type resolved and species-specific modelling in response to intraneuronal pathology when evaluating microglial gene function in complex diseases such as PD. Future experiments combining intracellular knockdown with extracellular GPNMB addition would help to more fully define the function of distinct GPNMB proteoforms.

There are limitations to our study. While our iPSC-based co-culture system enables dissection of human-specific neuron–microglia interactions, it does not fully recapitulate the multicellular and systemic complexity of the intact brain. Systemic factors may influence the full manifestation of pathogenic mutations and genetic modifiers in vivo. However, given well-established species differences in microglial biology, such human models provide a complementary and potentially more translationally relevant platform to interrogate disease mechanisms. Our modelling involved primarily DAN^{TRIP} and generalisation to sporadic synucleinopathies and different neuronal subtypes requires further investigation. In this regard, our findings in post-mortem human substantia nigra support a role for microglial GPNMB in sporadic PD.

In summary, our findings indicate that microglia deploy multiple regulatory checkpoints to fine-tune the trogocytosis of intraneuronal aggregates, revealing tractable therapeutic nodes in PD, including modulation of P2RY12 and GPNMB or suppression of

IL-10 and CD22 signalling. Effective translation of these strategies will require accessible biomarkers capable of resolving microglial state transitions and guiding stage-specific intervention across the course of the disease.

MATERIALS AND METHODS

Study Design

The objective of this study was to define mechanisms by which human microglia respond to and clear intraneuronal α-synuclein aggregates. Human iPSC-derived dopaminergic neurons and microglia were used in monoculture and co-culture systems to model endogenous α-synuclein aggregation caused by *SNCA* triplication or aggregation induced by exogenous α-synuclein fibrils. Experimental outcomes included quantification of α-synuclein aggregation, neuronal viability, microglial activation, transcriptomic changes, cytokine secretion, and aggregate clearance. Mechanistic studies were performed using pharmacological inhibitors, blocking antibodies, and inducible CRISPRi-mediated knockdown of candidate genes. Findings were assessed in postmortem human substantia nigra tissue from neurologically healthy controls, individuals with incidental Lewy body disease, and individuals with Parkinson's disease (n=3 per group). Human iPSC lines and postmortem tissues were selected based on genotype and tissue availability and were not randomised. For in vitro experiments, treatment allocation was predetermined by experimental design. Investigators were blinded during image acquisition and data analysis. For single-cell RNA sequencing analyses, low-quality cells, ambient RNA–contaminated droplets, and doublets were excluded according to predefined quality-control criteria; no additional outliers were excluded. No statistical methods were used to predetermine sample size. Sample sizes were based on previous experience with iPSC differentiation experiments and functional assays. All experiments were independently replicated using multiple

differentiations and, where indicated, independent iPSC lines. Biological replicate numbers are provided in the figure legends. Ethical approval for the use of human tissue, provided by the Oxford Brain Bank, was obtained from the Oxford C REC Ethics Committee (no. 15/SC/0639). Ethics Committees that approved the iPSC lines used in this study: for healthy control donors, National Health Service, Health Research Authority, NRES Committee South Central, Berkshire, UK, REC 10/H0505/71, and for SNCA patients REC 07/H0720/161. All experiments were performed in accordance with UK guidelines and regulations and as set out in the REC.

Statistical Analysis

All statistical analyses were performed using GraphPad Prism 8 (GraphPad Software Inc., USA). Data were examined for normality, and appropriate statistical tests were selected accordingly. For normally distributed data, one-sample *t*-test, two-sided unpaired Student's *t*-test or one-way ANOVA were used as shown. For non-normally distributed data, Wilcoxon Signed-Rank Test or the Kruskal–Wallis test was applied. The null hypothesis was rejected at a significance level of $P = 0.05$. Statistical significance in single cell analyses was assessed using Fisher's Exact test, and multiple testing correction was applied using the false discovery rate (FDR) method. Only the top 20 terms based on fold enrichment score with FDR-adjusted P values < 0.05 were included. In experiments involving iPSC lines, biological replicates (*n*) were defined as one independent differentiation per iPSC line. Differentiations yielded either microglial monocultures, dopaminergic neuron monocultures, or co-cultures containing both cell types. Individual level data are presented in data file S1.

List of Supplementary Materials

Supplementary Methods

Supplementary Figures S1-S10

Supplementary Tables S1-S8

Data File S1

MDAR Checklist

REFERENCES and Notes

1. G. K. Tofaris, Initiation and progression of α-synuclein pathology in Parkinson's disease. *Cellular and molecular life sciences* 79, 210 (2022).
2. D. Zenko, J. Marsh, A. R. Castle, R. Lewin, R. Fischer, G. K. Tofaris, Monitoring α-synuclein ubiquitination dynamics reveals key endosomal effectors mediating its trafficking and degradation. *Science Advances* 9, eadd8910 (2023).
3. Y. C. Wong, D. Krainc, α-synuclein toxicity in neurodegeneration: mechanism and therapeutic strategies. *Nature medicine* 23, 1-13 (2017).
4. H.-J. Lee, S. Patel, S.-J. Lee, Intravesicular localization and exocytosis of α-synuclein and its aggregates. *Journal of Neuroscience* 25, 6016-6024 (2005).
5. I. Choi, Y. Zhang, S. P. Seegobin, M. Pruvost, Q. Wang, K. Purtell, B. Zhang, Z. Yue, Microglia clear neuron-released α-synuclein via selective autophagy and prevent neurodegeneration. *Nature communications* 11, 1386 (2020).
6. S. Krasemann, C. Madore, R. Cialic, C. Baufeld, N. Calcagno, R. El Fatimy, L. Beckers, E. O'loughlin, Y. Xu, Z. Fanek, The TREM2-APOE pathway drives the transcriptional phenotype of dysfunctional microglia in neurodegenerative diseases. *Immunity* 47, 566-581. e569 (2017).
7. C. Kim, D.-H. Ho, J.-E. Suk, S. You, S. Michael, J. Kang, S. Joong Lee, E. Masliah, D. Hwang, H.-J. Lee, Neuron-released oligomeric α-synuclein is an endogenous agonist of TLR2 for paracrine activation of microglia. *Nature communications* 4, 1562 (2013).
8. A. Flury, L. Aljayousi, H.-J. Park, M. Khakpour, J. Mechler, S. Aziz, J. D. McGrath, P. Deme, C. Sandberg, F. G. Ibáñez, A neurodegenerative cellular stress response linked to dark microglia and toxic lipid secretion. *Neuron*, (2024).
9. W. Zhang, T. Wang, Z. Pei, D. S. Miller, X. Wu, M. L. Block, B. Wilson, W. Zhang, Y. Zhou, J.-S. Hong, Aggregated α-synuclein activates microglia: a process leading to disease progression in Parkinson's disease. *The FASEB Journal* 19, 533-542 (2005).
10. J. V. Pluvinage, M. S. Haney, B. A. Smith, J. Sun, T. Iram, L. Bonanno, L. Li, D. P. Lee, D. W. Morgens, A. C. Yang, CD22 blockade restores homeostatic microglial phagocytosis in ageing brains. *Nature* 568, 187-192 (2019).
11. H. Keren-Shaul, A. Spinrad, A. Weiner, O. Matcovitch-Natan, R. Dvir-Szternfeld, T. K. Ulland, E. David, K. Baruch, D. Lara-Astaiso, B. Toth, A unique microglia type

associated with restricting development of Alzheimer's disease. *Cell* 169, 1276-1290. e1217 (2017).
12. I. M. Chiu, E. T. Morimoto, H. Goodarzi, J. T. Liao, S. O'Keeffe, H. P. Phatnani, M. Muratet, M. C. Carroll, S. Levy, S. Tavazoie, A neurodegeneration-specific gene-expression signature of acutely isolated microglia from an amyotrophic lateral sclerosis mouse model. *Cell reports* 4, 385-401 (2013).
13. M.-J. Dolan, M. Therrien, S. Jereb, T. Kamath, V. Gazestani, T. Atkeson, S. E. Marsh, A. Goeva, N. M. Lojek, S. Murphy, Exposure of iPSC-derived human microglia to brain substrates enables the generation and manipulation of diverse transcriptional states in vitro. *Nature Immunology* 24, 1382-1390 (2023).
14. N. Sun, M. B. Victor, Y. P. Park, X. Xiong, A. N. Scannail, N. Leary, S. Prosper, S. Viswanathan, X. Luna, C. A. Boix, Human microglial state dynamics in Alzheimer's disease progression. *Cell* 186, 4386-4403. e4329 (2023).
15. Y. Huang, K. E. Happonen, P. G. Burrola, C. O'Connor, N. Hah, L. Huang, A. Nimmerjahn, G. Lemke, Microglia use TAM receptors to detect and engulf amyloid β plaques. *Nature immunology* 22, 586-594 (2021).
16. D. Gosselin, D. Skola, N. G. Coufal, I. R. Holtman, J. C. Schlachetzki, E. Sajti, B. N. Jaeger, C. O'Connor, C. Fitzpatrick, M. P. Pasillas, An environment-dependent transcriptional network specifies human microglia identity. *Science* 356, eaal3222 (2017).
17. L. Geirsdottir, E. David, H. Keren-Shaul, A. Weiner, S. C. Bohlen, J. Neuber, A. Balic, A. Giladi, F. Sheban, C.-A. Dutertre, Cross-species single-cell analysis reveals divergence of the primate microglia program. *Cell* 179, 1609-1622. e1616 (2019).
18. H. Scheiblich, F. Eikens, L. Wischhof, S. Opitz, K. Jüngling, C. Cserép, S. V. Schmidt, J. Lambertz, T. Bellande, B. Pósfai, Microglia rescue neurons from aggregate-induced neuronal dysfunction and death through tunneling nanotubes. *Neuron*, (2024).
19. W. Haenseler, F. Zambon, H. Lee, J. Vowles, F. Rinaldi, G. Duggal, H. Houlden, K. Gwinn, S. Wray, K. C. Luk, Excess α-synuclein compromises phagocytosis in iPSC-derived macrophages. *Scientific reports* 7, 9003 (2017).
20. B. Tanudjojo, S. S. Shaikh, A. Fenyi, L. Bousset, D. Agarwal, J. Marsh, C. Zois, S. Heman-Ackah, R. Fischer, D. Sims, Phenotypic manifestation of α-synuclein strains derived from Parkinson's disease and multiple system atrophy in human dopaminergic neurons. *Nature communications* 12, 3817 (2021).
21. W. Haenseler, S. N. Sansom, J. Buchrieser, S. E. Newey, C. S. Moore, F. J. Nicholls, S. Chintawar, C. Schnell, J. P. Antel, N. D. Allen, A highly efficient human pluripotent stem cell microglia model displays a neuronal-co-culture-specific expression profile and inflammatory response. *Stem cell reports* 8, 1727-1742 (2017).
22. J. D. Welch, V. Kozareva, A. Ferreira, C. Vanderburg, C. Martin, E. Z. Macosko, Single-cell multi-omic integration compares and contrasts features of brain cell identity. *Cell* 177, 1873-1887. e1817 (2019).
23. X. Wang, J. Park, K. Susztak, N. R. Zhang, M. Li, Bulk tissue cell type deconvolution with multi-subject single-cell expression reference. *Nature communications* 10, 380 (2019).
24. O. Butovsky, M. P. Jedrychowski, C. S. Moore, R. Cialic, A. J. Lanser, G. Gabriely, T. Koeglsperger, B. Dake, P. M. Wu, C. E. Doykan, Identification of a unique TGF-β–dependent molecular and functional signature in microglia. *Nature neuroscience* 17, 131-143 (2014).
25. M. Mittelbronn, K. Dietz, H. Schluesener, R. Meyermann, Local distribution of microglia in the normal adult human central nervous system differs by up to one order of magnitude. *Acta neuropathologica* 101, 249-255 (2001).

26. H. Fujiwara, M. Hasegawa, N. Dohmae, A. Kawashima, E. Masliah, M. S. Goldberg, J. Shen, K. Takio, T. Iwatsubo, α-Synuclein is phosphorylated in synucleinopathy lesions. *Nature cell biology* 4, 160-164 (2002).
27. M. Jonikas, M. Madill, A. Mathy, T. Zekoll, C. E. Zois, S. Wigfield, M. Kurzawa-Akanbi, C. Browne, D. Sims, P. F. Chinnery, S. A. Cowley, G. K. Tofaris, Stem cell modeling of mitochondrial parkinsonism reveals key functions of OPA1. *Ann Neurol* 83, 915-925 (2018).
28. H. Lee, R. Flynn, I. Sharma, E. Haberman, P. J. Carling, F. J. Nicholls, M. Stegmann, J. Vowles, W. Haenseler, R. Wade-Martins, LRRK2 is recruited to phagosomes and co-recruits RAB8 and RAB10 in human pluripotent stem cell-derived macrophages. *Stem Cell Reports* 14, 940-955 (2020).
29. H. J. Fernandes, E. M. Hartfield, H. C. Christian, E. Emmanoulidou, Y. Zheng, H. Booth, H. Bogetofte, C. Lang, B. J. Ryan, S. P. Sardi, ER stress and autophagic perturbations lead to elevated extracellular α-synuclein in GBA-N370S Parkinson's iPSC-derived dopamine neurons. *Stem cell reports* 6, 342-356 (2016).
30. W.-G. Kim, R. P. Mohney, B. Wilson, G.-H. Jeohn, B. Liu, J.-S. Hong, Regional difference in susceptibility to lipopolysaccharide-induced neurotoxicity in the rat brain: role of microglia. *Journal of Neuroscience* 20, 6309-6316 (2000).
31. J. Rueda-Carrasco, D. Sokolova, S. E. Lee, T. Childs, N. Jurčáková, G. Crowley, S. De Schepper, J. Z. Ge, J. I. Lachica, C. E. Toomey, Microglia-synapse engulfment via PtdSer-TREM2 ameliorates neuronal hyperactivity in Alzheimer's disease models. *The EMBO journal* 42, e113246 (2023).
32. C. M. Lill, A. Rengmark, L. Pihlstrøm, I. Fogh, A. Shatunov, P. M. Sleiman, L. S. Wang, T. Liu, C. F. Lassen, E. Meissner, The role of TREM2 R47H as a risk factor for Alzheimer's disease, frontotemporal lobar degeneration, amyotrophic lateral sclerosis, and Parkinson's disease. *Alzheimer's & Dementia* 11, 1407-1416 (2015).
33. S. Rayaprolu, B. Mullen, M. Baker, T. Lynch, E. Finger, W. W. Seeley, K. J. Hatanpaa, C. Lomen-Hoerth, A. Kertesz, E. H. Bigio, TREM2 in neurodegeneration: evidence for association of the p. R47H variant with frontotemporal dementia and Parkinson's disease. *Molecular neurodegeneration* 8, 1-5 (2013).
34. S. E. Haynes, G. Hollopeter, G. Yang, D. Kurpius, M. E. Dailey, W.-B. Gan, D. Julius, The P2Y12 receptor regulates microglial activation by extracellular nucleotides. *Nature neuroscience* 9, 1512-1519 (2006).
35. B. Pósfai, E. Szabadits, C. Cserép, S. Vida, A. D. Schwarcz, R. Fekete, K. Tóth, O. Bánkövi, C. Szekeres-Paraczky, Z. Maglóczky, P2Y12 Receptor Function Governs Microglial Surveillance and Cell–Cell Interactions in the Cerebral Cortex. *Glia* 74, e70109 (2026).
36. D.-I. Shin, U. Banning, Y.-M. Kim, J. Verheyen, M. Hannen, H. Bönig, D. Körholz, Interleukin 10 inhibits TNF-alpha production in human monocytes independently of interleukin 12 and interleukin 1 beta. *Immunological investigations* 28, 165-175 (1999).
37. M. F. Duffy, T. J. Collier, J. R. Patterson, C. J. Kemp, K. C. Luk, M. G. Tansey, K. L. Paumier, N. M. Kanaan, D. L. Fischer, N. K. Polinski, Lewy body-like alpha-synuclein inclusions trigger reactive microgliosis prior to nigral degeneration. *Journal of neuroinflammation* 15, 1-18 (2018).
38. G. K. Tofaris, P. G. Reitböck, T. Humby, S. L. Lambourne, M. O'Connell, B. Ghetti, H. Gossage, P. C. Emson, L. S. Wilkinson, M. Goedert, Pathological changes in dopaminergic nerve cells of the substantia nigra and olfactory bulb in mice transgenic for truncated human α-synuclein (1–120): implications for Lewy body disorders. *Journal of Neuroscience* 26, 3942-3950 (2006).
39. W. J. Schulz-Schaeffer, The synaptic pathology of α-synuclein aggregation in dementia with Lewy bodies, Parkinson's disease and Parkinson's disease dementia. *Acta neuropathologica* 120, 131-143 (2010).

40. L. Weinhard, G. di Bartolomei, G. Bolasco, P. Machado, N.L. Schieber, U. Neniskyte, M. Exiga, A. Vadisiute, A. Raggioli, A. Schertel, Y. Schwab, C.T. Gross, Microglia remodel synapses by presynaptic trogocytosis and spine head filopodia induction. *Nature communications* 9, 1228 (2018).
41. B. Nimmervoll, R. White, J.-W. Yang, S. An, C. Henn, J.-J. Sun, H. J. Luhmann, LPS-induced microglial secretion of TNFα increases activity-dependent neuronal apoptosis in the neonatal cerebral cortex. *Cerebral Cortex* 23, 1742-1755 (2013).
42. H.-J. Lee, J.-E. Suk, E.-J. Bae, S.-J. Lee, Clearance and deposition of extracellular α-synuclein aggregates in microglia. *Biochemical and biophysical research communications* 372, 423-428 (2008).
43. H. Scheiblich, C. Dansokho, D. Mercan, S. V. Schmidt, L. Bousset, L. Wischhof, F. Eikens, A. Odainic, J. Spitzer, A. Griep, Microglia jointly degrade fibrillar alpha-synuclein cargo by distribution through tunneling nanotubes. *Cell* 184, 5089-5106. e5021 (2021).
44. K. Hakim-Mishnaevski, N. Flint-Brodsly, B. Shklyar, F. Levy-Adam, E. Kurant, Glial phagocytic receptors promote neuronal loss in adult Drosophila brain. *Cell Reports* 29, 1438-1448. e1433 (2019).
45. K. d. P. Lopes, G. J. Snijders, J. Humphrey, A. Allan, M. A. Sneeboer, E. Navarro, B. M. Schilder, R. A. Vialle, M. Parks, R. Missall, Genetic analysis of the human microglial transcriptome across brain regions, aging and disease pathologies. *Nature genetics* 54, 4-17 (2022).
46. X.-Y. Qin, S.-P. Zhang, C. Cao, Y. P. Loh, Y. Cheng, Aberrations in peripheral inflammatory cytokine levels in Parkinson disease: a systematic review and meta-analysis. *JAMA neurology* 73, 1316-1324 (2016).
47. S. G. Cockey, K. N. McFarland, E. J. Koller, M. M. Brooks, E. Gonzalez De La Cruz, P. E. Cruz, C. Ceballos-Diaz, A. M. Rosario, Y. R. Levites, D. R. Borchelt, Il-10 signaling reduces survival in mouse models of synucleinopathy. *npj Parkinson's Disease* 7, 30 (2021).
48. T. G. Beach, L. I. Sue, D. G. Walker, L. F. Lue, D. J. Connor, J. N. Caviness, M. N. Sabbagh, C. H. Adler, Marked microglial reaction in normal aging human substantia nigra: correlation with extraneuronal neuromelanin pigment deposits. *Acta neuropathologica* 114, 419-424 (2007).
49. M. T. Heneka, M. P. Kummer, E. Latz, Innate immune activation in neurodegenerative disease. *Nature Reviews Immunology* 14, 463-477 (2014).
50. Y. Zhou, W. M. Song, P. S. Andhey, A. Swain, T. Levy, K. R. Miller, P. L. Poliani, M. Cominelli, S. Grover, S. Gilfillan, Human and mouse single-nucleus transcriptomics reveal TREM2-dependent and TREM2-independent cellular responses in Alzheimer's disease. *Nature medicine* 26, 131-142 (2020).
51. B. Stevens, N. J. Allen, L. E. Vazquez, G. R. Howell, K. S. Christopherson, N. Nouri, K. D. Micheva, A. K. Mehalow, A. D. Huberman, B. Stafford, The classical complement cascade mediates CNS synapse elimination. *Cell* 131, 1164-1178 (2007).
52. Y. Le Guen, G. Luo, A. Ambati, V. Damotte, I. Jansen, E. Yu, A. Nicolas, I. De Rojas, T. Peixoto Leal, A. Miyashita, Multiancestry analysis of the HLA locus in Alzheimer's and Parkinson's diseases uncovers a shared adaptive immune response mediated by HLA-DRB1* 04 subtypes. *Proceedings of the National Academy of Sciences* 120, e2302720120 (2023).
53. P. L. McGeer, S. Itagaki, B. E. Boyes, E. McGeer, Reactive microglia are positive for HLA-DR in the substantia nigra of Parkinson's and Alzheimer's disease brains. *Neurology* 38, 1285-1285 (1988).
54. D. Sulzer, R. N. Alcalay, F. Garretti, L. Cote, E. Kanter, J. Agin-Liebes, C. Liong, C. McMurtrey, W. H. Hildebrand, X. Mao, T cells from patients with Parkinson's disease recognize α-synuclein peptides. *Nature* 546, 656-661 (2017).

55. A. S. Harms, Y.-T. Yang, M. G. Tansey, Central and peripheral innate and adaptive immunity in Parkinson's disease. *Science translational medicine* 15, eadk3225 (2023).
56. M. A. Nalls, C. Blauwendraat, C. L. Vallerga, K. Heilbron, S. Bandres-Ciga, D. Chang, M. Tan, D. A. Kia, A. J. Noyce, A. Xue, Identification of novel risk loci, causal insights, and heritable risk for Parkinson's disease: a meta-analysis of genome-wide association studies. *The Lancet Neurology* 18, 1091-1102 (2019).
57. M. E. Diaz-Ortiz, Y. Seo, M. Posavi, M. Carceles Cordon, E. Clark, N. Jain, R. Charan, M. D. Gallagher, T. L. Unger, N. Amari, GPNMB confers risk for Parkinson's disease through interaction with α-synuclein. *Science* 377, eabk0637 (2022).
58. E. B. Moloney, A. Moskites, E. J. Ferrari, O. Isacson, P. J. Hallett, The glycoprotein GPNMB is selectively elevated in the substantia nigra of Parkinson's disease patients and increases after lysosomal stress. *Neurobiology of disease* 120, 1-11 (2018).
59. S. Smajić, C. A. Prada-Medina, Z. Landoulsi, J. Ghelfi, S. Delcambre, C. Dietrich, J. Jarazo, J. Henck, S. Balachandran, S. Pachchek, Single-cell sequencing of human midbrain reveals glial activation and a Parkinson-specific neuronal state. *Brain* 145, 964-978 (2022).
60. R. Brendza, H. Lin, K. Stark, O. Foreman, J. Tao, A. Pierce, H. Ngu, K. Shen, A. E. Easton, T. Bhangale, Genetic ablation of Gpnmb does not alter synuclein-related pathology. *Neurobiology of Disease* 159, 105494 (2021).
61. S. Shikano, M. Bonkobara, P. K. Zukas, K. Ariizumi, Molecular cloning of a dendritic cell-associated transmembrane protein, DC-HIL, that promotes RGD-dependent adhesion of endothelial cells through recognition of heparan sulfate proteoglycans. *Journal of Biological Chemistry* 276, 8125-8134 (2001).
62. V. M. Ripoll, K. M. Irvine, T. Ravasi, M. J. Sweet, D. A. Hume, Gpnmb is induced in macrophages by IFN-γ and lipopolysaccharide and acts as a feedback regulator of proinflammatory responses. *The Journal of Immunology* 178, 6557-6566 (2007).
63. R. L. Wallings, D. A. Gillett, H. A. Staley, S. Mahn, J. Mark, N. Neighbarger, H. Kordasiewicz, W. D. Hirst, M. G. Tansey, ASO-mediated knock-down of GPNMB in mutant-GRN and in Grn-deficient peripheral myeloid cells disrupts lysosomal function and immune responses. *Molecular Neurodegeneration* 20, 41 (2025).
64. M. Liu, J. Zhu, J. Zheng, X. Han, L. Jiang, X. Tong, Y. Ke, Z. Guo, W. Huang, J. Cong, M. Liu, S.-Y. Lin, S. Zhu, L. Mei, X. Zhang, W. Zhang, W.-J. Xin, Z. Zhang, Y. Guo, R. Chen, GPNMB and ATP6V1A interact to mediate microglia phagocytosis of multiple types of pathological particles. *Cell Reports* 44, (2025).
65. S. Sabate-Soler, S. L. Nickels, C. Saraiva, E. Berger, U. Dubonyte, K. Barmpa, Y. J. Lan, T. Kouno, J. Jarazo, G. Robertson, Microglia integration into human midbrain organoids leads to increased neuronal maturation and functionality. *Glia* 70, 1267-1288 (2022).
66. M. A. Horlbeck, L. A. Gilbert, J. E. Villalta, B. Adamson, R. A. Pak, Y. Chen, A. P. Fields, C. Y. Park, J. E. Corn, M. Kampmann, Compact and highly active next-generation libraries for CRISPR-mediated gene repression and activation. *elife* 5, e19760 (2016).
67. C. Soneson, M. I. Love, M. D. Robinson, Differential analyses for RNA-seq: transcript-level estimates improve gene-level inferences. *F1000Research* 4, 1521 (2016).
68. A. T. Lun, S. Riesenfeld, T. Andrews, T. P. Dao, T. Gomes, P. i. t. s. H. C. A. Jamboree, J. C. Marioni, EmptyDrops: distinguishing cells from empty droplets in droplet-based single-cell RNA sequencing data. *Genome biology* 20, 1-9 (2019).

69. S. Yang, S. E. Corbett, Y. Koga, Z. Wang, W. E. Johnson, M. Yajima, J. D. Campbell, Decontamination of ambient RNA in single-cell RNA-seq with DecontX. *Genome biology* 21, 1-15 (2020).
70. P. Germain, A. Lun, C. Garcia Meixide, W. Macnair, M. Robinson, Doublet identification in single-cell sequencing data using scDblFinder [version 2; peer review: 2 approved]. *F1000Research* 10, (2022).
71. Y. Hao, T. Stuart, M. H. Kowalski, S. Choudhary, P. Hoffman, A. Hartman, A. Srivastava, G. Molla, S. Madad, C. Fernandez-Granda, Dictionary learning for integrative, multimodal and scalable single-cell analysis. *Nature biotechnology* 42, 293-304 (2024).
72. S. X. Ge, D. Jung, R. Yao, ShinyGO: a graphical gene-set enrichment tool for animals and plants. *Bioinformatics* 36, 2628-2629 (2020).
73. D. Aran, A. P. Looney, L. Liu, E. Wu, V. Fong, A. Hsu, S. Chak, R. P. Naikawadi, P. J. Wolters, A. R. Abate, Reference-based analysis of lung single-cell sequencing reveals a transitional profibrotic macrophage. *Nature immunology* 20, 163-172 (2019).
74. V. A. Traag, L. Waltman, N. J. Van Eck, From Louvain to Leiden: guaranteeing well-connected communities. *Scientific reports* 9, 1-12 (2019).
75. G. Finak, A. McDavid, M. Yajima, J. Deng, V. Gersuk, A. K. Shalek, C. K. Slichter, H. W. Miller, M. J. McElrath, M. Prlic, MAST: a flexible statistical framework for assessing transcriptional changes and characterizing heterogeneity in single-cell RNA sequencing data. *Genome biology* 16, 1-13 (2015).
76. J. F. Tuddenham, M. Taga, V. Haage, V. S. Marshe, T. Roostaei, C. White, A. J. Lee, M. Fujita, A. Khairallah, Y. Zhang, A cross-disease resource of living human microglia identifies disease-enriched subsets and tool compounds recapitulating microglial states. *Nature Neuroscience*, 1-17 (2024).
77. S. A. Miller, R. A. Policastro, S. Sriramkumar, T. Lai, T. D. Huntington, C. A. Ladaika, D. Kim, C. Hao, G. E. Zentner, H. M. O'Hagan, LSD1 and aberrant DNA methylation mediate persistence of enteroendocrine progenitors that support BRAF-mutant colorectal cancer. *Cancer research* 81, 3791-3805 (2021).
78. Ó. González-Velasco, M. Simon, R. Yilmaz, R. Parlato, J. Weishaupt, C. D. Imbusch, B. Brors, Identifying similar populations across independent single cell studies without data integration. *bioRxiv*, 2024.2009. 2027.615367 (2024).
79. K. Street, D. Risso, R. B. Fletcher, D. Das, J. Ngai, N. Yosef, E. Purdom, S. Dudoit, Slingshot: cell lineage and pseudotime inference for single-cell transcriptomics. *BMC genomics* 19, 1-16 (2018).
80. K. Van den Berge, H. Roux de Bézieux, K. Street, W. Saelens, R. Cannoodt, Y. Saeys, S. Dudoit, L. Clement, Trajectory-based differential expression analysis for single-cell sequencing data. *Nature communications* 11, 1201 (2020).

Acknowledgements: We thank Eli Lilly & Co for the anti-TREM2 antibodies.

Funding: This study was funded by an MRC Senior Clinical Fellowship (MR/V007068/1), the National Institute for Health Research (NIHR) Oxford Biomedical Research Centre and Innovative Medicines Initiative 2 Joint Undertaking under grant agreement

No 116060 (IMPRiND) to GKT. HJC was supported by the Oxford-Taiwan Graduate Scholarship. AK was funded by a NDCN studentship partly supported by Eli Lilly. The James and Lillian Martin Centre for Stem Cell Research (S.A.C.) is supported by the James Martin 21st Century Research Foundation. The opinions expressed and arguments employed herein do not necessarily reflect the official views of the funding bodies.

Author Contributions: H-J.C., A.K., A.A-G., C.L.L collected, analysed, and interpreted data for the study. S.A.C interpreted data. L.T., A.J., D.A., D.S. performed bioinformatic analysis. H-J.C. and G.K.T. prepared the manuscript with input from all authors. G.K.T. analysed and interpreted data and was responsible for the design and supervision of the study.

Competing Interests: The authors declare that they have no competing interests.

Data and materials availability: All data needed to evaluate the conclusions in the study are presented in the paper and the Supplementary Materials. RNASeq data were deposited to GEO under the accession numbers GSE290525, GSE299790 and GSE299369. The anti-TREM2 antibodies used in this study were made available under a Material transfer Agreement with Eli Lilly. Requests for the dox inducible dCas9-KRAB iPSC line and other resources or reagents should be directed to and will be fulfilled by the lead contact, subject to completion of the required institutional material transfer agreement. All other iPSC lines are available from EBiSC. All other materials are commercially available or will be made available upon reasonable request.

940 **FIGURE LEGENDS**

942

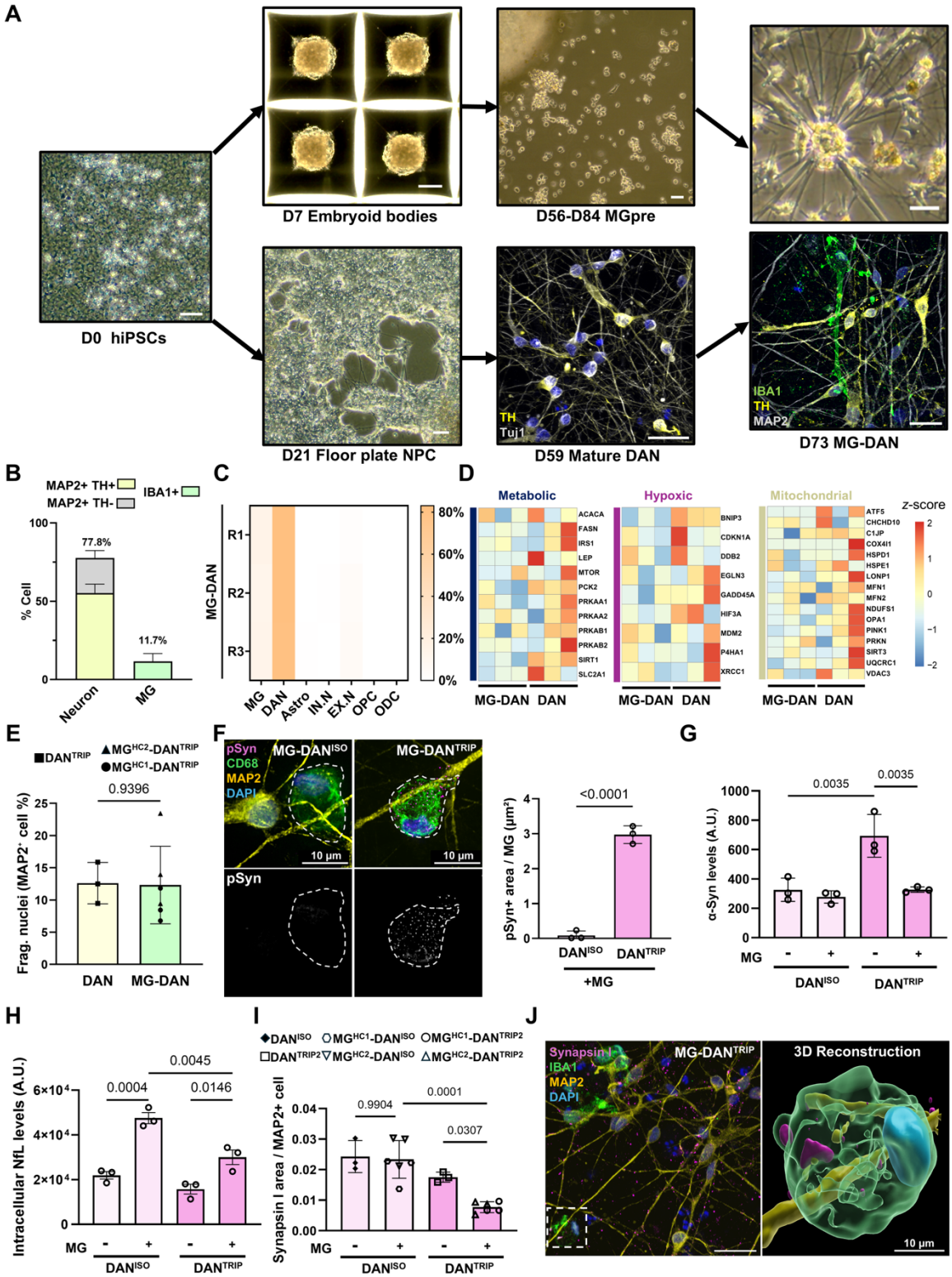

944

Fig. 1 Human iPSC-based modelling of long-term interactions between microglia and

946 **dopaminergic neurons reveals a protective response.**

(A) Schematic illustration of the co-culture model. Macrophage precursors (MGpre), generated from iPSC-derived embryoid bodies, were added to DAN cultures at D59 and differentiated into microglia (MG) during two weeks of co-culture. Transcriptomic analysis, immunofluorescence and all cellular assays were performed at D73. Immunostaining confirmed the presence of $IBA1^+$ MG and TH^+ DANs in co-cultures.

(B) Immunostaining quantification showing the percentage of microglia ($IBA1^+$) and the percentage of DAN (TH^+) and other $MAP2^+$ neurons in the co-culture (n = 3 independent differentiations for MG^{HC1}-DAN^{TRIP1}).

(C) Heatmap showing cell-type deconvolution of bulk RNA-seq data using the MuSiC algorithm. Relative proportions (%) of microglia (MG), dopaminergic neurons (DAN), astrocytes (Astro), inhibitory neurons (IN.N), excitatory neurons (EX.N), oligodendrocyte precursor cells (OPC), and oligodendrocytes (ODC) in the co-culture. R1–R3 denote three independent differentiations for MG^{HC1}-DAN^{TRIP1}.

(D) Bulk RNA-seq heatmaps for metabolic, oxidative, and mitochondrial stress signatures in MG^{HC1}-DAN^{TRIP1} co-cultures compared to DAN^{TRIP1} monocultures.

(E) Quantification of the percentage of $MAP2^+$ cells with fragmented nuclei in DAN^{TRIP1} monocultures versus MG^{HC1}- DAN^{TRIP1} co-cultures (n=3 independent differentiations)

(F) Representative instant structured illumination microscopy (iSIM) images and quantification showing $pSyn^+$ puncta within $CD68^+$ MG^{HC} co-cultured with DAN^{TRIP} or DAN^{ISO} (n = 3 independent differentiation for MG^{HC1}-DAN^{ISO} and MG^{HC1}-DAN^{TRIP2}).

(G) Quantification of total α-synuclein by ELISA in cell lysates from DAN monocultures and MG-DAN co-cultures (n = 3 independent differentiations for DAN^{ISO}, DAN^{TRIP2}, MG^{HC1}-DAN^{ISO} and MG^{HC1}-DAN^{TRIP2}).

(H) Quantification of NfL by MSD electrochemiluminescence in cell lysates from DAN monocultures and MG-DAN co-cultures (n = 3 independent differentiations for DAN^{ISO}, DAN^{TRIP2}, MG^{HC1}-DAN^{ISO} and MG^{HC1}-DAN^{TRIP2}).

(I) Quantification of total Synapsin I area in DAN monocultures and MG-DAN co-cultures (n = 3 independent differentiations for DAN^{ISO}, DAN^{TRIP2}, MG^{HC1}-DAN^{ISO} and MG^{HC1}-DAN^{TRIP2}).

(J) Representative 3D reconstruction from confocal images showing Synapsin I^+ and $MAP2^+$ puncta within $IBA1^+$MG co-cultured with DAN^{TRIP}.

All graphs show mean ± SD and were analysed by two-tailed t-test (**E, F**) or one-way ANOVA (**G, H, I**) followed by Tukey's post hoc test. *Scale bar,* 20 μm unless otherwise specified.

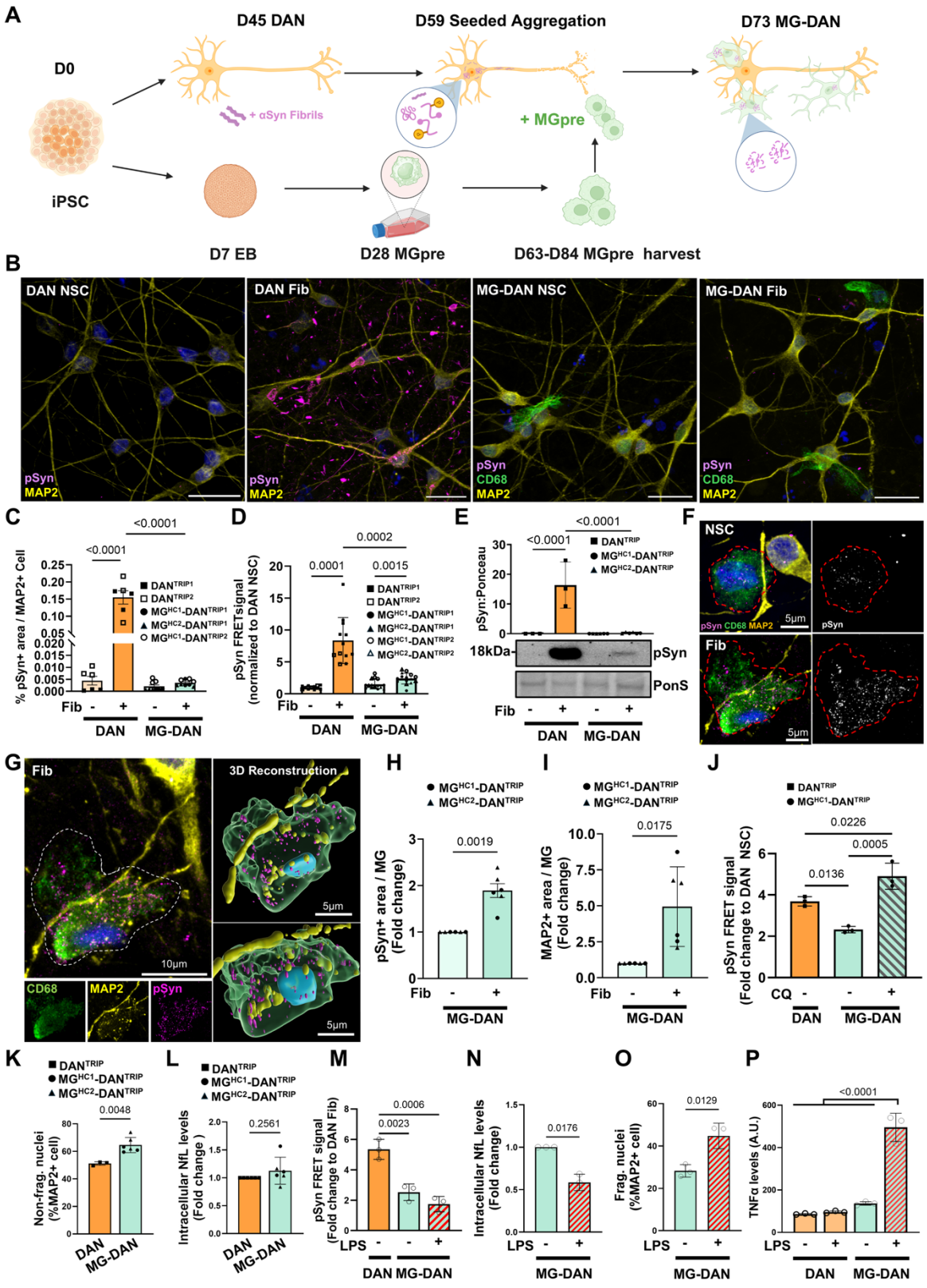

Fig. 2 Microglia promote the clearance of fibril-seeded intraneuronal α-synuclein aggregates

(A) Schematic diagram of the co-culture model. iPSC-derived DANs were seeded with fibrils at D45 and cultured for 2 weeks to allow the formation of abundant pSyn+ aggregates. Macrophage precursors (MGpre), differentiated from iPSC-derived embryoid

bodies, were added to the fibril-seeded DANs at D59, and matured into microglia during the subsequent 2 weeks of co-culture, until D73.

(B) Representative immunostaining of pSyn (magenta), CD68 (green), and MAP2 (yellow) in DAN and MG-DAN co-culture under non-seeded (NSC) or fibril-seeded (Fib) conditions.

(C) Quantification of the total $pSyn^+$ area per total scan area (% $pSyn^+$ area), normalised to $MAP2^+$ neuron count (n = 3 independent differentiations for DAN^{TRIP1}, DAN^{TRIP2}, MG^{HC1}-DAN^{TRIP1}, MG^{HC2}-DAN^{TRIP1} and MG^{HC1}-DAN^{TRIP2}).

(D) Quantification of pSyn signal by time-resolved FRET for each condition as indicated. Fibril-seeded DANs were co-cultured with MG (n=9 for DAN^{TRIP1}, n=3 for DAN^{TRIP2}, n=6 for MG^{HC1}-DAN^{TRIP1}, n=3 for MG^{HC1}-DAN^{TRIP2}, n=3 for MG^{HC2}-DAN^{TRIP1}, n=3 for MG^{HC2}-DAN^{TRIP2}).

(E) Representative immunoblot of RIPA-insoluble fraction showing pSyn levels in DAN monocultures compared to MG^{HC}-DAN^{TRIP} co-cultures under fibril-seeded conditions (n = 3 independent differentiations for DAN^{TRIP1}, MG^{HC1}-DAN^{TRIP1} and MG^{HC2}-DAN^{TRIP1}).

(F) Representative Airyscan super-resolution images, showing $pSyn^+$ puncta within $CD68^+$ MG co-cultured with DANs under fibril-seeded conditions.

(G) 3D reconstruction of Airyscan super-resolution image of MG co-cultured with DANs under fibril-seeded conditions in **(F)**, showing the presence of $pSyn^+$ puncta and $MAP2^+$ puncta within $CD68^+$ MG.

(H) Quantification of $pSyn^+$ area within $CD68^+$ MG (n = 3 independent differentiations for MG^{HC1}-DAN^{TRIP1} and MG^{HC2}-DAN^{TRIP1}).

(I) Quantification of $MAP2^+$ area within $CD68^+$ MG (n = 3 independent differentiations for MG^{HC1}-DAN^{TRIP1} and MG^{HC2}-DAN^{TRIP1}).

(J) Quantification of pSyn signal by time-resolved FRET at baseline and following chloroquine (CQ) treatment (10 μM) of MG^{HC}-DAN^{TRIP} co-cultures (n = 3 independent differentiations for DAN^{TRIP1} and MG^{HC1}-DAN^{TRIP1}).

(K) Quantification of the percentage of $MAP2^+$ cells with non-fragmented nuclei in DAN^{TRIP} monocultures versus MG^{HC}- DAN^{TRIP} co-cultures under seeded conditions (n=3 independent differentiations for DAN^{TRIP1}, MG^{HC1}-DAN^{TRIP1} and MG^{HC2}-DAN^{TRIP1}).

(L) Quantification of NfL by MSD electrochemiluminescence in cell lysates from DAN^{TRIP} monocultures and MG^{HC}-DAN^{TRIP} co-cultures under fibril-seeded conditions (n = 3 independent differentiations for DAN^{TRIP1}, MG^{HC1}-DAN^{TRIP1} and MG^{HC2}-DAN^{TRIP1}).

(M) Quantification of pSyn by time-resolved FRET in LPS-treated co-cultures (n = 3 independent differentiations for DAN^{TRIP2} and MG^{ISO}-DAN^{TRIP2}).

(N) Quantification of NfL by MSD electrochemiluminescence in cell lysates from DAN^{TRIP} monocultures and MG^{HC}-DAN^{TRIP} co-cultures at baseline and following LPS treatment (n = 3 independent differentiations for MG^{ISO}-DAN^{TRIP2}).

(O) Percentage of fragmented neuronal nuclei in MG^{HC}-DAN^{TRIP} co-cultures at baseline and after LPS treatment (n = 3 independent differentiations for MG^{ISO}-DAN^{TRIP2}).

(P) TNFα levels in DAN^{TRIP} monocultures and MG^{HC}-DAN^{TRIP} co-cultures at baseline and after LPS treatment (n = 3 independent differentiations for DAN^{TRIP2} and MG^{ISO}-DAN^{TRIP2}).

All graphs show mean ± SD and were analysed by one sample t-test (**H, I, L, O**), two-tailed t-test (**K, P**) or one-way ANOVA (**C**, **D**, **E**, **J, M, N**) followed by Tukey's post hoc test. *Scale bar,* 20 μm unless otherwise specified.

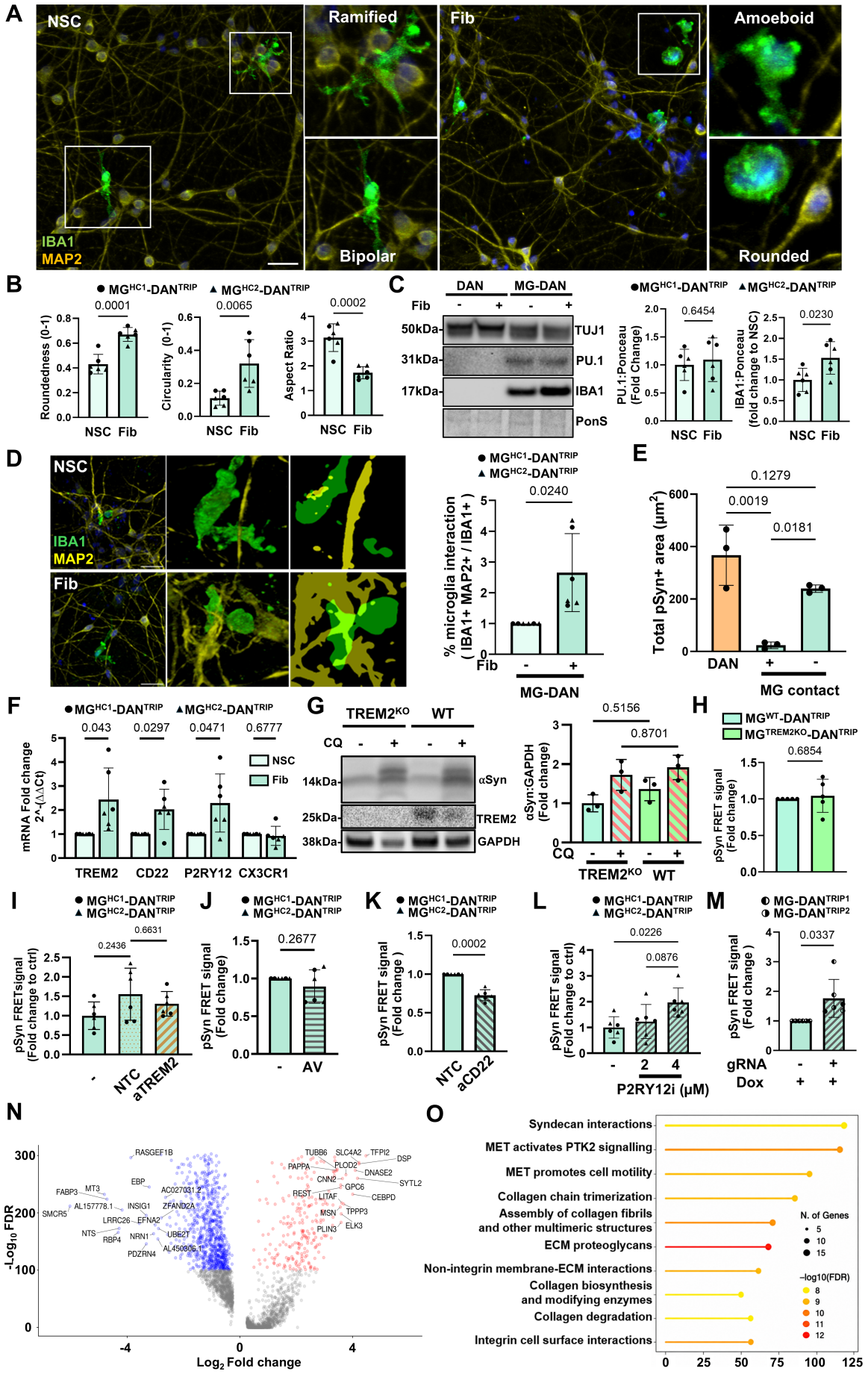
A
NSC
Ramified
Fib
Amoeboid
IBA1
MAP2
Bipolar
Rounded
B
MG^HC1-DAN^TRIP
MG^HC2-DAN^TRIP
0.0001
0.0065
0.0002
Roundedness (0-1)
Circularity (0-1)
Aspect Ratio
NSC Fib
C
DAN
MG-DAN
Fib
50kDa
31kDa
17kDa
TUJ1
PU.1
IBA1
PonS
0.6454
0.0230
PU.1:Ponceau (Fold Change)
IBA1:Ponceau (fold change to NSC)
D
NSC
IBA1
MAP2
Fib
0.0240
% microglia interaction (IBA1+ MAP2+ / IBA1+)
MG-DAN
E
0.1279
0.0019
0.0181
Total pSyn+ area (µm2)
DAN
MG contact
F
0.043
0.0297
0.0471
0.6777
mRNA Fold change 2^-(ΔΔCt)
TREM2
CD22
P2RY12
CX3CR1
G
TREM2^KO
WT
CQ
14kDa
25kDa
38kDa
αSyn
TREM2
GAPDH
0.5156
0.8701
αSyn:GAPDH (Fold change)
H
MG^WT-DAN^TRIP
MG^TREM2KO-DAN^TRIP
0.6854
pSyn FRET signal (Fold change)
I
0.2436
0.6631
pSyn FRET signal (Fold change to ctrl)
NTC
aTREM2
J
0.2677
pSyn FRET signal (Fold change)
AV
K
0.0002
pSyn FRET signal (Fold change)
NTC
aCD22
L
0.0226
0.0876
pSyn FRET signal (Fold change to ctrl)
P2RY12i (µM)
M
MG-DAN^TRIP1
MG-DAN^TRIP2
0.0337
pSyn FRET signal (Fold change)
gRNA
Dox
N
-Log10 FDR
Log2 Fold change
RASGEF1B
EBP
FABP3
MT3
AC027031.2
SMCR5
AL157778.1
INSIG1
ZFAND2A
LRRC26
EFNA2
NTS
RBP4
NRN1
UBE2T
PDZRN4
AL450806.1
TUBB6
SLC4A2
TFPI2
DSP
PAPPA
PLOD2
DNASE2
CNN2
SYTL2
GPC6
REST
LITAF
CEBPD
MSN
TPPP3
PLIN3
ELK3
O
Syndecan interactions
MET activates PTK2 signalling
MET promotes cell motility
Collagen chain trimerization
Assembly of collagen fibrils and other multimeric structures
ECM proteoglycans
Non-integrin membrane-ECM interactions
Collagen biosynthesis and modifying enzymes
Collagen degradation
Integrin cell surface interactions
N. of Genes
-log10(FDR)

Fig 3. Microglial activation in response to intraneuronal α-synuclein aggregation is TREM2-independent and involves contact mediated by P2RY12 and CD22

(A) Confocal images of IBA1^{+} MG in MG^{HC}-DAN^{TRIP} co-cultures exhibiting diverse morphologies, including ramified, bipolar, amoeboid, and rounded forms.

(B) Quantification of IBA1-masked MG for roundedness, circularity and aspect ratio under non-seeded (NSC) and fibril-seeded (Fib) conditions (n=3 independent differentiations for MG^{HC1}-DAN^{TRIP1} and MG^{HC2}-DAN^{TRIP1})

(C) Representative immunoblot and quantification of IBA1 and PU.1 in cell lysates, comparing MG^{HC}-DAN^{TRIP} co-cultures under fibril-seeded to NSC conditions (n =3 independent differentiations for MG^{HC1}-DAN^{TRIP1} and MG^{HC2}-DAN^{TRIP1}).

(D) Representative confocal images of MG^{HC}-DAN^{TRIP} co-cultures and corresponding 3D reconstructions with binary masks of the IBA1 and MAP2 channels, showing their overlap for quantitative analysis. Quantification using Mander's coefficient of the percentage overlap of IBA1 with MAP2 in each image stack (n = 3 independent differentiations for MG^{HC1}-DAN^{TRIP1} and MG^{HC2}-DAN^{TRIP1}).

(E) Total pSyn^{+} area, with or without separation of the MG with transwells (n = 3 independent differentiations for MG^{HC1}-DAN^{TRIP1}).

(F) qPCR analysis of relevant receptors (*TREM2*, *CD22*, *P2RY12*, *CX3CR1*) in fibril-seeded co-cultures, normalised to *GAPDH* and plotted relative to NSC conditions (n=3 independent differentiations for MG^{HC1}-DAN^{TRIP1} and MG^{HC2}-DAN^{TRIP1}).

(G) Immunoblotting of αSyn in TREM2 knockout (TREM2^{KO}) and isogenic WT MG monocultures at baseline and after treatment with chloroquine (50 μM) (n=3 independent differentiations for MG^{TREM2KO} and MG^{WT}).

(H) Quantification of pSyn by time-resolved FRET in cell lysates from DAN^{TRIP1} co-cultured with either TREM2^{KO} or isogenic WT control MG (n=5 independent differentiations for MG^{TREM2KO}-DAN^{TRIP1} and MG^{WT}-DAN^{TRIP1}).

(I) Quantification of pSyn by time-resolved FRET in cell lysates from MG^{HC}-DAN^{TRIP} co-cultures at baseline and after addition of TREM2 receptor blocking antibodies under fibril-seeded conditions (n = 3 independent differentiations for MG^{HC1}-DAN^{TRIP1} and MG^{HC2}-DAN^{TRIP1}).

(J) Quantification of pSyn time-resolved FRET in cell lysates from MG^{HC}-DAN^{TRIP} co-cultures at baseline and after Annexin V (AV) treatment under fibril-seeded conditions (n = 3 independent differentiations MG^{HC1}-DAN^{TRIP1} and MG^{HC2}-DAN^{TRIP1}).

(K) Quantification of pSyn by time-resolved FRET in cell lysates from MG^{HC}-DAN^{TRIP} co-cultures under fibril-seeded conditions when treated with anti-CD22 antibody (aCD22) compared to IgG non-targeting control (NTC) (n = 3 independent differentiations for MG^{HC1}-DAN^{TRIP1} and MG^{HC2}-DAN^{TRIP1}).

(L) Quantification of pSyn by time-resolved FRET, in cell lysates from MG^{HC}-DAN^{TRIP} co-cultures treated with an increasing concentrations of P2RY12 inhibitor (P2RY12i) or control under fibril-seeded conditions (n = 3 independent differentiations MG^{HC1}-DAN^{TRIP1} and MG^{HC2}-DAN^{TRIP1}).

(M) Time-resolved FRET quantification of pSyn in cell lysates from MG^{HC}–DAN^{TRIP} co-cultures following microglia-specific P2RY12 knockdown by CRISPRi under fibril-seeded conditions (n = 3 differentiations for MG^{dCas9}-DAN^{TRIP1} and MG^{dCas9}-DAN^{TRIP2}).

(N) Volcano plot of differentially expressed neuronal genes in MG^{HC}–DAN^{TRIP} co-cultures versus DAN^{TRIP} monocultures; red indicates upregulation, blue indicates downregulation.

(**O)** Gene ontology terms enriched in DANs when co-cultured with MG as determined by Single-cell RNA-seq analysis. Note enrichment of terms associated with extracellular matrix.

All graphs show mean ± SD and were analysed by one sample t-test (**D, F, J, H, K, M**) two-tailed t-test (**B, C, H**), one-way ANOVA (**E, G, I, L**) followed by Tukey's post hoc test. *Scale bar*, 20 μm unless otherwise specified.

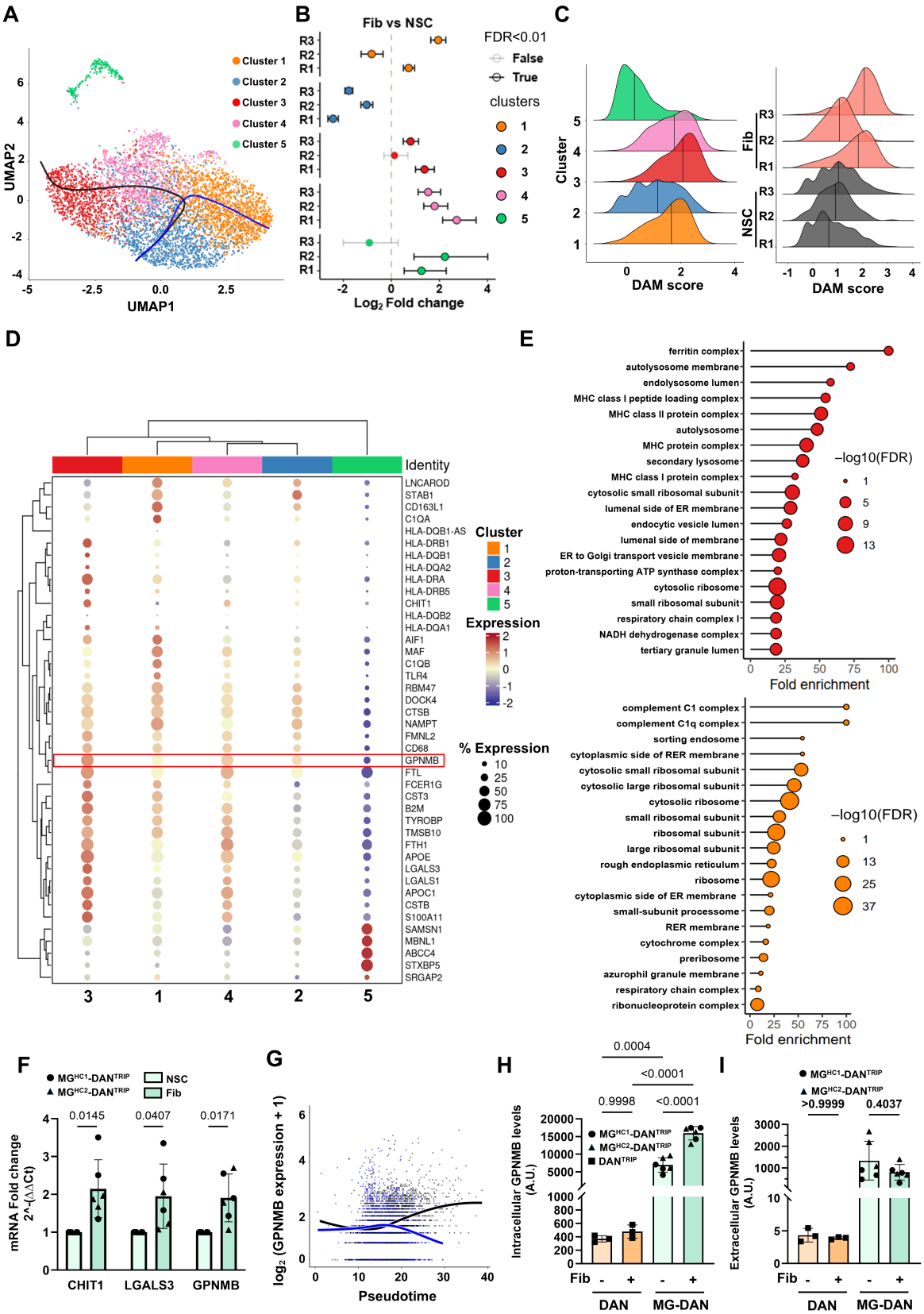

1142

Fig 4. Single-cell RNA sequencing identifies clusters of α-synuclein-related DAM.

1144 **(A)** UMAP visualisation of MG single-cell transcriptomes revealed 5 distinct clusters and 2 pseudo-time trajectories.

(B) Log_2 fold change in MG cluster abundance between NSC- and fibril-seeded conditions. Open circles indicate FDR < 0.01. R1–R3 denote three independent differentiations for MG^{HC1}-DAN^{TRIP1}.

(C) DAM signature module scores for microglial clusters 1 to 5 (left) and for microglia in NSC and fibril-seeded conditions (right). R1–R3 denote three independent differentiations for MG^{HC1}-DAN^{TRIP1}. Vertical lines indicate group medians. p <0.0001

(D) Dot plot summarising the average expression (blue-to-brown colour scale) and percentage of cells (dot size) expressing the top marker genes for each microglial cluster. Marker genes were identified by pairwise differential-expression testing with MAST, distinguishing each cluster from every other cluster. Note the high expression of *GPNMB* in clusters 3 and 4.

(E) Gene ontology (GO) analysis of cellular component terms showing the top 20 categories ranked by fold enrichment score (adjusted p <0.05) across pseudotime along the two branches originating from cluster 2: the trajectory toward clusters 3 and 4 (upper panel) and the trajectory toward cluster 1 (lower panel).

(F) *CHIT1*, *LGALS3*, and *GPNMB* expression in MG^{HC}–DAN^{TRIP} quantified by qPCR under fibril-seeded conditions (n=3 independent differentiations for MG^{HC1}-DAN^{TRIP1} and MG^{HC2}-DAN^{TRIP1}).

(G) Expression of *GPNMB* along the pseudotime trajectories. Smoothed trend lines indicate the fitted expression trajectories across pseudotime (black line toward clusters 3 and 4; blue line toward cluster 1). Each dot represents one cell; y-axis shows log2-transformed GPNMB expression; x-axis shows pseudotime.

(H) Quantification of GPNMB protein levels by ELISA in cell lysates from DAN^{TRIP} monocultures and MG^{HC}–DAN^{TRIP} co-cultures at baseline and under fibril-seeded (Fib) conditions (n = 3 independent differentiations for DAN^{TRIP1}, MG^{HC1}-DAN^{TRIP1} and MG^{HC2}-DAN^{TRIP1}).

(I) Quantification of GPNMB protein levels by ELISA in conditioned media from DAN monocultures and MG-DAN co-cultures at baseline and under fibril-seeded (Fib) conditions (n = 3 independent differentiations for MG^{HC1}-DAN^{TRIP1} and MG^{HC2}-DAN^{TRIP1}).

All graphs show mean ± SD and were analysed by Mann–Whitney U test (**C**), one sample t-test (**F**), two-tailed t-test or one-way ANOVA (**H**, **I**) followed by Tukey's post hoc test. R1, R2, R3 refer to biological replicates from n=3 independent differentiations.

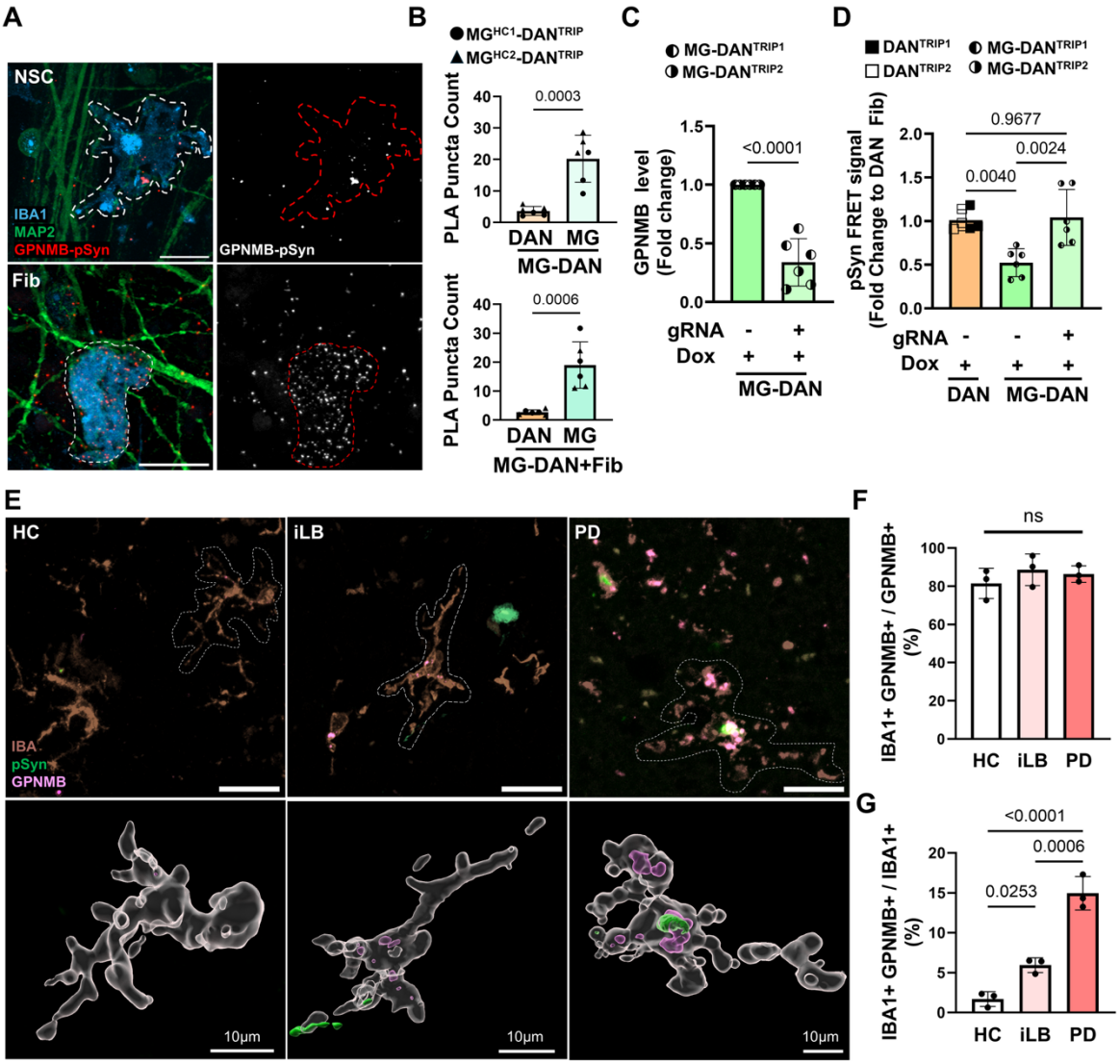

1192 **Fig 5. GPNMB interacts with α-synuclein and regulates aggregate clearance by MG.**

(A) Representative image of GPNMB and pSyn interaction (red) using proximity ligation
1194 assay with concomitant immunostaining for IBA1^{+} MG^{HC} (blue) and MAP2^{+} DAN^{TRIP} neurons (green) under non-seeded conditions (top) and Fib-seeded conditions (bottom).
1196 Right image in black and white shows the same field, highlighting the GPNMB–pSyn PLA puncta (n = 3 independent differentiations for MG^{HC1}-DAN^{TRIP1} and MG^{HC2}-DAN^{TRIP1})
1198

(B) Quantification of GPNMB and pSyn (red) interaction using proximity ligation assay in
1200 IBA1^{+} MG^{HC} and MAP2^{+} DAN^{TRIP} neurons under non-seeded (top) and fibril-seeded conditions (bottom) (n = 3 independent differentiations for MG^{HC1}-DAN^{TRIP1} and MG^{HC2}-
1202 DAN^{TRIP1}).

1204 **(C)** Quantification of GPNMB protein levels by ELISA levels in cell lysates from MG^{dCas9}-DAN^{TRIP} co-cultures (n = 3 independent differentiations for MG^{dCas9}-DAN^{TRIP1}
1206 and MG^{dCas9}-DAN^{TRIP2}).

1208 **(D)** Time-resolved FRET quantification of pSyn in cell lysates from MG^{dCas9}-DAN^{TRIP} co-cultures with or without GPNMB knockdown and in DAN^{TRIP} monocultures (n = 3

independent differentiations for DAN^{TRIP1}, DAN^{TRIP2}, MG^{dCas9}-DAN^{TRIP1} and MG^{dCas9}-DAN^{TRIP2}).

(E) Representative immunostaining for pSyn (green), IBA1 (brown), and GPNMB (magenta) in post mortem substantia nigra tissue from healthy donors (HC) and donors with incidental Lewy bodies (iLB) or PD. Lower panels show 3D reconstructions of identified $IBA1^+$ cells containing GPNMB and pSyn.

(F) Percentage of $GPNMB^+$ voxels overlapping $IBA1^+$ voxels in substantia nigra across HC, iLB, and PD (n=3 donors per group).

(G) Percentage of $IBA1^+$ voxels overlapping $GPNMB^+$ voxels in substantia nigra across HC, iLB, and PD (n=3 donors per group).

All graphs show mean ± SD and were analysed by two-tailed t-test (**B**), one sample t-test (**C**), one-way ANOVA (**D, F, G**) followed by Tukey's post hoc test. *Scale bar,* 20 μm unless otherwise specified.

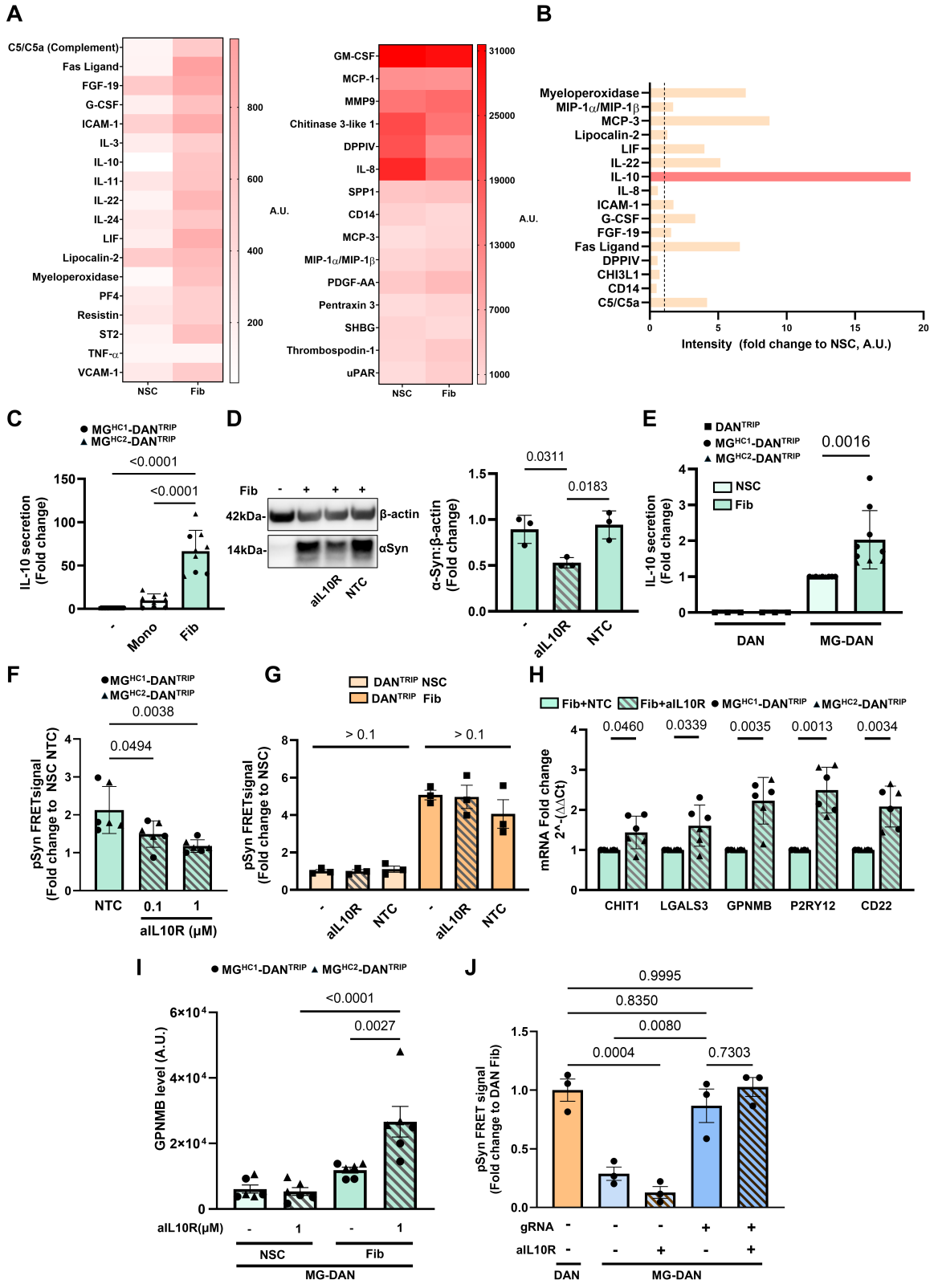

Fig 6. Autocrine regulation of microglia by IL-10 limits α-Synuclein aggregate clearance.

(A) Secretome analysis of MG^{HC}-DAN^{TRIP} co-cultures. Heatmaps showing cytokine signal abundance (AU) in conditioned media under non-seeded (NSC) and fibril-seeded (Fib) conditions.

(B) Quantification of secreted cytokines showing the largest fold change in MG^{HC}-DAN^{TRIP} co-culture conditioned media under Fib-seeded conditions relative to non-seeded controls (NSC).

(C) IL-10 secretion in conditioned media of MG monocultures as quantified by ELISA at baseline and after treatment with fibrils or monomeric αSyn (Mono) (n = 3 independent differentiations for MG^{HC1}-DAN^{TRIP1} and MG^{HC2}-DAN^{TRIP1}).

(D) Representative immunoblot and quantification of αSyn levels in cell lysates from MG monocultures treated with fibrils and either anti-IL10Rα antibody (1μg/ml) or isotype NTC IgG (n=3 for MG^{HC1}).

(E) IL-10 levels as quantified by ELISA in cell lysates from DAN^{TRIP} monocultures and MG^{HC}-DAN^{TRIP} co-cultures under non-seeded (NSC) or fibril-seeded (Fib) conditions. (n≥3 independent differentiations for DAN^{TRIP1}, MG^{HC1}-DAN^{TRIP1} and MG^{HC2}-DAN^{TRIP1}).

(F) Time-resolved FRET quantification of pSyn in cell lysates from fibril-seeded MG^{HC}-DAN^{TRIP} co-cultures treated with increasing concentrations of IL-10Rα blocking antibodies or NTC IgG (n=3 independent differentiations for MG^{HC1}-DAN^{TRIP1} and MG^{HC2}-DAN^{TRIP1}).

(G) Time-resolved FRET quantification of pSyn in cell lysates from DAN^{TRIP} monocultures under non-seeded (NSC) or fibril-seeded (Fib) conditions; cells were treated with 1 μg/ml anti-IL-10Rα or NTC IgG (n = 3 for DAN^{TRIP1}).

(H) qPCR analysis of DAM markers (*CHIT1*, *LGALS3*, *GPNMB*, *P2RY12, CD22*), normalised to *GAPDH*. Data show gene expression in anti-IL-10Rα or IgG (NTC) treated fibril-seeded MG^{HC}-DAN^{TRIP} co-cultures (n= 3 independent differentiations for MG^{HC1}-DAN^{TRIP1} and MG^{HC2}-DAN^{TRIP1}).

(I) Quantification of GPNMB protein levels by ELISA in cell lysates from MG^{HC}-DAN^{TRIP} co-cultures treated anti-IL-10Rα antibodies or NTC IgG, under non-seeded (NSC) or fibril-seeded (Fib) conditions (n = 3 independent differentiations for MG^{HC1}-DAN^{TRIP1} and MG^{HC2}-DAN^{TRIP1}).

(J) Time-resolved FRET quantification of pSyn in cell lysates from DAN monocultures and MG-DAN co-cultures. MG-DAN co-culture conditions included MG *GPNMB* knockdown or control ±IL-10 receptor blockade (aIL10R; n = 3 independent differentiations for DAN^{TRIP1} and MG^{dCas9}-DAN^{TRIP1}).

All graphs show mean ± SD and were analysed by one sample t-test (**H**) or one-way ANOVA (**C**, **D**, **E**, **F**, **G, I, J**) followed by Tukey's post hoc test.

Science Translational Medicine
AAAS

Supplementary materials for

Human microglia clear intraneuronal α-synuclein aggregates by GPNMB-mediated trogocytosis

Hung-Ju Chueh *et al.*

Corresponding author: Prof. George K. Tofaris (george.tofaris@ndcn.ox.ac.uk)

This PDF file includes:

Supplementary Material and Methods

Fig. S1 to S10

Table S1, S6, S7, S8

SUPPLEMENTARY MATERIALS AND METHODS

iPSC maintenance and differentiation of dopaminergic neurons and microglia

All iPSC cell lines have been previously characterised as summarised in **Table S1**. iPSCs were maintained in mTesR1 media (Stem Cell Technologies, 95957) and were differentiated into dopaminergic neurons using a protocol developed by Kriks et al. as adapted in our lab by Tanudjojo *et al.*(*24*). In summary, iPSCs were seeded on Geltrex-coated six-well plates and expanded to >80% confluency. The media were then switched from mTeSR1 to floor plate induction media until DIV (day in vitro) 12, consisting of 2 μM A83-01 (Tocris, 2939), 100 nM LDN (Sigma, SML0559), 300 ng/ml Sonic Hedgehog (Shh – R&D Systems, 464-SH-200), 2 μM purmorphamine (Tocris, 4551), 200 ng/ml FGF8a (R&D Systems, 4745-F8), and 3 μM CHIR-99021 (Tocris, 4423). From DIV 12, media were switched to dopaminergic neural differentiation and maturation media, consisting of 20 ng/ml BDNF (PeproTech, 450–02), 20 ng/ml GDNF (PeproTech, 450–10), 1 ng/ml TGFβ3 (Life Technologies, PHG9305), 10 μM DAPT (Tocris, 2634), 200 μM ascorbic acid (Sigma, A4403), and 500 μM dbcAMP (Sigma, D0627). At DIV20, cells were replated onto Geltrex-coated plates or coverslips. Starting from DIV21, media changes incorporated DIV11-19 components until the designated analysis timepoints.

Human microglia-like cells were derived from iPSCs using an established protocol (*19*). In summary, iPSCs were transferred to AgreWell800 plates (Stem Cell Technologies, 34811) when cultured to >90% confluency, with Embryoid Body (EB) medium consisting of 50 ng/ml Vascular endothelial growth factor (VEGF – Invitrogen, PHC9394), 50 ng/ml Bone morphogenetic protein 4 (BMP4 – Invitrogen, PHC9534), and 20 ng/ml Stem cell factor (SCF – Milteny, 130-096-692). On day 7, T175 flasks with 15 ml 'factory' differentiation medium were prepared. EBs from each AggreWell were transferred into two T175 flasks. EB medium was replaced with factory medium consisting of the X-vivo 15 medium (Lonza, BE02-060F) and small molecules including 25 ng/ml Interleukin-3 (IL3 – Invitrogen, PHC0033) and 100 ng/ml Macrophage stimulating factor (M-CSF – Invitrogen, PHC9501). Factory medium was added weekly (10–15 ml), with macrophage/microglia precursors (MGpre) emerging around days 14–28. Harvested cells were cultured for up to 2 weeks either as microglia monocultures (MG) or in co-culture with DANs (MG-DAN) at a 1:1 ratio. It has been previously demonstrated that certain components of iPSC-DAN medium are directly toxic to iPS-microglia (dbcAMP, TGFβ3) (*65*), and that GM-CSF is optional for the differentiation of microglia (*19*), so

these were not included in the coculture medium, and so the mono/co-culture medium consisted of Advanced DMEM/F12 and 100 ng/ml of Interleukin-34 (IL-34 – Peprotech, 200–34).

Generation of dCas9-KRAB iPSC-derived microglia

dCas9-KRAB HC iPSCs were generated by lentiviral transduction of dCas9-KRAB and M2rtTA into the AAVS1 locus (S7). dCas9-KRAB iPSCs were transduced in suspension with sgRNA lentivirus targeting P2RY12 or GPNMB. Transduced iPSCs were then selected with 1 μg/ml puromycin (Sigma, P8833) for 5 days or until 90–95% confluency was reached. sgRNA sequences were obtained from the hCRISPRi-v2.1 Weissman Laboratory Library (*66*). Transduced iPSCs were differentiated into microglia as described previously and treated with 1.5 μg/ml doxycycline (Sigma, D3447) every 48h to maintain dCas9 expression and gene knockdown until the final timepoints.

α-Synuclein purification and fibril assembly

Generation of α-synuclein (αSyn) fibrils was carried out following the method we described previously (*20*). In summary, the expression construct pRK172, encoding recombinant wild-type human αSyn was transformed into BL21 (DE3) E.Coli ((New England BioLabs, C2527H). The transformed cells were grown on ampicillin LB agar plate overnight. All grown colonies were collected and transferred into Terrific broth media. The bacteria were allowed to expand for 2.5 hours while shaking, after which 0.4 mM isopropyl β-d-1-thiogalactopyranoside (IPTG, VWR, 437144N) was added to induce αSyn expression followed by 5 hours of further incubation. Bacteria were then harvested and resuspended in low salt buffer [50 mM Tris-HCl, pH 7.4 (Santa Cruz Biotechnology, sc-301950), 20 mM NaCl (Sigma, S9888), 1 mM EDTA, 0.1 mM DTT, 0.1 mM PMSF (Calbiochem, 52332), and 2x cOmplete Protease Inhibitor Cocktail tablets (Roche, 04693116001)] containing 1 mg/ml lysozyme (Thermo Scientific, 89833), DNase (Invitrogen, 18047019), and RNase (Thermo Scientific, EN0601). Cells were lysed by sonication on ice (5 seconds on/5 seconds off, 40% amplitude) for 2 minutes. Cell debris were removed by centrifuging at 15,000 x g for 20 minutes at 4°C. Supernatant was collected and purified using a two-stage high-performance liquid chromatography. Supernatant was fractionated with a HiTrap Q HP anion exchange chromatography column (Cytiva, 17115401) followed by a HiLoad 16/600 Superdex 75 pg size exclusion chromatography column (Cytiva, 28-

9893-33). Fractions enriched in αSyn, identified by SDS-PAGE Coomassie stain and immunoblotting, were pooled and spin-concentrated at 400g for 8–12 hours at 4°C using a Vivaspin column (Cytiva, 28-9323-58). Buffer exchange was then done using a 50 mM/150 mM KCL solution. The concentration of the purified αSyn was measured using Pierce BCA assay kit (Thermo Scientific, 23225) per manufacturer's instructions and NanoDrop spectrophotometer (Thermo Scientific, ND-ONE-W) and diluted to 350 μM (5 mg/ml). The purified α-synuclein were assembled into fibrils via 1000 rpm rotational shaking at 37°C for 7 days. Fibrils were diluted to a working concentration of 1 μM followed by sonication at 20% amplitude for 2mins before added to cell media. Endotoxin levels at 1× dilution, or in the conditioned media of seeded neurons, were assessed using the Pierce Chromogenic Endotoxin Quant Kit (Thermo Fisher, A39553).

Transmission electron microscopy

Transmission electron microscopy was used to characterise the morphology of αSyn fibrils. Fibril were deposited onto freshly glow-discharged, carbon-coated 300 mesh copper grids (TAAB Laboratories, C267/050) and incubated for 2 minutes, blotted with filter paper and stained with 2% uranyl acetate for 10 seconds, blotted gently, and air-dried. Imaging was performed using a JEOL 1400 TEM operating at 120 kV, equipped with a Gatan Rio CMOS camera. Fibril length quantification post sonication was carried out in ImageJ51.

Thioflavin T assay

Fibril generation was monitored using Thioflavin T assay as instructed by the manufacturer. Briefly, samples taken over a period of 1 to14 days of shaking were mixed with 25μM ThT in PBS followed by 1hour incubation in the dark at 37°C and subsequently analysed using a CLARIOstar Plus microplate reader with excitation at 450 nm and emission at 485 nm. Fluorescence intensity values were normalised against αSyn monomer to calculate the fold change in aggregation over time.

Seeding of cells with exogenous αSyn fibrils

Before experimental use, de novo generated fibrils were tested in a HEK293 cell line overexpressing human αSyn-Venus fusion protein via lentiviral transduction and G418 antibiotic selection. HEK293 cells were

cultured in DMEM/F-12 (Gibco, 11320033) supplemented with 10% FBS (Sigma, F7524), 1% GlutaMAX (Gibco, 35050061), and 1% Penicillin/Streptomycin (Gibco, 15140122). Fibrils were sonicated diluted to 1 μM in cell media and sonicated for 2 minutes (1s on/1s off, 20% amplitude) before adding to HEK-mVenus cells for 6 hours using Lipofectamine 2000 (Invitrogen, 17504044). Imaging was then performed using an EVOS FL fluorescent microscope (Invitrogen, AMF4300) to confirm the presence of fluorescent punctate, indicating αSyn aggregation. Lysates were than collected 24 hours post-transfection followed by immunoblotting. A similar protocol was adapted for adding fibrils to neuronal or microglial cultures, but without the use of lipofectamine in their corresponding culture media.

Bulk RNA sequencing

RNA samples from neuronal monocultures and neuron-microglia co-cultures were prepared using standard poly-A enrichment, 250–300 bp insert cDNA library was prepared with the NEB Next Ultra RNA Library Prep Kit (New England Biolabs, E7530) and sequenced on Illumina NovaSeq 6000 (S4) using 150 bp paired-end reads. Sequencing resulted in ~40 million reads per sample. Filtered substantia nigra single nuclei count data with cell type annotations for 7 post-mortem individuals was downloaded from the Broad Institute Single Cell Portal [https://singlecell.broadinstitute.org/single_cell]. The count matrices for all individuals were merged with 24 cell types encompassing all known resident cell classes as identified previously in the literature (*22*). For cell type deconvolution analysis, these cell types were merged into eight major subtypes: astrocytes, dopaminergic neurons, endothelial, excitatory and inhibitory neurons, microglia, oligodendrocytes and oligodendrocyte progenitor cells endothelial, excitatory and inhibitory neurons, microglia, oligodendrocytes and oligodendrocyte progenitor cells. Kallisto (v0.46.2) was used to estimate abundance for Ensembl (release 88) protein-coding genes from RNAseq reads. The cell-type composition of the bulk RNA-Seq samples was characterised using the MuSiC method (*23*).

To visualise the expression profiles of cell-type and stress-related genes across different experimental conditions, we generated heatmaps using normalised transcriptomic data. Transcript-level abundance estimates (TPM) were imported using the tximport R package (*67*). Gene-level TPM values were extracted by filtering for NSC-specific samples using consistent naming conventions. Metadata, including tissue type and

replicate information, was annotated using sample identifiers. Gene sets were compiled based on prior literature and publicly available datasets. These included markers associated with oxidative, ER, hypoxia, mitochondrial, and metabolic stress. TPM values were log2-transformed and z-scored (row-scaled) across each gene to emphasize relative expression differences while accounting for baseline variability. Genes with zero variance across all samples were excluded from visualization. Heatmaps were generated in R, with annotation metadata overlaid as sample labels. To maintain interpretability, only non-redundant gene symbols were retained, and duplicates were removed based on gene names.

Single cell RNA sequencing

Cell suspensions were enzymatically dissociated using Accutase to achieve a single-cell state. Following dissociation, cells were fixed in 100% methanol in accordance with the protocol recommended by 10x Genomics. Cells were loaded into the Chromium Controller (10x Genomics) for microfluidic partitioning and barcoding. Library preparation was performed using the Chromium Single Cell 3' Reagent Kit v3 (10x Genomics, PN-1000268), following the manufacturer's protocol. Sequencing was conducted on the Illumina NovaSeq 6000 platform. CellRanger count pipeline was used to process FASTQ files, generating feature-barcode matrices. Cells were identified using DropletUtils::emptyDrops (*68*). Those with high-ambient RNA contamination were identified and removed using decontX (*69*) and doublets were filtered out using scDblFinder (*70*). Low-ambient singlets were further processed and analysed primarily using Seurat V5 (*71*), with additional packages used as specified. Biological replicates were integrated using Seurat::CCAIntegration.

<u>Transcriptomic profiling of Neurons in monoculture and co-culture</u>

To investigate whether clearance of aggregated proteins is associated with neuronal rescue, we performed single-cell RNA sequencing (scRNA-seq) on dopaminergic neurons (DANs) seeded with fibrils alone (monoculture) and fibril-seeded DANs co-cultured with microglia (MG). Processed Seurat objects corresponding to different experimental groups were merged and annotated to distinguish monoculture and co-culture conditions. After merging, highly variable genes were identified using Seurat::FindVariableFeatures with the 'vst' method (n = 2000). The data were scaled, and principal component

analysis (PCA) was performed. Clustering was carried out using Seurat::FindNeighbors and FindClusters with a resolution of 0.1, followed by dimensionality reduction with UMAP (dims = 1:30).

Nine transcriptionally distinct clusters were identified. Clusters 0, 1, 2, 4, 6, and 7 were annotated as neurons based on the expression of canonical neuronal and dopaminergic markers. Cluster 3 was annotated as microglia. We then focused on neuronal clusters to examine expression signatures associated with various cellular stress responses. Expression levels for these gene sets were visualised using Seurat::DotPlot. Values were log-normalised and z-score transformed across genes. Dot plots were generated to show expression intensity and the proportion of cells expressing each gene. Differential gene expression analysis was performed using Seurat::FindAllMarkers with the Wilcoxon rank-sum test (test.use = "wilcox") and parameters set to logfc.threshold = 0.25 and min.pct = 0.1. Gene Ontology (GO) and pathway enrichment analyses were conducted using ShinyGO (v0.77) (*72*). Only differentially expressed genes between monoculture and co-culture groups were included. GO terms with FDR-adjusted P values < 0.05 were considered significant.

Trajectory Inference and Functional Annotation of Microglia

Cells were annotated by mapping to reference dataset from Welch et al. (*26*) using SingleR (*73*) and Seurat::TransferData as a complementary method. Only microglia cells (N=5640) confidently annotated by both methods were used for further analysis. Microglia cells were re-integrated using Seurat::RPCAIntegration, followed by clustering using the Leiden algorithm (resolution 0.4) (*74*). To identify top differentially expressed genes for each cluster, pairwise testing with MAST was performed (*75*) adapting code from Tuddenham et al. (*76*) to summarise the results from all pairwise comparisons. Significance of differences in cluster proportions between non-seeded and fibril seeded conditions was determined using scProportionTest (*77*). Module scores for DAM genes were calculated using Seurat::AddModuleScore. Similarity of clusters to the microglia states defined by Dolan et al. (*13*) were determined using ClusterFoldSimilarity (*78*), which determines similarity by comparing fold changes of shared genes across clusters.

Trajectory was inferred using Slingshot (*79*) and generalized additive models were fitted using tradeSeq (*80*). Microglia cluster 2, with the highest proportion in non-seeded condition and the lowest DAM score among

the four largest microglia clusters, was specified as the starting cluster for the trajectory inference. To characterise each trajectory, Gene Ontology (GO): Cellular Component enrichment analysis was performed using the PANTHER Overrepresentation Test (Release 20240807) with the database (DOI: 10.5281/zenodo.15066566, released 2025-03-16), based on differentially expressed genes between the start and end clusters of each trajectory.

Homogenous time resolved fluorescence (HTRF)

αSyn aggregation was measured using an anti-phospho Ser129 αSyn HTRF kit (Revvity, 6FSYNPEG) following the manufacturer's instructions. 4 µl of donor and acceptor Förster Resonance Energy Transfer (FRET) fluorophores were mixed with 16 µl of cell lysate in a 96-well plate, sealed with a film and incubated for 2 hours in the dark. Fluorescence intensity was recorded using a CLARIOstar Plus Microplate Reader (BMG Labtech, Ortenberg, Germany) with excitation at 340 nm and emission readings at 620 nm and 665 nm. Time-resolved FRET was determined by calculating the emission ratio (665/620) followed by background subtraction, BCA normalisation, and fold increase over non-seeded control.

Immunoblotting

Cells were lysed in RIPA [50 mM Tris-HCl, pH 7.4 (Santa Cruz Biotechnology, sc-301950), 500 mM NaCl (Sigma, S9888), 0.1% SDS (Sigma, L3771), 5 mM EDTA (Invitrogen, 15575020), 1 mM DTT (Roche, 10708984001) and 1x protease inhibitor tablet (Roche, 11697498001) in dH_2O], followed by 10-minute centrifugation at 10,000g to remove cell debris. The lysate was then further spun down at 100,000g for 2 hours. The supernatant was collected as the RIPA soluble fraction and the pellet was resuspended in the same RIPA buffer with 2% SDS, sonicated for 2 minutes (1s on/1s off, 20% amplitude) and kept as the insoluble fraction for determining the level of pSyn.

Protein concentration was quantified by BCA following manufacturer's instructions and the lysates were then mixed with NuPAGE LDS Sample Buffer (Invitrogen, NP0007) and Sample Reducing Agent (Invitrogen, NP0009) and heated at 95°C for 5 minutes. Samples were resolved by 4–12% Bis-tris gels and transferred to a nitrocellulose membrane. Membranes were blocked for 1 hour in 5% bovine serum albumin (Melford, A30075) in 1X TBS with 0.1% Tween-20 (Sigma, P1379). Membranes were incubated overnight

at 4°C with primary antibodies, followed by a 1hour incubation at room temperature with HRP-conjugated secondary antibodies. Membranes were then incubated with ECL Start Western Blotting Detection Reagent (Cytiva, GERPN3244) for 1–5 minutes and imaged using a ChemiDoc Imaging System (Bio-Rad). Band intensities were quantified by densitometry using Image Lab software (Bio-Rad, v6.1). All antibodies and their dilutions are listed in **Table S7**.

Microscopy

Immunocytochemistry: Cells were fixed in 4% paraformaldehyde (PFA), permeabilised with 0.1% Triton-X-100, and blocked in 10% BSA in PBST (0.1% Tween-20) for 1 hour at RT. This was followed by overnight incubation with primary antibodies at 4°C and washed in DPBS three times for 15 minutes at RT the following day. Cells were then stained with fluorescently labelled secondary antibodies for 1 hour at RT, washed in DPBS three times for 5 minutes. For detection of cathepsin B activity, cells were incubated with Magic Red (Abcam, ab270772; 1:25 dilution of the prepared stock) for 30 minutes, followed by washing in DPBS two times, prior to imaging. Finally, samples were mounted in ProLong Glass Antifade Mountant with DAPI (Invitrogen, P36981) or VECTASHIELD Antifade Mounting Medium (Vector Laboratories, H-1000-10) and sealed with CoverGrip Coverslip Sealant (Biotium, 23005).

Immunohistochemistry for human brain sections: Antigen retrieval was performed by steaming slides in 10 mM sodium citrate buffer (pH 6.0, 0.05% Tween-20) for 30 minutes, followed by cooling at room temperature for 1 hour in retrieval buffer. Slides were then blocked with 5% BSA at room temperature. Primary antibodies [anti-GPNMB (1:200), antiIBA1 (1:200), anti-pSyn (1:500)] were applied and incubated overnight at 4°C. Slides were washed 3× in TBST, followed by incubation with secondary antibodies for 1 hour 30 minutes at room temperature. After washing 3× in TBST, autofluorescence was quenched using Autofluorescence Quenching Reagent for 10 minutes (ThermoFisher, R37630), followed by washes 2× in TBST and 1× in TBS. Samples were then mounted with ProLong Glass Antifade Mountant (Invitrogen, P36980).

Super-resolution microscopy: Imaging was performed using a Zeiss LSM980 laser scanning confocal microscope, integrated with an Airyscan 2 module, featuring an Olympus Plan-Apochromat 63x 1.43 NA oil-

immersion lens and a 32-channel gallium arsenide phosphide (GaAsP-PMT) area detector. Z-stack images were generated, with stack intervals at 0.13 μm, operated by a Wienecke & Sinske PiezoDrive CAN stage controller, post-processed by Zen Blue (V3 3.89). All Images are quantified in Fiji (ImageJ 3.5). For Super-resolved structured illumination microscopy (iSIM), VisiTech iSIM super-resolution module integrated with an Olympus IX83 inverted microscope, equipped with a high-resolution 100× UPlanApo TIRF oil immersion objective (NA 1.50). Detection was carried out using a Hamamatsu ORCA-Quest qCMOS camera. To enhance image contrast and spatial resolution while minimizing artefact introduction, raw image data were processed in cellSens Dimension software (Olympus, v4.2.1).

Proximity Ligation Assay

Proximity ligation assays (PLA) were performed using 13 mm 1.5H high-precision glass coverslips (Marienfeld, Cat. No. 0117530). All PLA procedures used the Duolink In Situ Red Starter Kit for Mouse/Rabbit (Sigma, DUO92101), following the manufacturer's instructions. In summary, cells were initially fixed with 4% PFA in DPBS for 15 minutes, then permeabilized for 30 minutes at room temperature using DPBS supplemented with 0.1% Triton X-100. After permeabilization, neurons were incubated with Duolink Blocking Solution at 37°C for one hour. Primary antibodies were diluted in Duolink Antibody Diluent and applied overnight at 4°C. The following day, two washes were performed using 1X Wash Buffer A, each for 10 minutes. PLA probes (PLUS and MINUS) were prepared at a 1:5 dilution in Antibody Diluent along with corresponding secondary antibodies. Co-cultures were incubated with this solution, followed by another two 10-minute washes in 1X Wash Buffer A. Subsequently, ligation was carried out by incubating in the Ligation Buffer containing ligase for 30 minutes at 37°C. After ligation, two further washes with Wash Buffer A were conducted before amplification using 1X Amplification Buffer for 100 minutes. Post-amplification, cells were washed twice in Wash Buffer B for 10 minutes each and finally rinsed in 0.01X Wash Buffer B for 1 minute.

Image quantification and 3D reconstruction

iPSC-Derived Cultures

Images were acquired using a Zeiss LSM 880 microscope or iSIM at specified magnifications (20×–63×, ≥3–10 fields/differentiation/cell line). All image analyses were performed in ImageJ/FIJI using consistent pipelines. To assess microglial morphology, masked microglia were analysed for circularity ($4\pi\times\text{area}/\text{perimeter}^2$), aspect ratio (major/minor axis), and roundness ($4\times\text{area}/(\pi\times\text{major axis}^2)$) (, n≥5 fields/differentiation/cell line). To assess neuron–microglia interactions, neuronal and microglial markers were masked and thresholded using Fiji algorithms, and their interactions per stack were quantified using Mander's coefficient (n ≥ 5 cells /differentiation/cell line).To quantify pSyn or Synapsin I level, thresholding were applied, followed by "Analyse Particles" for particle number, % area, size; normalized to $MAP2^+$ neurons (n≥3 fields/differentiation/cell line).To measure $pSyn^+$ or $MAP2^+$ signal in microglia, $MAP2^+$ $pSyn^+$ areas were quantified as above in CD68+ ROIs. (n≥10 cells/differentiation/cell line).

For stained human postmortem tissue images, confocal z-stacks were subjected to background subtraction, automatic thresholding using Fiji algorithms, and JACoP plugin analysis to determine percentage voxel overlap. All three-dimensional reconstructions were performed in Imaris (version 10.0.0).

Relative gene expression

RNA extraction was carried out using the RNeasy Kit (Qiagen, 74104) following the guidelines provided by the manufacturer. A total of 1 µg of cDNA was generated using random hexamers provided in the QuantiTect Reverse Transcription Kit (Qiagen, 205311). Quantification of mRNA levels was done using real-time PCR, which involved a mixture containing 5 ng of cDNA, LightCycler 480 SYBR Green I Master Mix (Roche Life Science, 04707516001) and 1 µM of each primer, both forward and reverse. Normalisation of the data were done using the housekeeping gene GAPDH. The sequences of all primers used are shown in **Table S8**. Analysis of the samples was conducted using the LightCycler 480 Instrument (Roche Life Science). The instrument's software was utilised for the determination of crossing threshold (Ct) values. The relative expression of genes was then calculated using the ΔΔCt method.

MSD electrochemiluminescence

The R-plex human neurofilament L kit was used as per manufacturer's instruction (Meso Scale Discovery, F217X-3), using 25 µl of sample (diluted cell lysate at 1:50) or standard. Briefly, samples and standards were prepared and added to pre-coated assay plates for 1 hour at RT, followed by the addition of electrochemiluminescent-labelled detection antibodies. After 1 hour of incubation and washing to remove unbound substances, the assay was read using MESO QuickPlex SQ 120MM (Meso Scale Diagnostics, USA).

ELISA

α-Syn, TNFα, IL-10, and GPNMB levels in lysates and conditioned media from mono- and co-cultures were quantified using corresponding ELISA kits (BioLegend 448607, KHC3011, Life Technologies, BioLegend 430604, and Bio-Techne DY2550, respectively) following the manufacturers' protocols. For all assays, 96-well plates were coated with a capture antibody and incubated overnight at 4°C. The next day, 100 µl of either samples or standards were added to the wells and incubated for 2 hours. Following this, a detection antibody was applied and incubated for another 2 hours. After each step, the plates were washed three times with wash buffer. Subsequently, 100 µl of Avidin-HRP was added and incubated for 30 minutes, followed by the addition of TMB substrate solution for another 30 minutes. The reaction was terminated with 50 µl of stop solution. Absorbance was measured at 450 nm using a CLARIOstar Plus microplate reader (BMG Labtech, Germany). The following dilutions were used for α-Syn: 1/1000 for lysates from dopaminergic neuron and 1/100 for lysates from co-culture; for TNFα: 1/2 for conditioned media; for IL-10: 1/10 for monoculture-conditioned media and 1/1 for co-culture-conditioned media. For GPNMB, the dilutions were: 1/250 for dopaminergic neuron lysates, 1/1000 for co-culture lysates, 1/10 for dopaminergic neuron-conditioned media, and 1:1000 for co-culture-conditioned media.

Human cytokine array

Cytokines in conditioned media from co-cultured microglia and dopaminergic neurons were detected using the Proteome Profiler Human XL Cytokine Array Kit (R&D Systems, # ARY022B). Dopaminergic neurons were plated at 800,000 cells/well in 12-well plates, with microglia added at a 1:1 ratio; conditioned media were collected 2 weeks later, clarified by centrifugation at 1200 × g for 10 min at 4°C, and processed as per

the manufacturer's protocol. For biological replicates, media from three independent iPSC differentiations were pooled per condition onto duplicate-spotted nitrocellulose membranes, which were blocked, incubated overnight with samples at 4°C, then sequentially with detection antibody cocktail, streptavidin-HRP, and chemiluminescent reagents. Spot intensities were quantified using the ChemiDoc MP Imaging System (Bio-Rad).

Treatments with Antibodies, Inhibitors, LPS, and Annexin V

Antibodies targeting human IL-10 receptor-alpha (0.1 μM and 1 μM), CD22 (1 μM) or SPP1 (5 μg/ml) and the non-targeted controls (corresponding concentrations) or inhibitors targeting MCP-1 (#RS504393, 2 μM), MMP9 (#444278, 5 μM) or P2RY12 (PSB-0739, 2 μM and 4 μM) were added every 3 days to microglia monocultures or neuron-microglia co-cultures. A similar protocol was followed for the TREM2 antagonist and its corresponding IgG control, applied at a concentration of 10 μg/ml. Annexin V was added to neurons at a concentration of 0.2 μg/ml prior to co-culturing with microglia and subsequently re-applied every three days at 0.2 μg/ml until the end of the co-culture period. LPS was added two days after plating the microglia at a final concentration of 200 ng/ml and subsequently re-applied every three days until the end of the co-culture period.

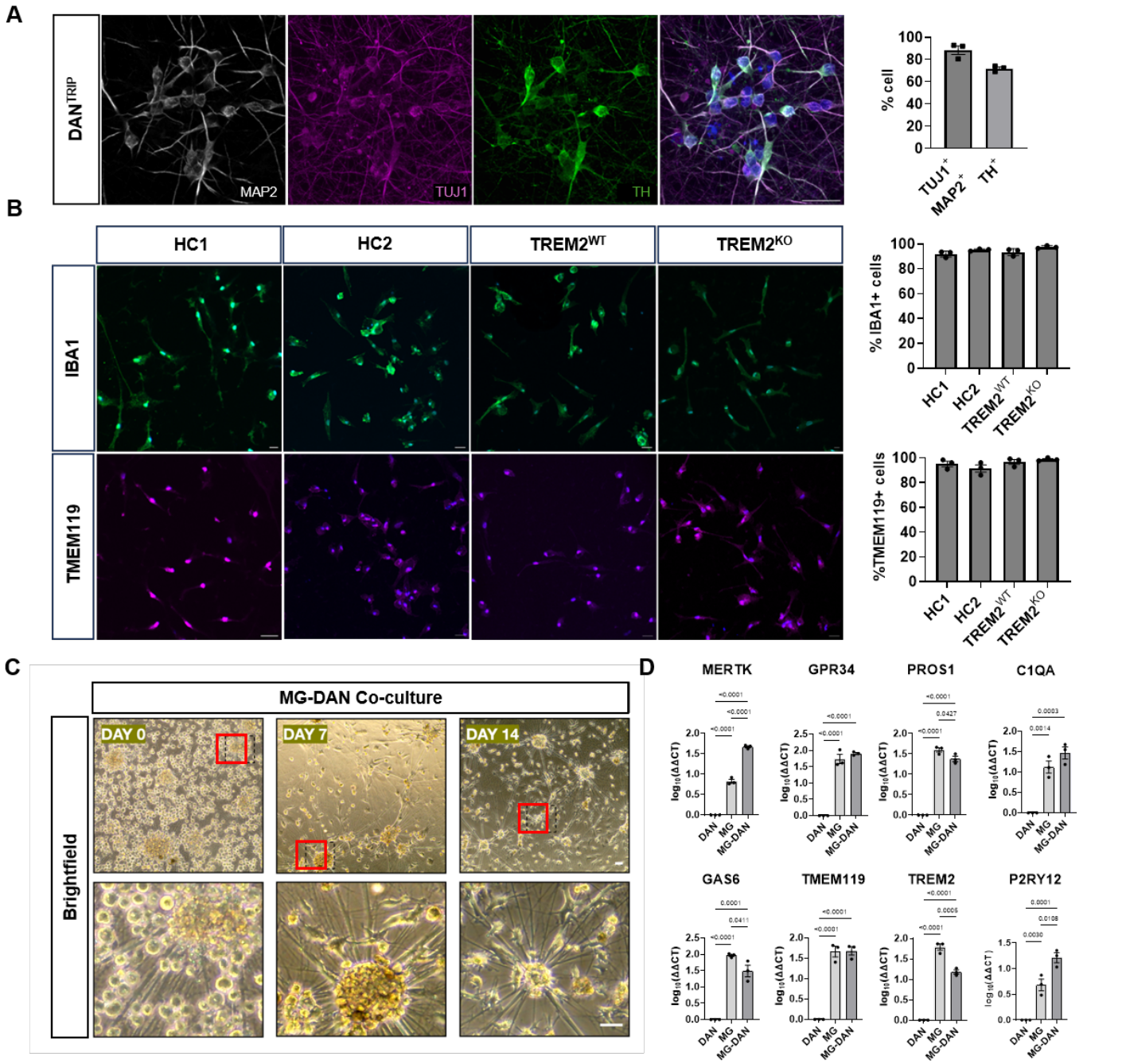

Fig. S1 Characterisation of iPSC-derived dopaminergic neurons and microglia in monoculture and co-culture.
(A) Representative confocal images and quantification of iPSC-derived dopaminergic neurons (DANs) from the DAN^{TRIP1} line, stained for TH, MAP2, and TUJ1 (n=3 independent differentiations for DAN^{TRIP1}).
(B) Representative confocal images and quantification of iPSC-derived microglia (MG) stained with IBA1 and TMEM119 from healthy controls (HC1, HC2), isogenic control (ISO), and TREM2 knockout (TREM2 KO) lines (n=3 differentiations per iPSC line).
(C) Brightfield images showing time-dependent morphological maturation of MG^{pre} in MG–DAN co-culture. Initially, pMacpre displayed a uniform round shape. After 7 days, cells adopted a ramified MG morphology among DANs under baseline conditions. The representative image of D14 MG-DAN co-culture is also shown in **Fig 1A**.
(D) qPCR quantification of MG gene expression in DAN^{TRIP} monocultures, MG monoculture, and MG-DAN^{TRIP} co-cultures (n=3 independent differentiations for DAN^{TRIP1}, MG^{HC1}, MG^{HC1}-DAN^{TRIP1}).

Data are presented as mean ± SD. Statistical analysis by one-way ANOVA **(D)** with Tukey's post hoc test. *Scale bar*: 20 µm.

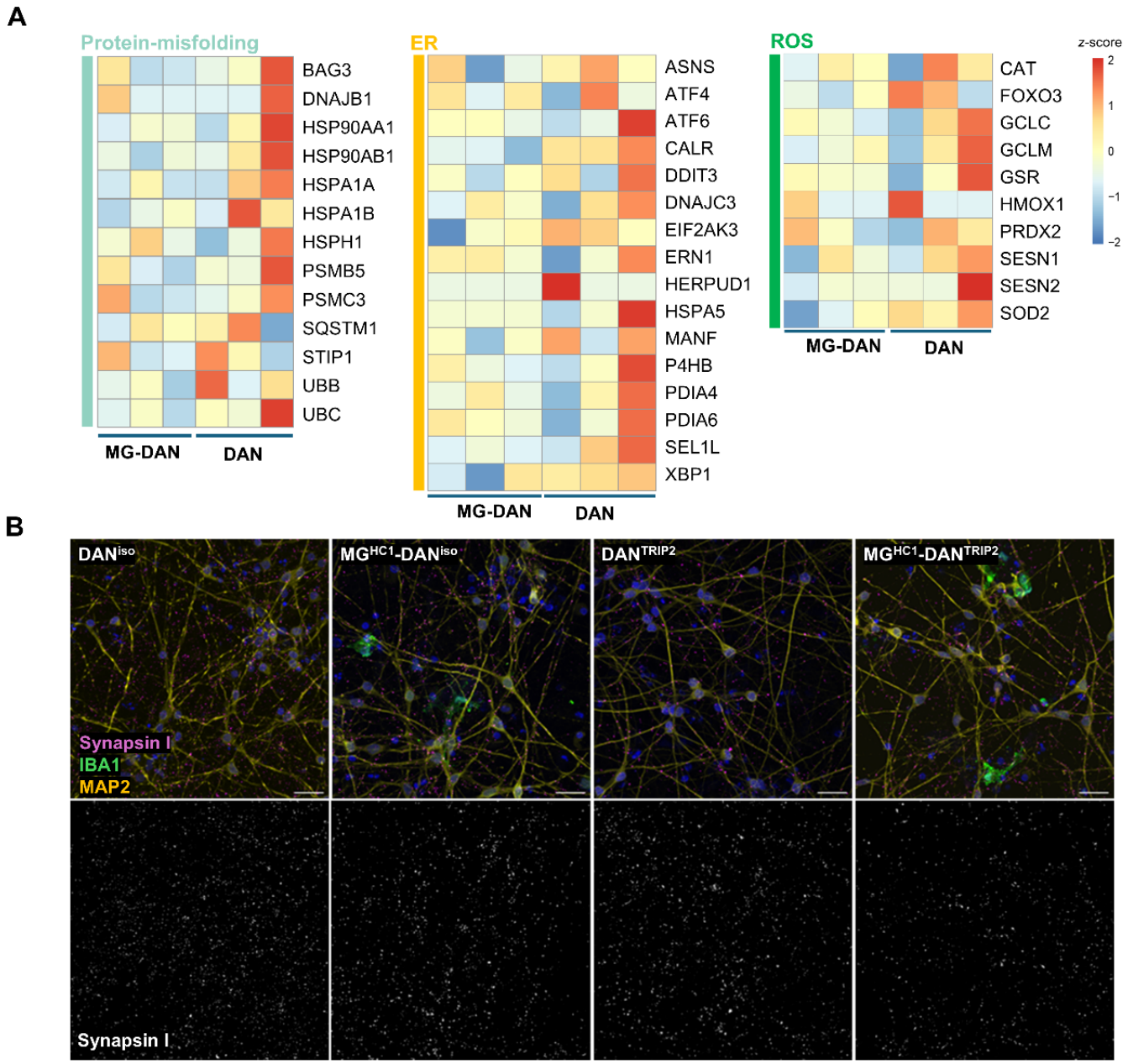

Fig. S2 Characterisation of iPSC-derived dopaminergic neurons and microglia in co-culture.

(A) Bulk RNA-seq heatmaps showing stress gene expression profile involving protein-misfolding, endoplasmic reticulum (ER), and inflammation in DAN^{TRIP} monocultures which is reduced in MG-DAN^{TRIP} co-cultures.

(B) Representative confocal images of Synapsin I^{+} pre-synaptic terminals in DAN^{TRIP2} or DAN^{ISO} monocultures and when co-cultured with IBA1^{+} microglia (MG). Note reduced Synapsin I^{+} puncta in DAN^{TRIP2} neurons in co-culture with MG. The representative image of MG^{HC1}-DAN^{TRIP2} was used for 3D reconstruction and is also shown in **Fig.1J.** Quantification is shown in **Fig. 1I.** *Scale bar*, 20 µm.

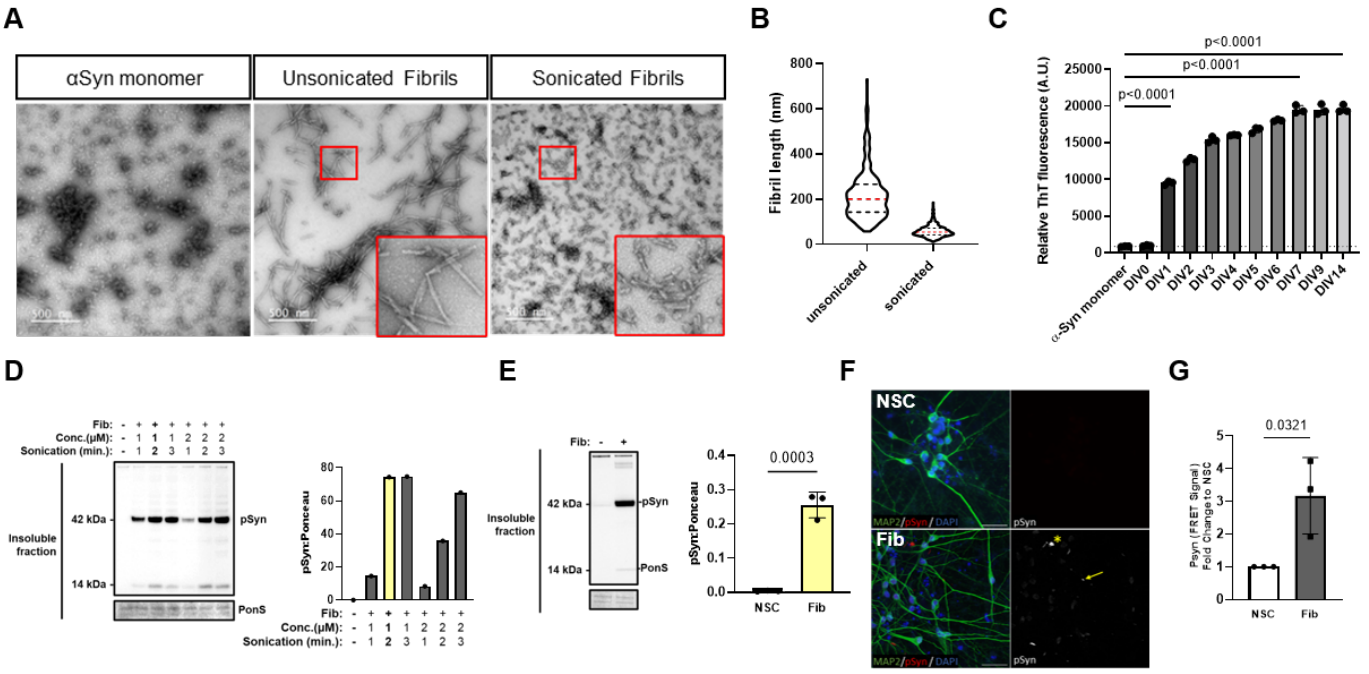

Fig. S3 *De novo* generated α-synuclein fibrils seed aggregation in HEK293 cells and iPSC-derived dopaminergic neurons.

(A) Electron micrographs depict α-synuclein (αSyn) monomers or αSyn fibrils after 7 days of shaking, and fragmented fibrils after sonication.

(B) Median Fibril length decreased from 200 nm to 55 nm after 2 min of sonication.

(C) Quantification of Thioflavin T(ThT) fluorescence showed that fibrils (Fib) unlike monomeric protein exhibit increased signal indicating assembly into β-sheet-rich structures (n=3 independent experiments).

(D) Immunoblotting and quantification for pSyn in the RIPA-insoluble fraction of HEK293 stably expressing α-Syn-venus after seeding overnight showing optimisation of fibril dose at different fibril sonication times.

(E) Immunoblotting and quantification of pSyn-venus confirmed the reproducibility of seeding with fibrils (1µM) at the optimal (2 minutes) sonication (n=3 independent experiments).

(F) Representative confocal images of DAN^{TRIP} treated with sonicated fibrils (Fib) for 2 weeks at 1µM stained positive for pSyn aggregates in processes (arrowheads) and cell bodies (asterisk), which are absent in the non-seeded condition (NSC). *Scale bar*, 20 µm.

(G) Time-resolved FRET assay using DAN lysates revealed increased pSyn levels 2 weeks post seeding with Fib compared to NSC (n=3 independent differentiations for DAN^{TRIP1}).

Data are presented as mean ± SD. Statistical analysis by one-way ANOVA **(C)** with Tukey's post hoc test, two-tailed t-test **(E)**, or one sample t-test **(G)**.

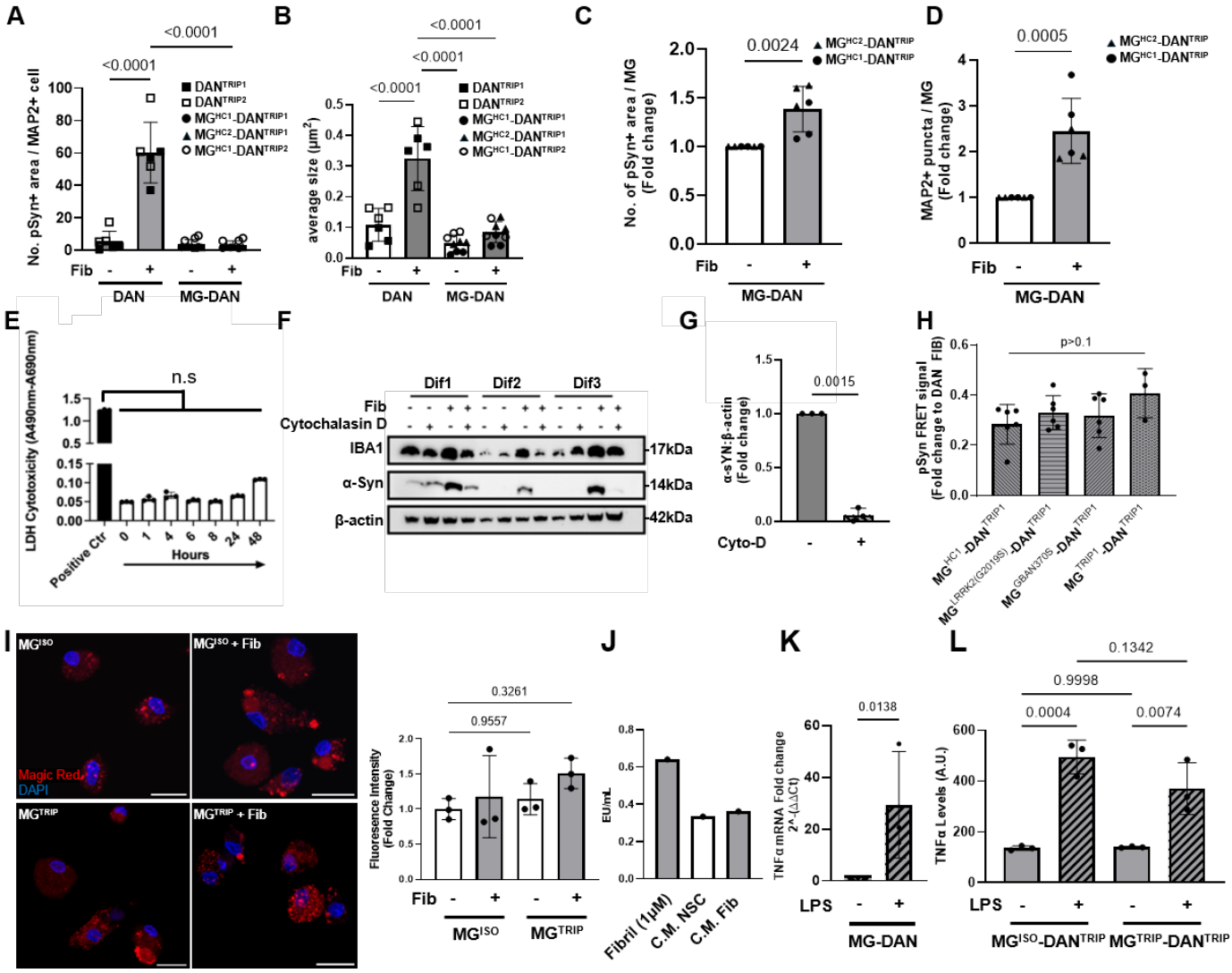

Fig. S4 Microglia remove large intraneuronal α-synuclein aggregates.

(A) Quantification of the total pSyn^{+} area count normalised to the number of MAP2^{+} neurons showing reduced pSyn aggregates in MG-DAN co-cultures compared to DAN monocultures under Fibril-seeded conditions (n = 3 independent differentiations for DAN^{TRIP1}, DAN^{TRIP2}, MG^{HC1}-DAN^{TRIP1}, MG^{HC2}-DAN^{TRIP1} and MG^{HC1}-DAN^{TRIP2}).

(B) Quantification of the total pSyn^{+} area size normalised to number MAP2^{+} neurons showing reduced pSyn aggregates in MG-DAN co-cultures compared to DAN monocultures under fibril-seeded conditions (n = 3 independent differentiations for DAN^{TRIP1}, DAN^{TRIP2}, MG^{HC1}-DAN^{TRIP1}, MG^{HC2}-DAN^{TRIP1} and MG^{HC1}-DAN^{TRIP2}).

(C) Quantification of pSyn^{+} area count within CD68^{+} MG (n = 3 independent differentiations for MG^{HC1}-DAN^{TRIP1} and MG^{HC2}-DAN^{TRIP1}).

(D) Quantification of MAP2^{+} area count within CD68^{+} MG (n = 3 independent differentiations for MG^{HC1}-DAN^{TRIP1} and MG^{HC2}-DAN^{TRIP1}).

(E) Time-course examination of 10 µM cytochalasin D revealed MG toxicity at 48 h but not at earlier time-points using LDH (Lactate Dehydrogenase) (n=3 independent differentiations for MG^{HC1}).

(F) αSyn fibril (1 µM) uptake by MG is blocked in cells treated with cytochalasin D (10 µM 1h prior to fibril addition and for 24h thereafter), compared to the fibril condition alone, shown using immunoblotting.

(G) Quantification of fibril uptake following inhibition of phagocytosis using cytochalasin D (n=3 independent differentiations for MG^{HC1}).

(H) HC, *GBA^{N409S}*, *LRRK2^{G2019S}*, or *SNCA^{TRIP}* mutant MG clear pSyn^{+} neuronal aggregates similarly when co-cultured with DAN under fibril-seeded conditions, measured using time-resolved FRET assay (n≥3 independent differentiations per MG iPSC line).

(I) Representative images and quantification of Cathepsin B activity using the Magic Red assay showing no change in fluorescent intensity between MG^{ISO} and MG^{TRIP} monocultures at baseline and when treated with fibrils (n=3 independent differentiations for MG^{ISO} and MG^{TRIP2}). *Scale bar*, 20 µm.

(J) Endotoxin levels in the conditioned media of fibril-seeded DAN monocultures before the addition of MG is less than 0.5 EU/ml and comparable to NSC DANs.

(K) qPCR analysis of TNFα mRNA in LPS-treated co-cultures vs baseline showing LPS-induced TNFα up-regulation (n=3 independent differentiations for MG^{ISO}-MG^{TRIP2}).

(L) TNFα levels do not differ between MG^{ISO} and MG^{TRIP} co-cultured with DAN^{TRIP} under basal or LPS-treated conditions (n=3 independnet differentiations for MG^{ISO}-DAN^{TRIP2} and MG^{TRIP2}-DAN^{TRIP2}).

Data are presented as mean ± SD. Statistical analysis by one-way ANOVA **(A, B, E, H, I, L)** with Tukey's post hoc test or one sample t-test **(C, D, G, K)**.

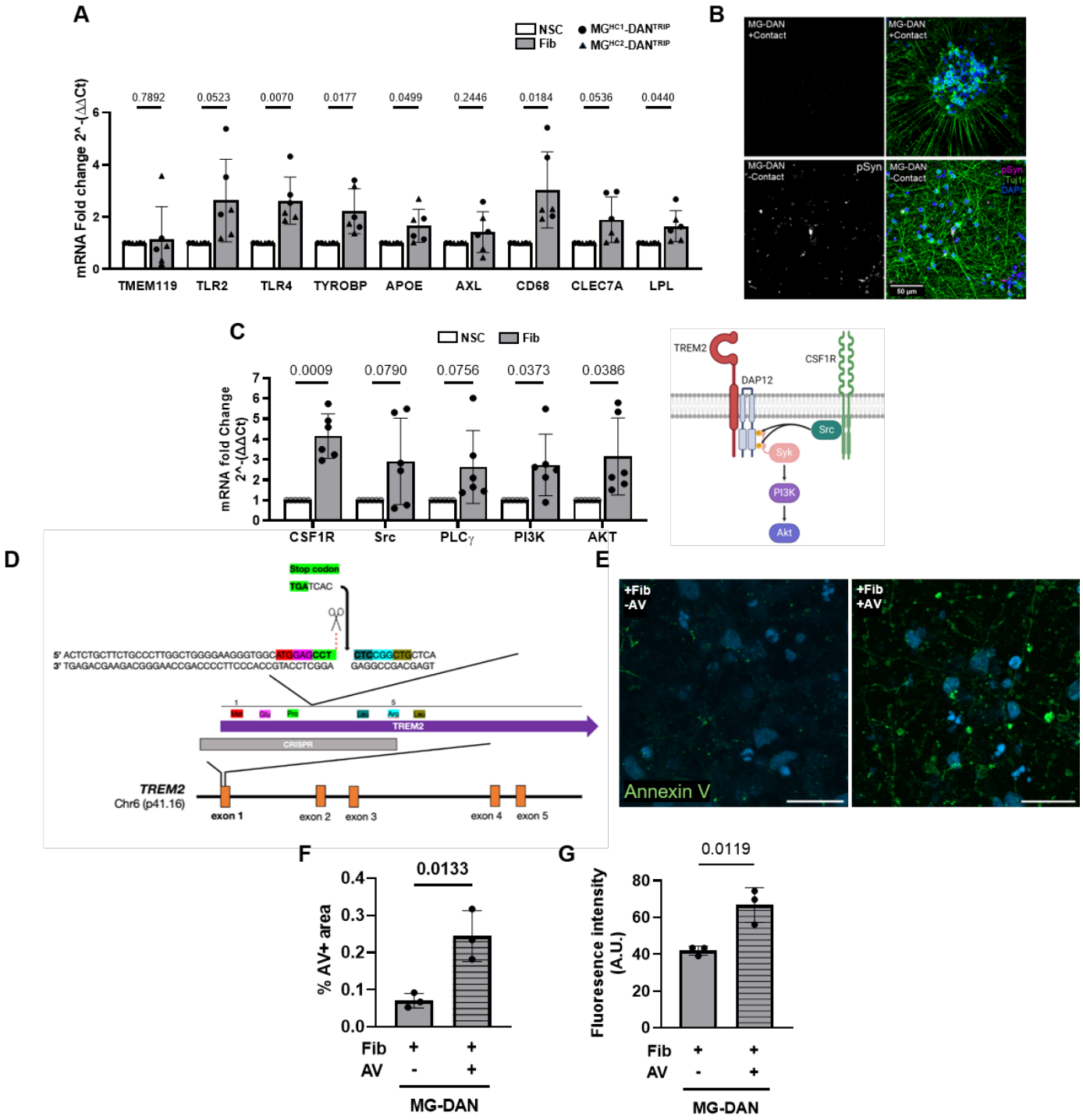

Fig. S5 Clearance of α-synuclein aggregates is TREM2-independent

(A) qPCR analysis of relevant markers (*TMEM119, TLR2, TLR4, TYROBP, APOE, AXL, CD68, CLEC7A, LPL*) normalised to GAPDH and plotted relative to the NSC condition showing up-regulation of DAM and no change in the homeostatic gene *TMEM119* (n=3 independent differentiations for MG^{HC1}-DAN^{TRIP1} and MG^{HC2}-DAN^{TRIP1}).

(B) Representative confocal images of pSyn staining in DAN^{TRIP} when MG^{HC1} were co-cultured with or without contact using a transwell under fibril-seeded conditions.

(C) qPCR analysis showing upregulation of genes involved in TREM2 signalling (*CSF1R*, *Src*, *PLCγ*, *PI3K*, and *AKT*) in the fibril-seeded condition compared to NSC in MG-DAN co-cultures (n=6 independent differentiations for MG^{HC1}-DAN^{TRIP1}).

(D) CRISPR/Cas9-mediated knockout of human TREM2. The 5' end of exon 1 was targeted using CRISPR/Cas9, introducing a TGA stop codon and four additional bases via homology-directed repair (HDR), resulting in a homozygous TREM2 knockout (BIONi010-C).

(E) Representative confocal images of Annexin V (AV) staining to confirm binding to and thus blocking of phosphatidylserine.

(F) Quantification of % AV^+ area normalised to number of nuclei (n=3 independent differentiations for MG^{HC1}-DAN^{TRIP1}). *Scale bar*, 20 µm

(G) Quantification of AV fluorescence intensity normalised to number of nuclei (n=3 independent differentiations for MG^{HC1}-DAN^{TRIP1}).

Data are presented as mean ± SD. Statistical analysis by one sample t-test **(A, C)** or two-tailed t-test **(F, G)**. *Scale bar*, 20 µm, unless else specified.

A

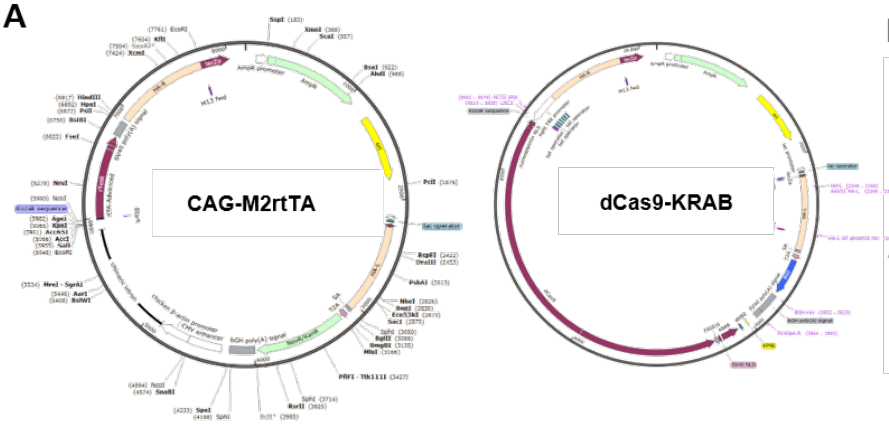

B

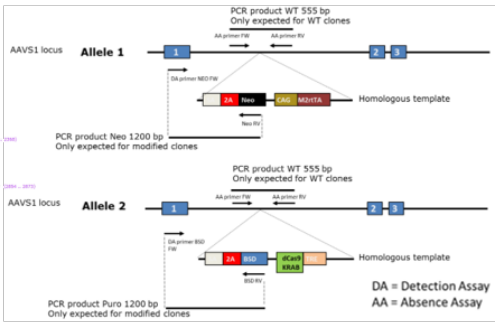

C

CRISPR	Sequence
CR2 AAVS1_rv	TGTCCCTAGTGGCCCCACTGTGG

Primer	Sequence	Product size
DA primer BSD_fw	CTCCGACGGATGTCTCCCTTGCG	1200
DA primer BSD_rv	CACGCTGTAATCCTCGCTGA	
DA primer NEO_fw	CCAGAGGCGGCGCAGAAGCCAG	1200
DA primer NEO_rv	ATCTTGTTCAATGGCCGATCCCAT	
AA primer_fw	GTCACCAGATAAGGATCTGCC	555
AA primer_rv	CTCCGACGGATGTCTCCCTTGCG	

D

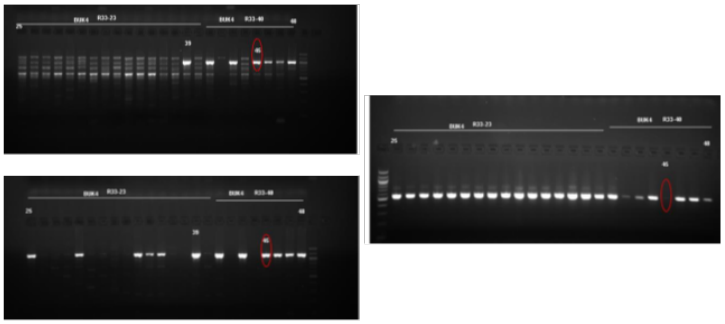

E

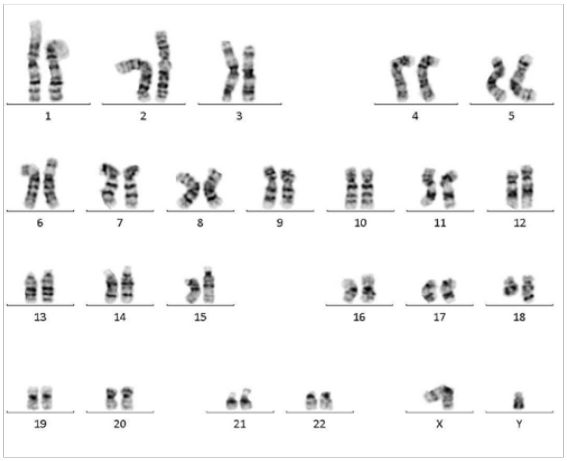

F

	HC1		dCas9-HC1	
Marker	Allele 1	Allele 2	Allele 1	Allele 2
AMEL	X	Y	X	Y
CSF1PO	10	12	10	12
D13S317	8		8	
D16S539	10	13	10	13
D18S51	15	16	15	16
D19S433	16		16	
D21S11	30	31,2	30	31,2
D2S1338	23	24	23	24
D3S1358	15	17	15	17
D5S818	11		11	
D7S820	8	11	8	11
D8S1179	11	15	11	15
FGA	20	21	20	21
TH01	9	9,3	9	9,3
TPOX	8		8	
vWA	15	18	15	18

G

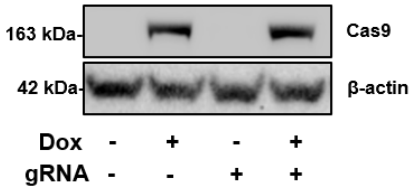

H

Gene	gRNA ID	TSS Site	Protospacer Sequence
P2RY12	P2RY12.1	P1P2	GTGTCCAGGGTCAGATTACA
P2RY12	P2RY12.2	P1P2	GGTGATCACAATCAGAAGAC
P2RY12	P2RY12.3	P1P2	GCTGAAATGACAAAAATCCA

I

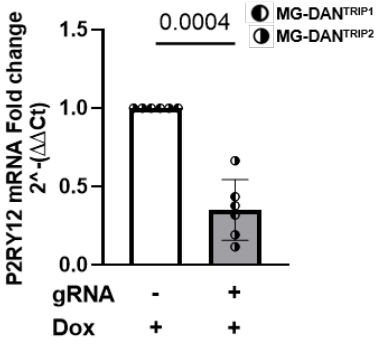

Fig S6. Generation of doxycycline inducible dCas9-KRAB gene in hiPSCs

(A) Plasmid maps of the reverse tetracycline-controlled transactivator (rtTA) and dCas9 sequences used to generate dead Cas9-KRAB hiPSCs using clone OX3-9 (HC1). iPSCs were nucleofected with the CRISPR "CR2_AAVS1_RV" and 2 μg of each plasmid.

(B) Schematic showing the integration sites of the rtTA and dCas9 sequences at the AAVS1 loci. 1, 2 and 3 represent the respective exon numbers in the AAVS1 locus. SA: splice acceptor, 2A: self-splicing protein, CAG: constitutively active promoter, TRE: tetracycline transactivator responsive element. Screening primers are shown as arrows.

(C) Table showing the primer sequences used to generate and confirm the doxycycline inducible dCas9 system in hiPSCs.

(D) PCR gels confirming insertion of the M2rtTA and the dCas9-KRAB expression cassettes into the AAVS1 locus of HC1 hiPSCs resulting in a doxycycline inducible dCas9 system.

(E) Karyotyping of the newly generated dCas9-KRAB HC1 hiPSCs.

(F) Short tandem repeat (STR) analysis of the dCas9-KRAB HC1 hiPSC clone and its corresponding line of origin. The number of allelic repeats tested in each locus matched between both lines, confirming that HC1/dCas9 clone was derived from the parent HC1 hiPSC line.

(G) Immunoblotting with anti-Cas9 antibody in iPSC lysates showing robust dCas9 induction upon doxycycline (Dox) treatment, without any expression observed in non-Dox treated controls.

(H) gRNA sequences obtained from the hCRISPRi-v2.1 Weissman Laboratory Library. The targeted promoter region at the transcription start site (TSS) is indicated.

(I) Quantification of P2RY12 mRNA level by qPCR confirmed P2RY12 knockdown in MG-DAN co-cultures compared to control MG (n = 3 independent differentiations for MG^{dCas9}-DAN^{TRIP1} and MG^{dCas9}-DAN^{TRIP2}).

Data are presented as mean ± SD. Statistical analysis by one sample t-test **(I)**.

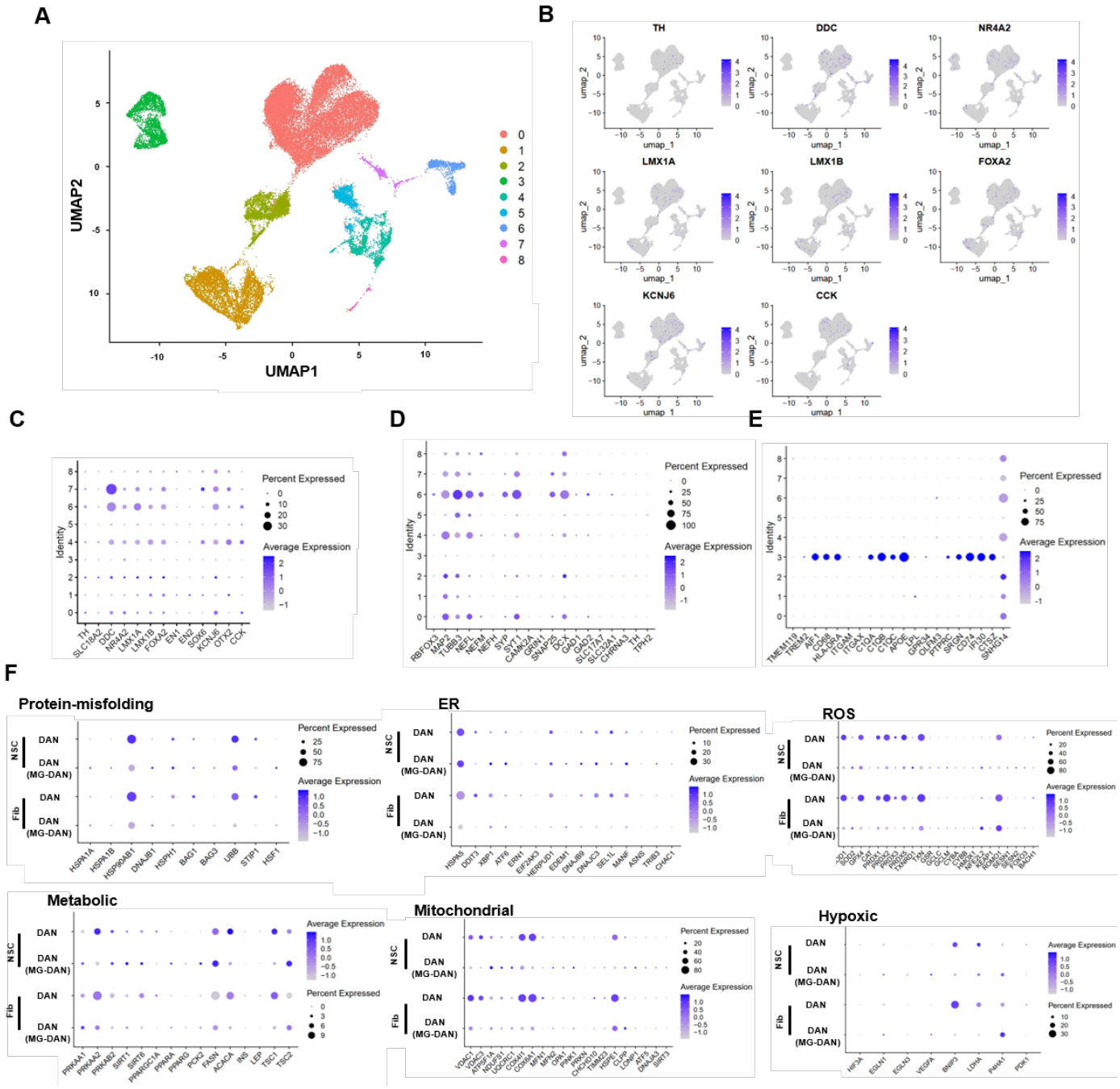

Fig S7 Single cell RNA Sequencing analysis for DANs

(A) UMAP of single-cell transcriptomes from MG–DAN co-cultures reveal neuronal (clusters 0, 4, 6, 7) and microglial (cluster 3) identities.

(B) Expression of DAN markers across cell clusters visualised by UMAP projection.

(C) Dot plot showing expression of DAN markers across clusters.

(D) Dot plot showing expression of neuronal markers in each cluster.

(E) Dot plot showing expression of MG markers across clusters.

(F) Dot plot showing reduced stress gene expression profile in DANs isolated from co-cultures compared to monocultures in relation to protein-misfolding, ER stress and reactive oxygen species (ROS), metabolic stress, mitochondrial stress and hypoxia. The strongest effect was observed under the fibril-seeded conditions.

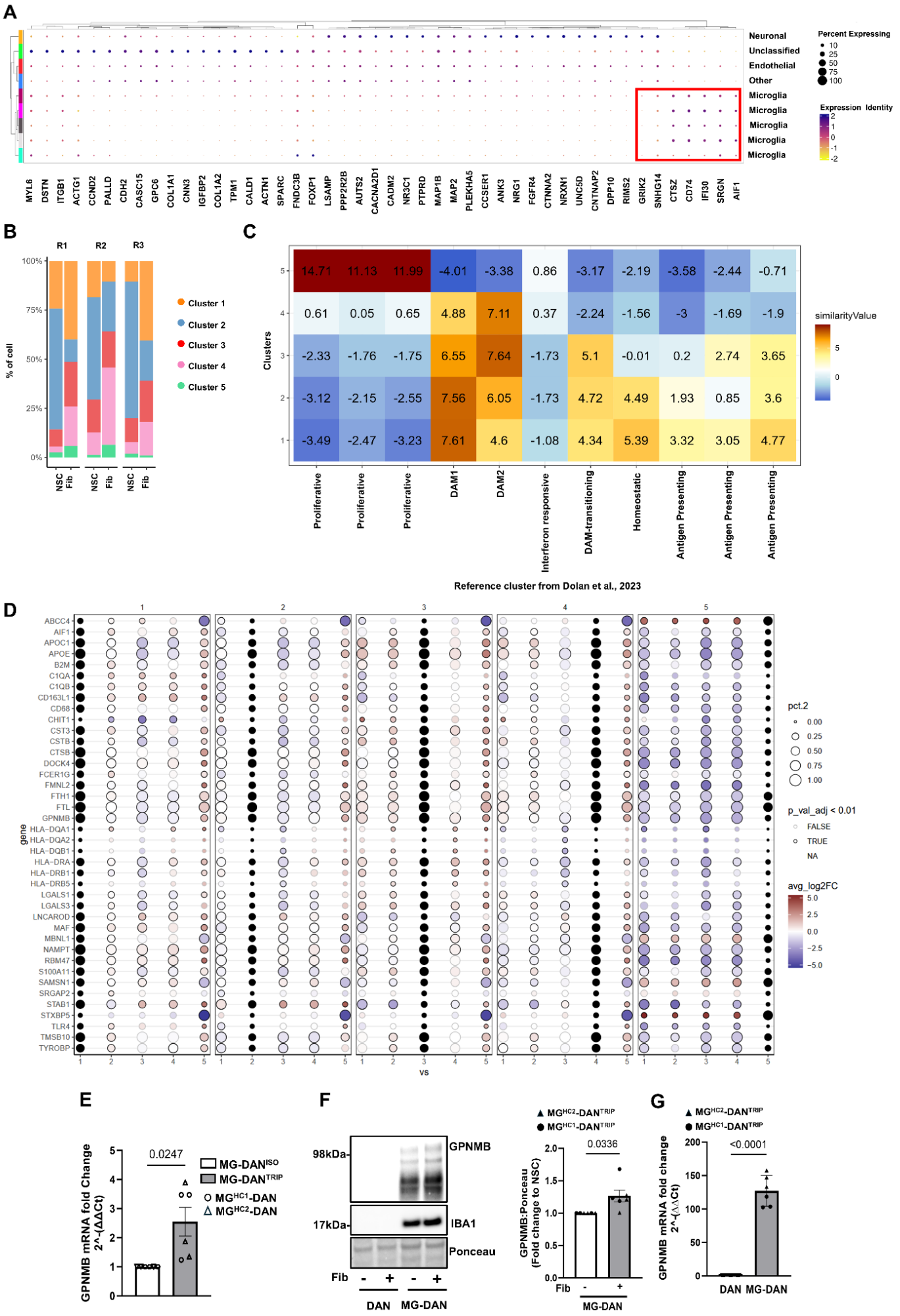
A
Neuronal
Unclassified
Endothelial
Other
Microglia
Microglia
Microglia
Microglia
Microglia
Percent Expressing
10
25
50
75
100
Expression Identity
2
1
0
-1
-2
MYL6 DSTN ITGB1 ACTG1 CCND2 PALLD CDH2 CASC15 GPC6 COL1A1 CNN3 IGFBP2 COL1A2 TPM1 CALD1 ACTN1 SPARC FNDC3B FOXP1 LSAMP PPP2R2B AUTS2 CACNA2D1 CADM2 NR3C1 PTPRD MAP1B MAP2 PLEKHA5 CCSER1 ANK3 NRG1 FGFR4 CTNNA2 NRXN1 UNC5D CNTNAP2 DPP10 RIMS2 GRIK2 SNHG14 CTSZ CD74 IFI30 SRGN AIF1
B
R1
R2
R3
100%
75%
50%
25%
0%
% of cell
NSC
Fib
Cluster 1
Cluster 2
Cluster 3
Cluster 4
Cluster 5
C
Clusters
14.71 11.13 11.99 -4.01 -3.38 0.86 -3.17 -2.19 -3.58 -2.44 -0.71
0.61 0.05 0.65 4.88 7.11 0.37 -2.24 -1.56 -3 -1.69 -1.9
-2.33 -1.76 -1.75 6.55 7.64 -1.73 5.1 -0.01 0.2 2.74 3.65
-3.12 -2.15 -2.55 7.56 6.05 -1.73 4.72 4.49 1.93 0.85 3.6
-3.49 -2.47 -3.23 7.61 4.6 -1.08 4.34 5.39 3.32 3.05 4.77
Proliferative
Proliferative
Proliferative
DAM1
DAM2
Interferon responsive
DAM-transitioning
Homeostatic
Antigen Presenting
Antigen Presenting
Antigen Presenting
similarityValue
5
0
Reference cluster from Dolan et al., 2023
D
gene
ABCC4 AIF1 APOC1 APOE B2M C1QA C1QB CD163L1 CD68 CHIT1 CST3 CSTB CTSB DOCK4 FCER1G FMNL2 FTH1 FTL GPNMB HLA-DQA1 HLA-DQA2 HLA-DQB1 HLA-DRA HLA-DRB1 HLA-DRB5 LGALS1 LGALS3 LNCAROD MAF MBNL1 NAMPT RBM47 S100A11 SAMSN1 SRGAP2 STAB1 STXBP5 TLR4 TMSB10 TYROBP
vs
pct.2
0.00
0.25
0.50
0.75
1.00
p_val_adj < 0.01
FALSE
TRUE
NA
avg_log2FC
5.0
2.5
0.0
−2.5
−5.0
E
GPNMB mRNA fold Change 2^-(ΔΔCt)
0.0247
MG-DAN^ISO
MG-DAN^TRIP
MG^HC1-DAN
MG^HC2-DAN
F
98kDa-
17kDa-
GPNMB
IBA1
Ponceau
Fib
DAN
MG-DAN
MG^HC2-DAN^TRIP
MG^HC1-DAN^TRIP
0.0336
GPNMB:Ponceau (Fold change to NSC)
G
<0.0001
GPNMB mRNA fold change 2^-(ΔΔCt)
DAN
MG-DAN

Fig S8. scRNA-seq reveals DAM Subtype mediating clearance of α-synuclein aggregates.

(A) Clustered dot plot showing marker expression across cell types, with microglia further grouped into subclusters

(B) Analysis of MG cluster composition across NSC and fibril-seeded conditions revealed a higher proportion of MG in clusters 3 and 4 under the fibril-seeded conditions.

(C) Similarity of MG clusters with published iPSC-derived human microglia states upon exposure to different brain substrates (Dolan et al., 2023) based on similarity scores (González-Velasco et al., 2024).

(D) Dot plot showing expression of MG cluster-defining genes with pairwise comparisons between clusters.

(E) qPCR analysis showing increased expression of *GPNMB* in MG co-cultured with DAN^{TRIP} compared to DAN^{ISO} normalized to GAPDH (n = 3 independent differentiations for MG^{HC1}-DAN^{ISO}, MG^{HC1}-DAN^{TRIP2} , MG^{HC2}-DAN^{ISO}, and MG^{HC2}-DAN^{TRIP2}).

(F) Immunoblotting confirmed increased expression of GPNMB in MG-DAN co-cultures under fibril-seeded conditions (n=3 independent differentiations for MG^{HC1}-DAN^{TRIP1} and MG^{HC2}-DAN^{TRIP1}).

(G) qPCR analysis shows that *GPNMB* is primarily expressed in MG-DAN co-cultures (n = 3 independent differentiations for MG^{HC1}-DAN^{TRIP1} and MG^{HC2}-DAN^{TRIP1}).

Data are presented as mean ± SD. Statistical analysis by one sample t-test **(E, F, G)**.

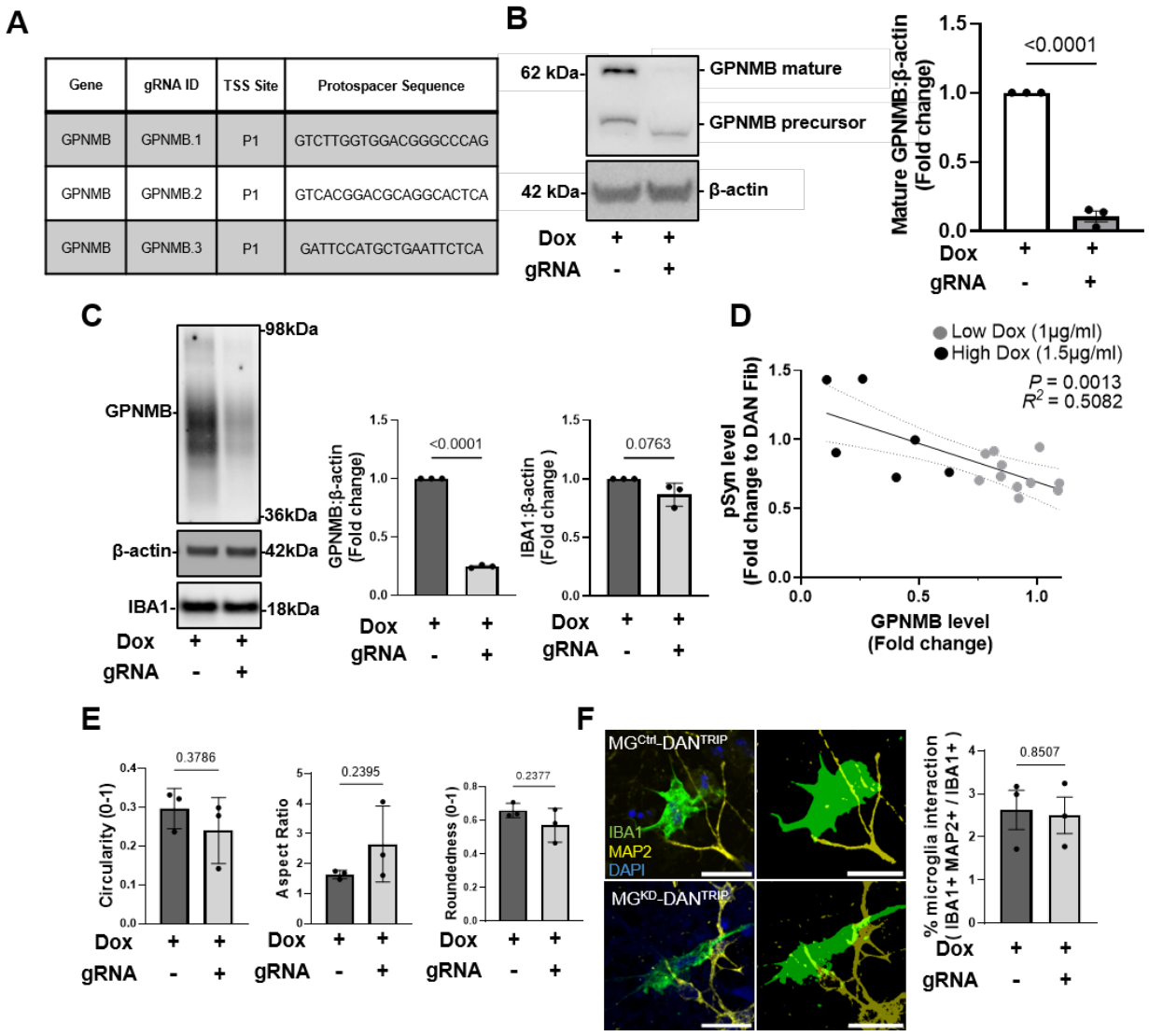

Fig. S9 Validation and characterization of GPNMB Knockdown

(A) gRNA sequences obtained from the hCRISPRi-v2.1 Weissman Laboratory Library. The targeted promoter region at the transcription start site (TSS) is indicated.

(B) Representative immunoblot and quantification for GPNMB in iPSC lysates showing 90% knockdown upon doxycycline treatment in transduced stem cells (n = 3 independent experiments for $iPSC^{dCas9}$).

(C) Representative immunoblot and quantification of GPNMB and IBA1 in MG monoculture lysates, showing a 75% knockdown of GPNMB upon doxycycline treatment in transduced MG compared to control, with no change in IBA1 expression (n = 3 independent experiments for MG^{dCas9}).

(D) Simple linear regression revealed a significant inverse relationship between relative GPNMB levels (fold change relative to control) and pSyn levels normalised to DAN Fib ($R^2 = 0.5082$, slope = −0.5605, $P = 0.0013$; n = 17 independent differentiations for MG^{dcas9}-DAN^{TRIP1}).

(E) Quantification of IBA1-masked MG for roundedness, circularity and aspect ratio under non-seeded (NSC) and fibril-seeded (Fib) conditions in MG-DAN^{TRIP} co-cultures with or without GPNMB knockdown (n=3 independent differentiations for MG^{dcas9}-DAN^{TRIP1}). *Scale bar*, 20 µm

(F) Representative confocal images and corresponding binary masks of MG^{dcas9}-DAN^{TRIP} co-cultures with or without GPNMB knockdown, showing IBA1/MAP2 overlap. Quantification was performed using Manders' coefficient to determine the percentage overlap of IBA1 with MAP2 in each image stack.(n = 3 independent differentiations for MG^{dcas9}-DAN^{TRIP1}).

The graphs show mean ± SD and was analysed by one sample t-test **(B, C)**, two-tailed t-test **(E, F)** and simple linear regression **(D).**

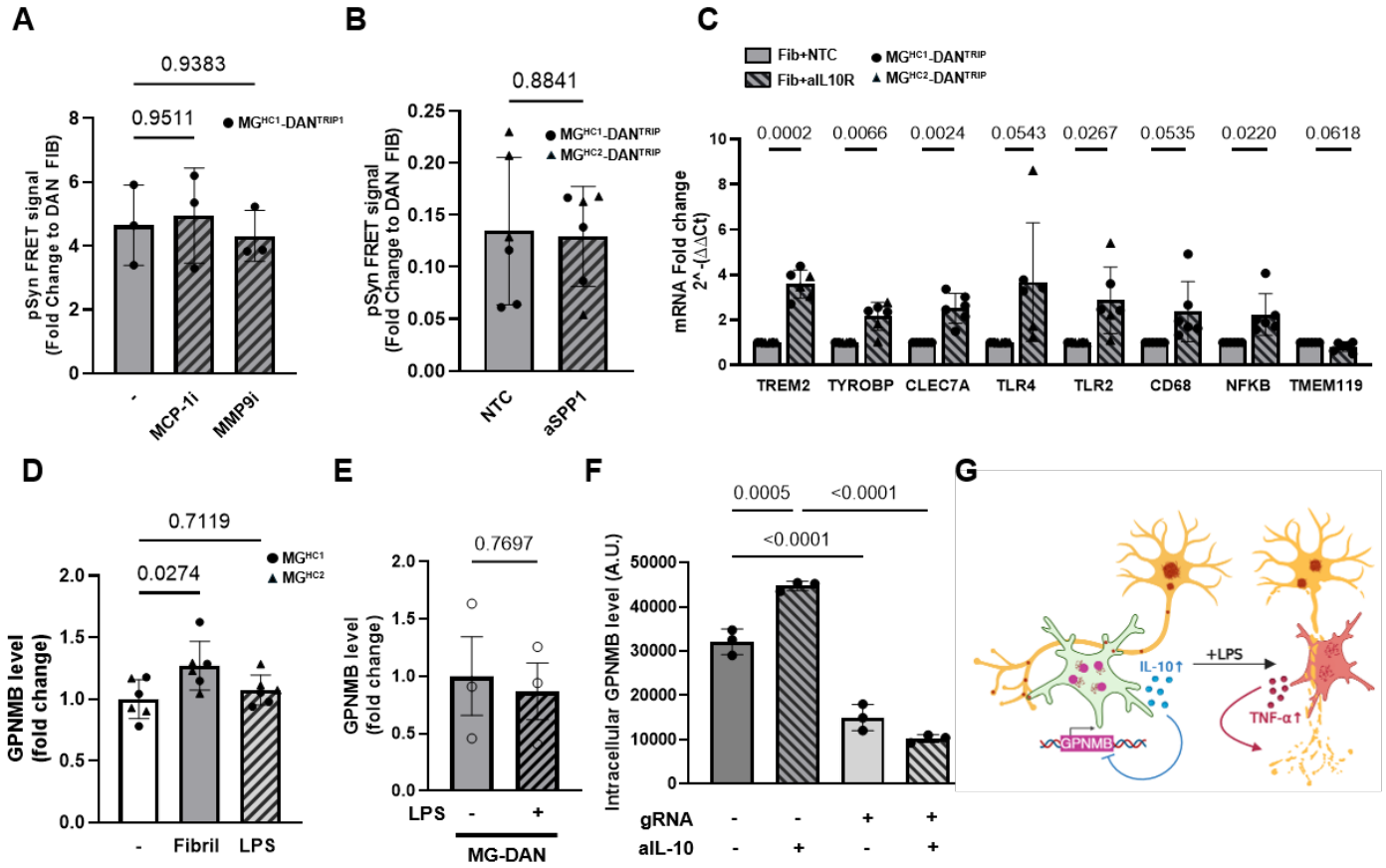

Fig S10. Autocrine IL-10 signalling limits microglia-mediated clearance of α-synuclein aggregates

(A) pSyn levels in MG-DAN did not change upon treatment of MCP-1 inhibitor (2µM) or MMP9 inhibitor (5µM), as quantified using time-resolved FRET (n = 3 independent differentiations for MG^{HC1}-DAN^{TRIP1}).

(B) pSyn levels in MG-DAN did not change upon treatment of anti-SPP1 antibody (5µg/mL) compared to NTC IgG (5µg/mL), as quantified using time-resolved FRET (n = 3 independent differentiations for MG^{HC1}-DAN^{TRIP1} and MG^{HC2}-DAN^{TRIP1}).

(C) qPCR analysis showed increased expression of DAM markers (*TREM2, TYROBP, CLEC7A, TLR4, TLR2, CD68, NFKB*), and no change in the homeostatic receptor TMEM119 in anti-IL-10R treated co-cultures versus NTC IgG (n= 3 independent differentiations for MG^{HC1}-DAN^{TRIP1} and MG^{HC2}-DAN^{TRIP1})

(D) GPNMB protein levels in MG monoculture lysates as quantified using ELISA are increased in response to fibril treatment, but not LPS (n = 3 independent differentiations for MG^{HC1} and MG^{HC2}).

(E) Quantification of GPNMB protein levels in MG-DAN co-culture lysates using ELISA reveals no increase upon LPS treatment in fibril- seeded conditions (n = 3 independent differentiations for MG^{ISO}-MG-DAN^{TRIP2}).

(F) Quantification of GPNMB protein levels in MG–DAN co-culture lysates using ELISA reveals up-regulation following anti-IL-10R treatment in control MG, but not in co-cultures with GPNMB KD MG (n = 3 independent differentiations for MG^{HC1}-DAN^{TRIP1}).

(G) Schematic diagram of the identified autocrine mechanism and effect of LPS.

Data are presented as mean ± SD. Statistical analysis by one sample t-test **(C)**, two-tailed t-test **(B, E)**, and one-way ANOVA **(A, D, F)** followed by Tukey's post hoc test.

ID	Diagnosis	genotype	Sex	Biopsy age (years)	Original ID	Reprogramming method	iPSC clone characterisation	GEO
HC1	HC	WT/WT	M	49	OX3-9	Cytotune1	Dafinca et al., 2016	GSE64584
HC2	HC	WT/WT	F	67	AH017-13 (STBCi026-A)	Cytotune1	Fernandes et al., 2016	GSE53426
$SNCA^{ISO}$	PD	Isogenic to $SNCA^{TRIP2}$	F	55	Clone 1-13	Cytotune1	Heman-Askah et al., 2017	GSE89886
$SNCA^{TRIP1}$	PD	Triplication/WT	F	55	SFC831-03-05 (STBCi024-C)	Cytotune1	Haenseler et al., 2017	GSE89886
$SNCA^{TRIP2}$	PD	Triplication/WT	F	55	ND34391G	Cytotune1	Heman-Askah et al., 2017	GSE89886
dCas9-HC1	HC	WT/WT	F	49	BUK4 (dCas9-OX 3-9)	Cytotune1	This study	N/A
$TREM2^{WT}$	HC	WT/WT	M	19	BIONi010-C	Cytotune 2	Hall-Roberts et al., 2020	GSE157635
$TREM2^{KO}$	HC	KO/KO	M	19	BIONi010-C-17	Cytotune 2	Hall-Roberts et al., 2020	GSE157635
LRRK2-1	PD	G2019S	F	57	MK144 (UOXFi008-A)	Retrovirus	Sandor et al., 2017	GSM2055807
LRRK2-2	PD	G2019S	M	57	SFC855-03-01 (STBCi007-C)	Cytotune 2	Booth et al., 2019	GSE120306
GBA-1	PD	N370S	M	72	SFC834-03-01 (STBCi025-A)	Cytotune 2	Fernandes et al., 2016	GSE53426
GBA-2	PD	N370S	M	72	SFC834-03-03 (STBCi025-B)	Cytotune 2	Fernandes et al., 2016	GSE53426

Table S1. Cell line information for all hiPSC lines used in this study. HC = healthy control, PD = Parkinson's disease.

ID	Age	Sex	Diagnosis	PMI (hours)	Brain weight (g)
CTRL 1	65	F	Normal	24	-
CTRL 2	72	F	Normal	72	1339
CTRL 3	59	M	Normal	24	1370
iLB1	88	M	Normal (Braak LB stage 5)	24	-
iLB2	77	F	Normal (Braak tangle stage 2)	34	-
iLB3	82	M	Normal (Braak LB stage 5)	29	1435
PD1	72	M	PD (Braak stage 6)	42	-
PD2	81	M	PD (Braak stage 6)	37	-
PD3	80	F	PD (Braak stage 6)	-	-

Table S6. Patient information for post-mortem brain tissue used in this study. PMI=post-mortem interval.

Antibodies		
Mouse anti-Tuj1 (monoclonal), 1:1000	BioLegend	Cat# 801201 [TUJ1], RRID: AB_2313773
Rabbit anti-alpha-synuclein (phospho S129) (monoclonal), 1:1000	Abcam	Cat# ab51253 [EP1536Y], RRID: AB_869973
Chicken anti-MAP2 (polyclonal), 1:1000	Abcam	Cat# ab92434, RRID: AB_2138147
Mouse anti-β-Actin (monoclonal), 1:5000	Sigma	Cat# A1978 [AC-15], RRID: AB_476692
Rabbit anti-tyrosine hydroxylase (monoclonal), 1:500	Cell Signaling Technology	Cat# 58844 [E2L6M], RRID: AB_2744555
Goat anti-IBA1 (polyclonal), 1:500	Abcam	Cat#ab5076 RRID: AB_2224402
Rabbit anti-IBA1 (polyclonal) 1:1000	FUJIFILM Wako Chemicals	Cat#019-19741 RRID: AB_839504
Mouse anti-CD68 (monoclonal) 1:500	Invitrogen	Cat # 14-0688-82 RRID: AB_11151139
Mouse anti-Osteoactivin/GPNMB (polyclonal) 1:500	Bio-Techne	Cat #AF2330 RRID: AB_2112934
Goat anti-Osteoactivin/GPNMB (polyclonal)1:500	Bio-Techne	Cat #AF2550 RRID: AB_416615
Mouse anti-CD22 (Clone 219903) 5μM	Bio-Techne	Cat#MAB19682 RRID: AB_3532205
Moust anti-IL10R Alpha 1μM	Bio-Techne	Cat#MAB274 RRID: AB_358187
anti-human osteopontin (SPP1) 5ug	Bio X cell	Cat#BE0382 RRID: AB_2927519
Mouse IgG_1 Isotype Control	Bio-Techne	Cat#MAB002 RRID: AB_357344
TREM2 Antaognist 10μg/ml	Eli Lilly	
IgG Control	Eli Lilly	
Goat anti-Mouse Alexa Fluor™ 488-conjugate, 1:1000	Invitrogen	Cat# A-11001, RRID: AB_2534069
Goat anti-Rabbit Alexa Fluor™ 488-conjugate, 1:1000	Invitrogen	Cat# A-11034, RRID: AB_2576217
Goat anti-Mouse Alexa Fluor™ 568-conjugate, 1:1000	Invitrogen	Cat# A-11031, RRID:AB_144696
Goat anti-Rabbit Alexa Fluor™ 568-conjugate, 1:1000	Invitrogen	Cat# A-11036, RRID: AB_10563566
Goat anti-Chicken Alexa Fluor™ 647-conjugate, 1:1000	Invitrogen	Cat# A-21449, RRID: AB_2535866
Donkey anti-Goat Alexa Fluor™ Plus 405-conjugate, 1:250	Invitrogen	Cat# A48259 RRID: AB_2890272
Donkey anti-Chicken Alexa Fluor™ 647-conjugate, 1:1000	Invitrogen	Cat#A78952 RRID: AB_2921074
Donkey anti-Rabbit Alexa Fluor™ 568-conjugate,1:1000	Invitrogen	Cat#A10042 RRID: AB_2534017
Donkey anti-Mouse Alexa Fluor™ 488-conjugate, 1:1000	Invitrogen	Cat#A21202 RRID: AB_141607

Table S7. Information for all antibodies used for blocking, immunocytochemistry and immunoblotting in this study.

Gene	Forward sequence (5' to 3')	Reverse sequence (3' to 5')
APOE	GTTGCTGGTCACATTCCTGG	GCAGGTAATCCCAAAAGCGAC
AXL	ATCAGCTTCGGCTAGGCAG	TCCGCGTAGCACTAATGTTCT
CD22	GCACCCTGAAACCCTCTACG	ATCAAACTTCGAGGTGTTCTTGT
CD68	CTTCTCTCATTCCCCTATGGACA	GAAGGACACATTGTACTCCACC
CHIT1	GGGCTCTGCTGCAAAACTG	AGAGTCTCGTCATTCCACTCAG
CLEC7A	GTCCTGGGTACCATGGCTATT	GTGTGGGTTGACTGTGGTTC
C1QA	GTGACACATGCTCTAAGAAG	GACTCTTAAGCACTGGATTG
CSF1R	GGGAATCCCAGTGATAGAGCC	TTGGAAGGTAGCGTTGTTGGT
GAPDH	TGGAAGGACTCATGACCACAG	CAGTGGGGACACGGAAGG
GAS6	CGAAGAAACTCAAGAAGCAG	AGACCTTGATCTCCATTAGG
GPNMB	CTTCTGCTTACATGAGGGAGC	GGCTGGTGAGTCACTGGTC
GPR34	GAAGACAATGAGAAGTCATACC	TGTTGCTGAGAAGTTTTGTG
LGALS3	ATGGCAGACAATTTTTCGCTCC	GCCTGTCCAGGATAAGCCC
LPL	AGGATGTGGCCCGGTTTATC	CCAAGGCTGTATCCCAAGAGAT
MERTK	AGGACTTCCTCACTTTACTAAG	TGAACCCAGAAAATGTTGAC
NFKB1	GAAGCACGAATGACAGAGGC	GCTTGGCGGATTAGCTCTTTT
P2RY12	AAGAGCACTCAAGACTTTAC	GGGTTTGAATGTATCCAGTAAG
PROS1	AAAGATGTGGATGAATGCTC	TCACATTCAAAATCTCCTGG
TLR2	AGTTGTGGGTTGAAGCACTG	TGGAGAGGCTGATGATGACC
TLR4	GCGTGGAGGTGGTTCCTAAT	GAGGTGGCTTAGGCTCTGAT
TNF-α	CAAAGTAGACCTGCCCAGAC	GACCTCTCTCTAATCAGCCC
TREM2	TCTGAGAGCTTCGAGGATGC	GGGGATTTCTCCTTCAAGA
TYROBP	ACTGAGACCGAGTCGCCTTAT	ATACGGCCTCTGTGTGTTGAG

Table S8. Primer sequences used for RT-qPCR.